A Flow-to-Digital Converter based on a Thermal-Sigma Delta Modulator

By
Avish Gupta

In partial fulfilment of the requirements for the degree of

Master of Science in Electrical Engineering
At the Department of Microelectronics (Electronic Instrumentation),
Faculty of Electrical Engineering, Mathematics and Computer Science,
Delft University of Technology

To be defended on September 20th, 2023

Student Number:	5491231	
Supervisors:	Prof. Dr. K.A.A. Makinwa	TU Delft
	Gert Jan Snijders	Bronkhorst
Thesis Committee:	Prof. Dr. K.A.A. Makinwa	TU Delft
	Dr. D.G. Muratore	TU Delft
	Gert Jan Snijders	Bronkhorst

Abstract

Flow sensing is essential in various industrial, commercial, and biomedical applications. Although many types of flow sensors exist, thermal flow sensors are widely used due to their simple sensing elements (heaters and temperature sensors) and low fabrication costs. A low-cost interface for thermal flow sensors can then be realized with a Thermal Sigma-Delta Modulator (TΣΔM), which regulates the temperature of the sensing element, while simultaneously digitizing the required power.

This thesis discusses the design of a pseudo-differential TΣΔM to read out a thermal flow sensor, which consists of two heating resistors in thermal contact with the flow. The modulator maintains both resistors at a constant temperature and digitizes the required differential power. The resistors have a Positive Temperature Coefficient (PTC) and can thus be used as heaters and temperature sensors in a time-multiplexed manner, resulting in a compact realization. A prototype was fabricated using discrete components on a PCB. With a sampling frequency of 5kHz, the modulator achieved a thermal noise-limited resolution of greater than 13 bits in a bandwidth of 1.5Hz for a full-scale input of 7mL/min. The entire read-out was realized with two integrators, two clocked comparators, and a few switches, resulting in a simple, low-cost interface with direct digital read-out.

Acknowledgements

This last year has been a journey of learning and growth for me and would not have been possible without all the support and contribution I received. Here, I would like to thank the people who made this thesis possible.

First and foremost, I would like to thank my professor and supervisor, Prof. Dr. Kofi Makinwa, who gave me an opportunity to work on such an interesting multi-disciplinary project. During this past year, his advice and guidance in a technical and non-technical capacity helped me make the right decisions at a personal and professional level. His seemingly endless knowledge was elemental to the completion of my thesis, and I am grateful to have learned from him. Thank you, professor, for helping me understand that the best designs are the simplest ones and making me an electrical engineer.

I would like to thank Gert Jan Snijders from Bronkhorst, who was always more than willing to accommodate me in his busy schedule for calls and in-person visits, even letting me stay over at his house when I went to Ruurlo. His insight into the flow-sensing principles and sensor structures helped me develop a deeper understanding of the subject and proved to be key in interpreting the results. Many thanks also to Jens, Rob, Neils, and the rest of the team at Bronkhorst, whose friendly nature and approachability ensured I felt a part of the team even though I was far away in Delft while they were working from Ruurlo. Thank you for making this past year such an amazing and collaborative one.

I owe a great deal to my daily supervisor, Arthur Campos de Oliveira, who helped me understand the importance of balancing personal and professional life. He helped me out during the most challenging periods, and his patience with my countless questions greatly added to my engineering knowledge. Many thanks also to the researchers and PhD candidates at the Electronic Instrumentation Laboratory, Sundeep, Nandor, Eren, Alireza, Suhas, and Zhong, for providing constructive feedback and reviewing my work on multiple occasions. I would really miss the lunches we had, not to mention the various insightful discussions on technical and worldly matters. Special thanks to Lukasz, Ron and Zu Yao for assisting me in my measurement setup and always being willing to walk across the campus, looking for the necessary components and equipment. Their experience and assistance really streamlined the entire measurement process.

A great deal of professional success comes from a happy personal life. For my good fortune in that domain, I thank all my friends and colleagues – Shenyang, Giorgos, Jida, Sanja, Tanmeet, Mahesh, Kyle, Dimitris, Yash, Aryan, Raga and many more. Thank you all for helping me feel at home while being thousands of kms away from it.

A special and important thanks to my parents and my sister. Their unwavering support and faith in me propelled me to come to Delft and undertake such a challenging project. I am indebted to them for the person I am today. A final thanks to the Lord, who has always guided me to where I need to be.

Table of Contents

List of Figures

List of Tables

Chapter 1. Introduction

Fluid flow sensing is essential in many applications requiring gas monitoring [1], flow cytometry [2], wind measurement [3], and the semiconductor industry [4]. Depending upon the primary physical principle used to sense the fluid flow, they can be classified as inferential flow sensors (e.g., orifice plate and venturi meter), direct-measurement flow sensors (e.g., positive-displacement), and energy-assistive flow sensors (e.g., Coriolis, ultrasonic, and thermal) [5]. The energy-assistive flow sensors are non-contact and are thus more suitable for low-flow sensing applications. These sensors leverage the changes induced due to fluid flow in Coriolis force [6], Nuclear Magnetic Resonance [7], Temperature [8], or other physical phenomena to measure flow. Their output can then be converted into a digital signal for further processing by a microcontroller to either control the fluid flow or display the flow rate to the user.

Thermal flow sensors need only a few temperature sensors placed around a heating element to measure fluid flow. The simple structure and lack of moving parts simplify their fabrication and operating requirements. Thus, thermal flow sensors are suitable for low-cost, large-volume production. Moreover, thermal sensors benefit well from the current trend of miniaturization, where reducing size leads to lower power consumption and higher sensitivity to low flows. As a result, thermal flow sensors are commonly used for commercial applications [9].

The output of thermal flow sensors is an electrical signal, which is usually amplified and then digitized via an external Analog-to-Digital Converter (ADC) for further processing. Thermal Sigma Delta Modulators are ADCs that can directly digitize an analog heat flow and can thus be used to interface thermal flow sensors [10]. This thesis discusses the design of a Thermal Sigma Delta based read-out to interface a thermal flow sensor in a simple and cost-efficient manner.

1.1. Thermal Flow Sensors

Thermal flow sensors are a class of flow sensors in which fluid flow is converted to temperature changes in the fluid channel due to forced convection. This temperature change is read out and converted into an electrical signal for further processing. Thus, the fluid flow is converted from the mechanical domain to the thermal domain and then to the electrical domain, as shown in Fig. 1-1 [11]. The simple structures needed to realize thermal flow sensors allow for robust, low-cost, and scalable solutions and have thus been investigated extensively in the literature [9]. However, thermal flow sensors are not without their limitations. Since fluid flow is sensed indirectly via temperature changes, they are highly dependent on the heat capacity of the fluids. Thus, they have to be calibrated for different liquids and gases, which limits their use to applications where the exact composition of the fluid is known. Despite the limitations, thermal flow sensors dominate the flow sensing market [12] due to the ease of manufacturing and operating such sensors.

Based on different types of transduction principles, thermal flow sensors can be classified as hot-wire/hot-film anemometric sensors (Fig. 1-2(a)), calorimetric sensors (Fig. 1-2(b)), and time-of-flight (Fig. 1-2(c)) sensors. Anemometric sensors measure the total heat of the heated object lost to the flow [13], [14]. Anemometric sensors have a monotonic response to flow and saturate when the temperature of the heated object falls to ambient temperature due to fluid flow. Anemometric sensors can only measure fluid flow speed, not direction [15]. On the other hand, Calorimetric sensors can

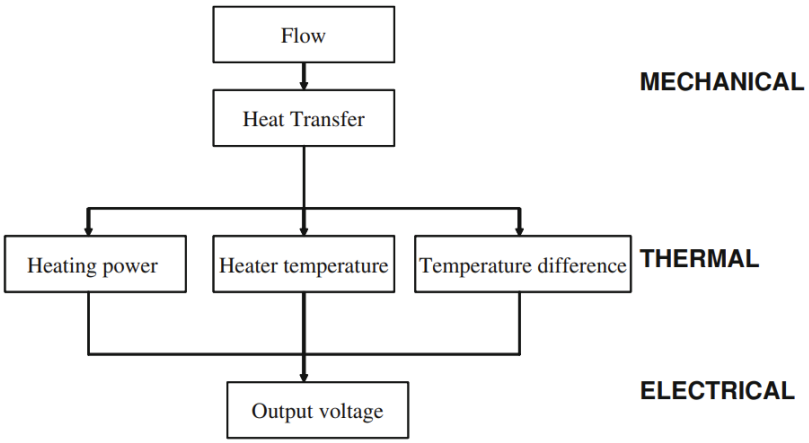

Fig. 1-1: Signal transport of thermal flow sensors [11]

(a) Anemometric Flow Sensor

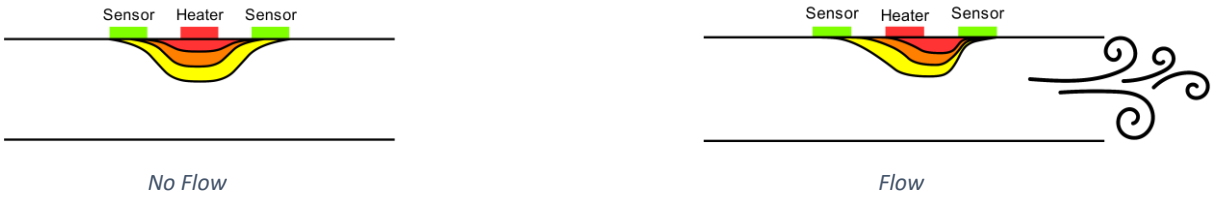

(b) Calorimetric Flow Sensor

(c) Time-Of-Flight Sensor

Fig. 1-2: Thermal Flow Sensor types

measure fluid flow speed and direction by measuring the changes in heat distribution around the heated element. However, depending on how calorimetric sensors are interfaced, they can have a non-monotonic response to flow [15]. Thermal time-of-flight sensors work by measuring the time taken by a fluid heated via a heater to travel a known distance [16]-[19]. These sensors offer the advantage that they can be made independent of the fluid's thermal properties; however, they need complex signal processing and have a limited dynamic range [19]. The sensing structures in the three classes of thermal flow sensors are similar. Thus, many flow sensors reported in the literature use more than one operation principle [20]-[26] to improve the sensor's linearity and dynamic range.

1.2. Interfacing Thermal Flow Sensors

An interface is needed for thermal flow sensors to bias the heater and the temperature sensor. The heater raises the temperature of the fluid flow path, and the temperature sensor measures the fluid-flow-induced temperature changes. The interface also needs to convert these temperature changes into a digital signal to display the flow rate to the user or to give the information to a fluid flow controller. This interface should be implemented in a cost-efficient manner while ensuring the performance of the thermal flow sensor is maximised.

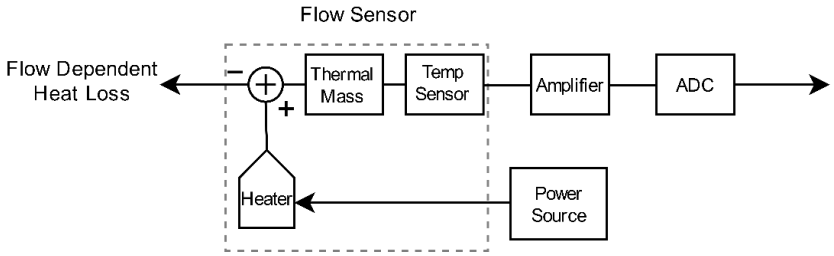

Fig. 1-3: Open Loop Flow sensor architecture [10]

Thermal flow sensors can be interfaced in an open loop (Fig. 1-3) or a closed loop (Fig. 1-4) manner. The open loop approach allows for a simple interface where constant power is applied to the heater, and the temperature sensor measures the flow information. The temperature sensor output passes through a signal processing chain, usually consisting of an amplifier and an ADC. The simplicity of the open loop approach allows for a low-cost interface for thermal flow sensors and has been used frequently in literature [3][9]. However, the open loop interface of thermal flow sensors makes the read-out dependent on the sensor's thermal mass properties. The thermal mass, which can be modelled as a low pass filter in the thermal domain [27], thus limits the response time of such sensors. Moreover, the open loop system's performance and accuracy depend on all the blocks in the signal chain, each adding errors to the overall output.

Alternatively, the closed-loop approach puts the sensor in a feedback loop, modulating the heater power to cancel out the flow-induced temperature changes [9][10]. As a result, the sensor's thermal mass is maintained at a constant temperature, resulting in a faster response time compared to open-loop architecture [28]. Moreover, the loop gain will suppress the inaccuracies of the various blocks in the signal chain, and the system transfer function will be mainly governed by the feedback path. These benefits have made the closed-loop interface a popular way to read out thermal flow sensors in applications requiring fast response times and high accuracy [10], [29]-[32].

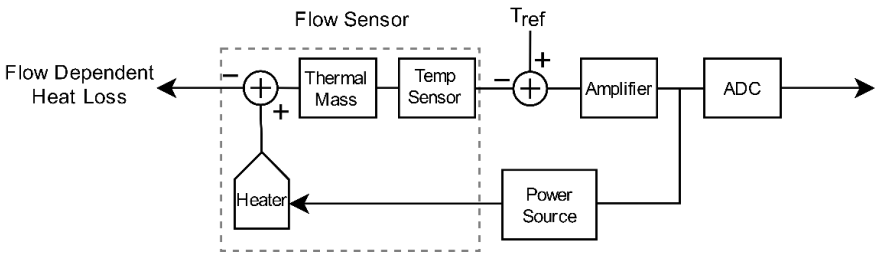

Fig. 1-4: Closed Loop Flow sensor architecture [10]

1.3. Thermal Sigma Delta modulator

The interface shown in Fig. 1-4 can be further refined by moving the ADC inside the feedback loop (Fig. 1-5). The resulting system will now have a direct digital output while maintaining the sensor's thermal mass at a constant temperature, thereby retaining all the benefits of the closed-loop architecture

mentioned above while also suppressing the errors due to the ADC. However, the feedback will need a digital-to-analog converter (DAC) to convert this digital output to its analog equivalent before being given to the sensor's thermal mass. The topology shown in Fig. 1-5 resembles that of a Sigma-Delta (ΣΔ) Modulator, with the primary difference that the flow sensor's thermal mass now forms the first "integrator" in the loop and is thus called Thermal Sigma Delta (TΣΔ) Modulator [33]. Like a conventional ΣΔ modulator (ΣΔM), a TΣΔ modulator (TΣΔM) uses oversampling and noise-shaping [34] to achieve high-resolution while using a low-resolution ADC inside the loop. Thus, we can further simplify the architecture by using a 1-bit ADC inside the loop, allowing us to simplify the feedback DAC and drive the power source directly with the outputs of the 1-bit quantizer.

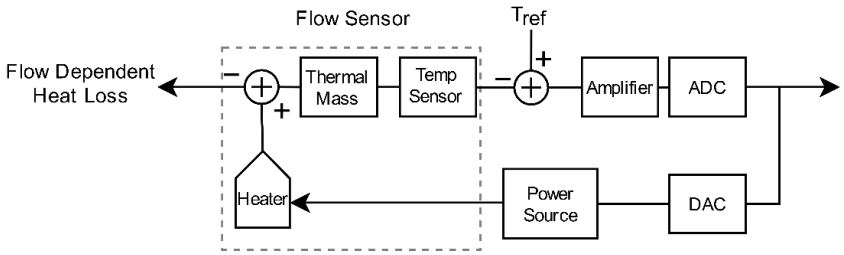

Fig. 1-5: Closed loop interface using Thermal Sigma Delta Modulator [10]

The use of TΣΔMs was proposed as early as 1990 [33] to read out an integrated anemometric flow sensor (Fig. 1-6(a)). The simplicity of the TΣΔ ADC allowed for easy integration of the sensing structure and interface electronics on a single chip, resulting in a "smart flow sensor" as demonstrated in [35][36][37]. The use of the TΣΔM for sensing the flow of liquids was demonstrated in [38]. Authors in [39] explored the limitations on resolution and sensitivity of the TΣΔM, the DC transfer function of which has a fractal structure due to thermal mass being a passive lossy integrator. A simple improvement was proposed by the same authors in [40], where an offset (AC and DC) was introduced (Fig. 1-6(b)) to disturb the modulator at zero flow, which improves the dynamic range. An approach to improve the modulator's resolution is described in [10], [29], which uses an electrical integrator in cascade with thermal mass, resulting in the design of an improved TΣΔM (Fig. 1-6 (c)). The improved modulator was used to interface an anemometric flow sensor built using discrete components. A TΣΔ interfaced anemometric wind sensor was also used in the Curiosity Rover's Environmental Monitoring Station [41], which used four in-plane anemometers to measure wind speed and direction.

Using a TΣΔM to interface a calorimetric flow sensor was first proposed in [42]. A 2-D calorimetric wind sensor was interfaced using a differential TΣΔM as described in [43][44]. A smart wind sensor is described [30] (Fig. 1-7 (a)), which uses three TΣΔ loops: two loops to digitize the wind speed and direction and an "overheat control loop" to maintain the sensor at a constant temperature above the ambient, independent of the fluid flow rate, thereby operating the sensor as a null-detector and resulting in improved transient response. [45] used the same sensing structure in a higher-order TΣΔM, achieving the same performance at lower power consumption by eliminating the overheat control loop. The power consumption was further reduced in [46], where the thermal properties of silicon were leveraged to measure the sensor's absolute temperature. However, all the designs used separate heating and sensing elements: thermopiles as temperature sensing elements and resistors as heaters, increasing production and implementation costs.

Though no implementations of TΣΔM to interface time-of-flight sensors have been found, the TΣΔ has been used in other applications, such as root-mean-square converter [47][48], conductivity sensor [49][50], radiation measurement [51][52], and temperature measurement [53].

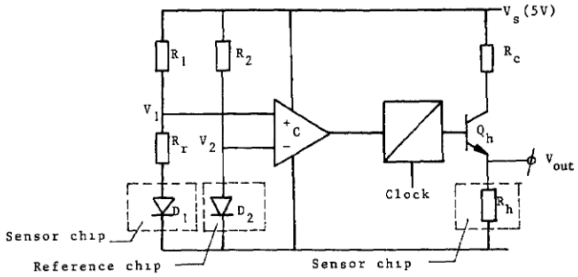

(a) First TΣΔM proposed in [33]

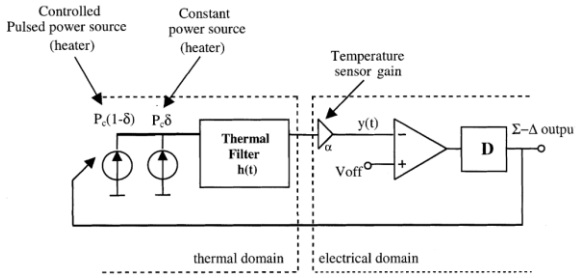

(b) A TΣΔ with offset (V_{Off}) to improve dynamic range [40]

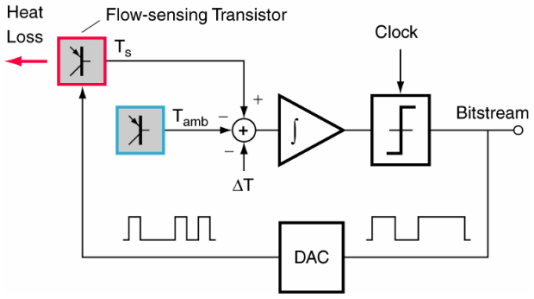

c) Improved TΣΔM with a cascaded thermal and electrical filter [29]

Fig. 1-6: TΣΔM to interface an Anemometric Flow Sensor

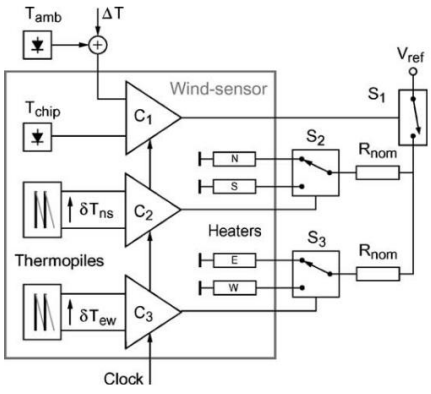

(a) TΣΔ based smart sensor read-out [30]

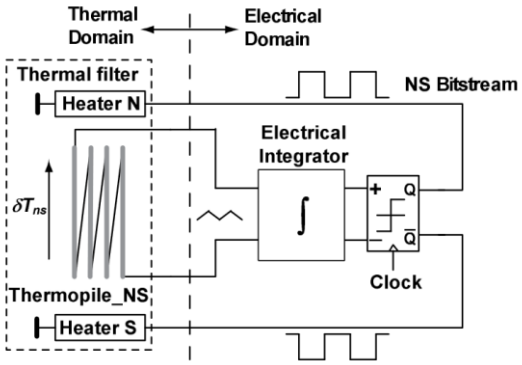

(b) A higher-order TΣΔ based smart sensor read-out [46]

Fig. 1-7: TΣΔM to interface a Calorimetric Flow Sensor

The TΣΔ based interface described in [54] reads out a convective accelerometer, which uses the same principle of operation as that of a flow sensor. [54] uses Positive Temperature Coefficient (PTC) (Fig. 1-8(a)) resistors in a time multiplexed manner (Fig. 1-8(b)) as heating and sensing elements. During phase ϕ1, the modulator is in "sensing" mode, and the Wheatstone Bridge containing the PTC resistors is normally biased. The output voltage, V_{out}, during the sensing phase will depend on the difference in the value of the PTC resistors, which will be governed by acceleration-induced convection. The feedback activates during phase ϕ2 when, based on the result of the sensing phase, the heated resistors are shorted, and the power is diverted to the cooler resistors. Thus, the convection-induced temperature difference is cancelled out, and the average output bit-stream now represents convection-dependent heat loss. However, due to the absence of common-mode feedback, as described in [30], the absolute temperature of the sensor is now input-dependent, which would limit the transient response.

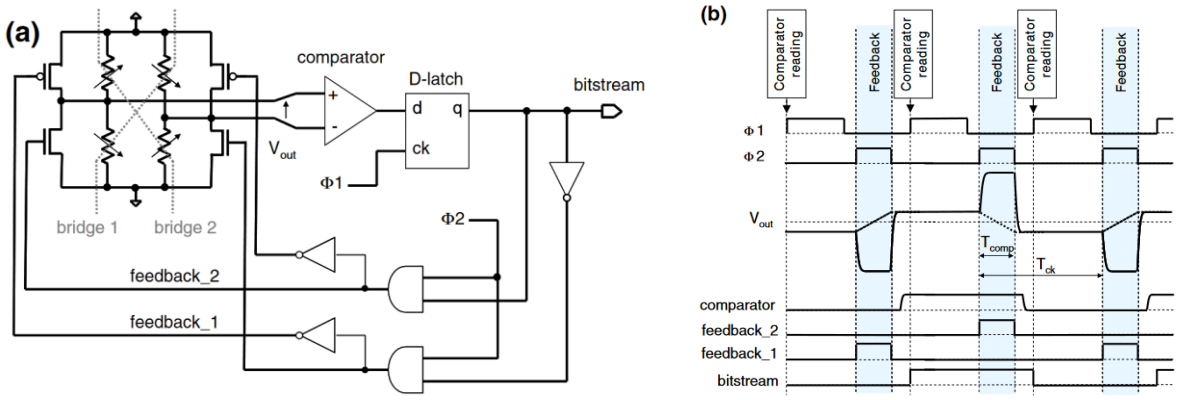

(a) Sensor Architecture using PTC resistors multiplexing as heating and sensing elements [54]

(b) The clock diagram showing time multiplexing scheme [54]

Fig. 1-8: Resistor-based time-multiplexed TΣΔ read-out for convective accelerometer [54]

Resistors as heating and sensing elements can also be used to realize fluid flow sensors, which reduces the implementation costs by reducing the number of components that need to be fabricated. As a result, resistor-based fluid flow sensors have been explored extensively in the literature [9][19][55] and have been commercialized as well [56].

1.4. Thesis Motivation

Bronkhorst Hi-Tech B.V. is a company that specializes in flow sensors and is one of the market leaders for low-flow sensing applications. Their thermal flow sensors [57][58][59] use PTC resistors as heaters and temperature sensors, thereby reducing the sensor fabrication costs. However, with the fabrication costs brought down, the design and cost of the interface circuitry to read out these sensors have become significant. A simple-low-cost interface using a TΣΔM is possible. However, to the best of our knowledge, a TΣΔM to read out a calorimetric flow sensor using a resistor as a heating and sensing element has not yet been published in the literature or publicized in a commercial product.

This thesis describes the design and implementation of a TΣΔM to read out a resistor-based calorimetric flow sensor from Bronkhorst in a time-multiplexed manner. The TΣΔ read-out will measure the flow rate while keeping the sensor's temperature constant (=35℃ above ambient) and independent of flow, resulting in fast response times (limited by sensor BW of ~1Hz) and offering high resolution (>13 bits). This thesis focuses on reading out a calorimetric sensor; however, the interface design was kept general, allowing it to read out Bronkhorst's anemometric sensors as well with minimal changes.

1.5. Thesis Organisation

This thesis report is organized into five chapters (including this introduction). Chapter 2 briefly highlights the construction of different sensor types available in this thesis, and the various modes to interface these sensors will be discussed. Chapter 3 will discuss the design of the TΣΔ interface to read out the chosen flow sensor. This chapter will introduce the basic concepts of ΣΔM followed by the concepts of TΣΔM and highlight key differences between the two. The modelling of thermal mass to be used as the first "integrator" in the ΣΔ loop is presented in this chapter, followed by the modelling of the TΣΔM. Chapter 4 discusses the implementation of the TΣΔM using discrete components to read out the chosen flow sensor. This chapter highlights the target specifications for the read-out, followed by the proposed architecture to meet all the requirements. The choice of discrete components is discussed, followed by top-level simulations of the designed modulator. Finally, the measurement results of the prototype modulator are discussed. Chapter 5 concludes this thesis, where a summary of the design is presented, followed by highlighting the potential future research opportunities.

Chapter 2. Thermal Flow Sensing

This chapter discusses the operation of various thermal flow sensors and possible interfaces to read them out. The basic principle of operation lies in the interaction of a heated body with a fluid flow. By measuring the change in absolute temperature (Fig. 1-2(a)), anemometric flow sensors can be realized, while by measuring the change in heat distribution (Fig. 1-2(b)), calorimetric flow sensors can be realized. The time-of-flight sensors (Fig. 1-2 (c)) are considered beyond the scope of this thesis and will not be discussed further.

Thermal flow sensors, which require only heaters and temperature sensors, can be realized in different ways. This chapter begins by elaborating on the different types of flow sensors available in this project and briefly discusses their construction. Various ways to operate these sensors will then be introduced, and the characteristics of each mode of operation will be discussed.

2.1. Thermal Flow Sensor Types

Heaters and temperature sensors form the core of a thermal flow sensor. Dedicated transducers can be used as heating and sensing elements [24][30][60]. However, a compact thermal flow sensor can be realized by multiplexing these transducer elements in time rather than space [61]. Such a realization uses the same node for heating and sensing, i.e., the node where the heater power is applied is the same as the node where the temperature change is measured. Such thermal flow sensors can be realized using active elements such as bipolar transistors [29] or passive elements such as resistors [61]. As discussed in the previous chapter, resistor-based thermal flow sensors are a popular choice for commercial implementation due to the low fabrication costs involved and have been used by Bronkhorst Hi-Tech B.V. in their flow meters and controllers [57][58][59].

This section will briefly discuss the resistor-based thermal flow sensors offered by Bronkhorst Hi-Tech B.V.

2.1.1. Anemometric Flow Sensor

An anemometric flow sensor consists of an ambient (medium) temperature sensor, a heated body, and an associated temperature sensor. The heater applies a heating power, P, to raise the temperature of a surface above ambient temperature. This difference between the ambient and surface temperature is called overheat (ΔT), which decreases due to flow-induced forced convection. The relationship between flow speed (U), ΔT and P was derived as early as 1914 by L.V. King [13]. Commonly known as King's law, this relation is given by eq. $(2\text{-}1)$

$$\frac{P}{\Delta T} = A + B\sqrt{U} \tag{2-1}$$

where A and B are temperature-dependent constants representing the sensor's heat loss to conduction and convection, respectively, and are influenced by sensor geometry and fluid properties. Eq. $(2\text{-}1)$ was derived primarily for laminar flow over a cylindrical wire, and though it was found to be applicable to many other geometries, a more generalised form of King's law is given by eq. $(2\text{-}2)$ [10]

$$\frac{P}{\Delta T} = A + BU^n \tag{2-2}$$

where n is a constant that depends on the sensor's geometry and Reynold's number governing the fluid flow (laminar or turbulent).

An anemometric flow sensor can be realized using two resistors with a high-temperature coefficient (TC) [14]. A resistor biased at low current to minimise self-heating will be used as a medium temperature sensor. A second resistor biased at large current will be used as a heater and as a temperature sensor to raise, as well as measure, the temperature of the sensor body. Fig. 2-1 (a) shows the sensor under nominal conditions when a constant ΔT is maintained. Due to flow-induced forced convection, the heated body cools down, and ΔT is reduced (Fig. 2-1 (b)). From King's law, flow speed can be determined with a known ΔT and P.

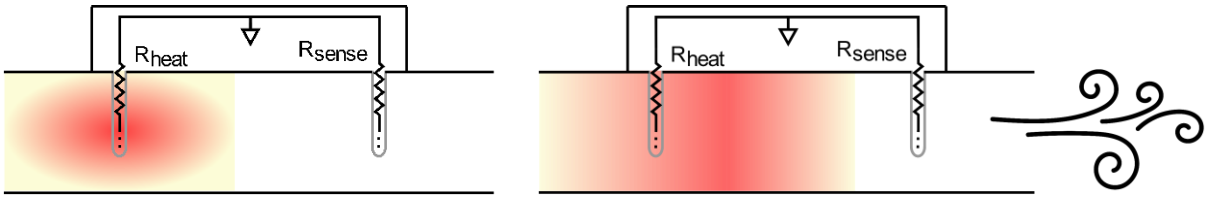

(a) No Flow *(b) Flow*

Fig. 2-1: Resistor-Based Anemometric Flow Sensor

The resistor-based anemometric flow sensor, used in Bronkhorst's Digital Mass Flow Meter and Controller for Gases, Mass-Stream™, is called the probe sensor and consists of two stainless steel rods or probes with resistors inside them. These rods are placed in the fluid flow path and are thus in direct contact with the fluid flow (Fig. 2-2) (and hence is also called direct through-flow measurement [62]). The first probe is a heater, and the second is a medium temperature sensor. The temperature difference between the heater and the medium sensor is the overheat (ΔT), and the heater power needed is P. Then, by using eq. (2-2) fluid flow speed can be determined. The simplicity of construction and the wide fluid flow path allow the use of anemometric sensors to sense the flow of liquids and gases [62]. However, the wide flow path also means that a large fluid volume needs to be heated, limiting the response time of these sensors, which is in the order of a few seconds.

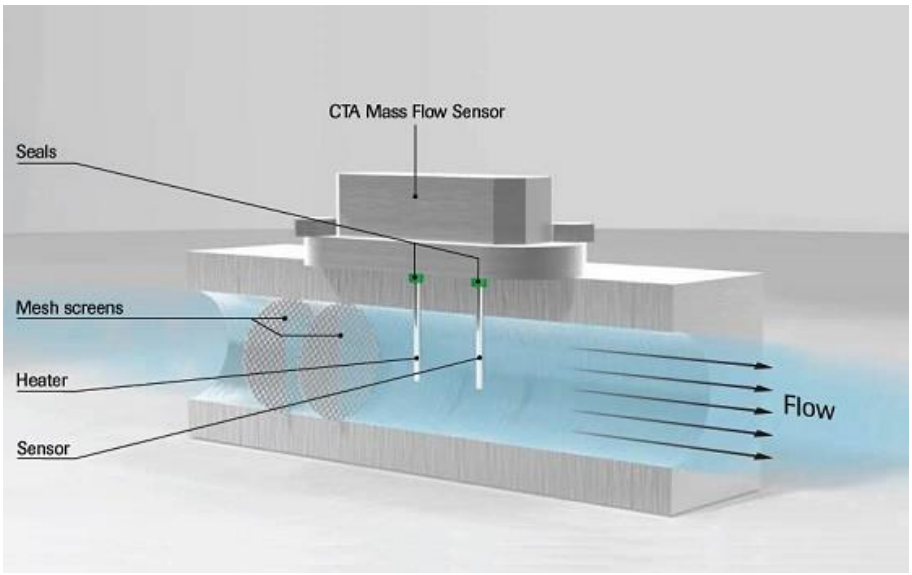

Fig. 2-2 : Anemometric Sensor [62]

2.1.2. Calorimetric Flow Sensors

Fluid flow cools down a heated surface asymmetrically, where the areas encountering the fluid first are cooled down more than those encountering the flow later. By measuring the temperature of two symmetrically located points around the centre of heat, fluid flow speed and direction can be determined [29][63], leading to a class of flow sensors called Calorimetric flow sensors.

A calorimetric sensor can be realized by using two high TC resistors as heaters and temperature sensors. A constant power can be applied to the resistors to heat the sensor body above the ambient temperature. A thermal equilibrium will be achieved when the heat is distributed uniformly about a point at the centre of the two resistors (Fig. 2-3(a)). Fluid flow will distort the symmetry of heat distribution (Fig. 2-3(b)). Note that the sensor body, as a whole, will cool down as well; however, in calorimetric flow sensors, the main parameter of interest is the differential heat loss to flow. Bronkhorst uses resistor-based calorimetric flow sensing in several products such as EL-Flow® Select , EL-Flow® Prestige, and Flexi-Flow™.

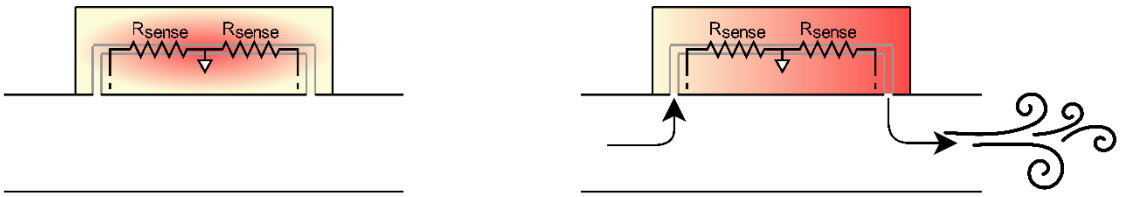

(a) No Flow *(b) Flow*

Fig. 2-3: Resistor-Based Calorimetric Flow Sensor

The calorimetric sensors used in this thesis use a bypass, as shown in Fig. 2-4, where a part of the flow is diverted from the main flow tube into a metallic capillary tube with thin walls [64]. A laminar flow element [65] is used in the main flow path to filter out turbulence in flow and acts to divert a ratio of the main flow through the bypass [66]. The bypass capillary tube has a small diameter, so only a small volume of fluid needs to be heated, resulting in a fast response time (~1s). The capillary tube consists of two PTC resistors wound symmetrically about the centre of the tube. These resistors are made of the resistherm wire with a diameter of 30µm, nominal resistance of 90Ω at 20℃ and TC of 3200 ppm/K. UV glue holds the resistors in place, and then the sensor housing is filled with foam before being closed.

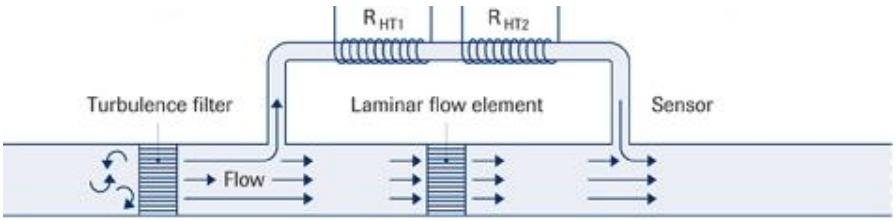

Fig. 2-4: Calorimetric Flow Sensor with a bypass [64]

2.2. Sensing Modes

The interface used for the Anemometric and the Calorimetric sensors strongly influences these sensors' response time and accuracy. This section discusses the different interfaces available to read out thermal flow sensors and their characteristics.

2.2.1. Anemometric Sensing Modes

The governing equation for Anemometric Sensors is given in eq. (2-2) from which it can be observed that there are two degrees of freedom available to us: the overheat (ΔT) and the heater power (P).

Usually, one of these parameters is kept constant and independent of flow, while the other is used to measure flow. This allows for at least two configurations: The constant power (CP) mode in which the sensor is operated in an open-loop manner, where the heater power is kept constant, and the temperature change is measured. The other mode is the constant temperature difference (CTD) mode, in which the sensor is operated in a closed loop where the overheat is kept constant by modulating the heating power. In CTD mode, the flow information is present in the power dissipated in the heater.

2.2.1.1. Constant Power (CP) Mode

The CP mode of operation for anemometric sensors involves biasing the sensor with a constant power source and measuring the change in ΔT due to fluid flow. For the flow sensor shown in Fig. 2-1, the resistor will act as the heater and the temperature sensor, where the resistance will vary with temperature and, thus, with flow. However, this means that the power dissipated in the circuit will also vary with the flow. Power regulating circuits can be used to ensure constant power dissipation, independent of flow. However, in many cases, a more straightforward implementation is preferred where the resistor is biased with constant voltage or current source, and the sensor output is calibrated in digital post-processing to accommodate the variations in the resistor. Fig. 2-5 (a) shows a possible realization of an anemometric sensor operated in CP mode where the resistors are biased using constant current sources. The difference between the voltages at the output of the two resistors is representative of the ΔT and can then be used to measure flow using eq. (2-2). Fig. 2-5(b) shows the variation of ΔT of a CP anemometer with flow. This simple implementation operates the sensor in an open-loop manner. As a result, the system's response time will be limited by the thermal time constants of the sensor and can be in the order of a few seconds. Moreover, the system's characteristics and accuracy will now be influenced by all the signal chain elements, including the influence of fluid properties and ambient temperature on the sensor.

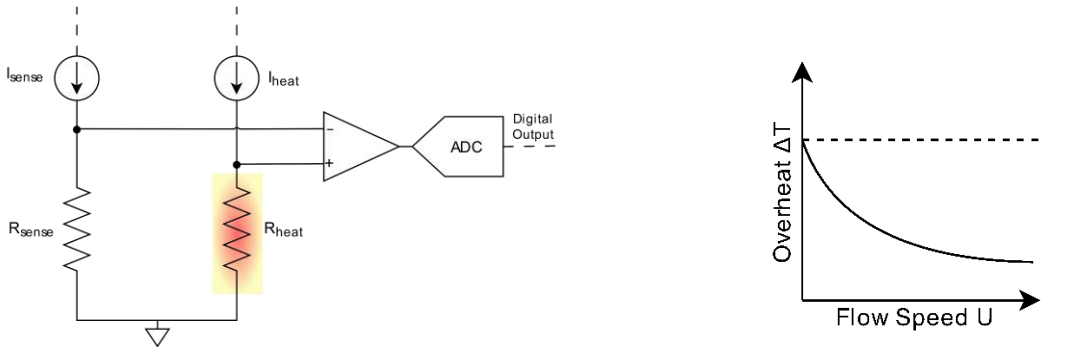

(a) Schematic Representation *(b) Flow speed vs Overheat Curve*

Fig. 2-5: CP Mode of operation of the Anemometric Sensor

2.2.1.2. Constant Temperature Difference (CTD) Mode

In CTD mode, the sensor is put in a closed loop to cancel out the flow-induced temperature drop, thereby regulating ΔT. This is done by using the sensor's output to increase the power flowing into the heater resistor, increasing the flow sensor's temperature. A CTD mode resistive thermal flow sensor can be realized by starting from the schematic of Fig. 2-5(a) and closing the loop from the output of the amplifier to modulate the current source of the heater resistor, as shown in Fig. 2-6 (a). Fig. 2-6 (b) shows the variation of heater power with respect to flow, which increases with the flow to raise the sensor's temperature. Putting the sensor in the feedback helps improve the system's response time and increases the sensor's 3dB bandwidth [28]. Moreover, the closed-loop system suppresses the non-idealities introduced by various blocks in the signal chain, resulting in the system transfer function being mainly governed by the feedback element.

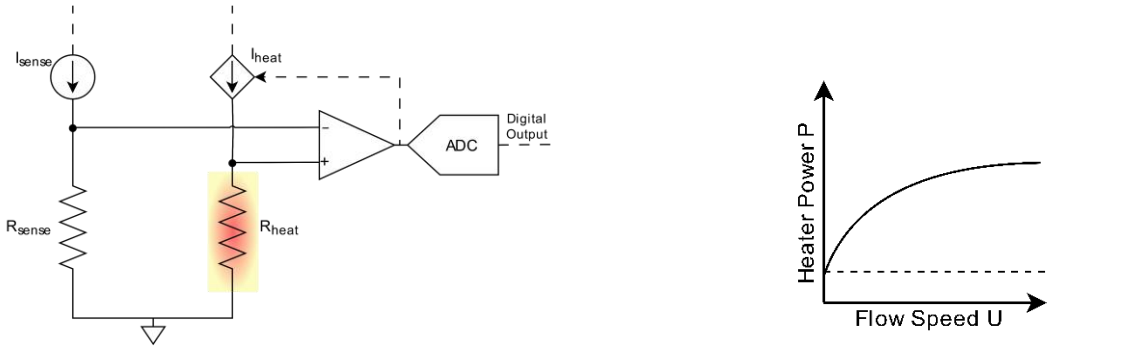

(a) Schematic Representation *(b) Flow speed vs heater power*

Fig. 2-6: CTD mode of operation of the Anemometric Sensor

2.2.2. Calorimetric Sensing Modes

For calorimetric sensors, another degree of freedom is available where a differential temperature is also created along with the cooling of the flow sensor body. So now, apart from measuring and regulating the overheat, the differential temperature (δT) can be measured or regulated. Measuring δT in an open loop manner results in temperature gradient (TG) configurations. δT can be cancelled by putting the sensor in a closed loop and applying differential power (δP), resulting in temperature balance (TB) configurations. Though operating the calorimetric sensors in CP vs CTD mode can affect its response time, the relevant flow information is contained in the differential temperature or differential power that must be applied. Hence, the classification of the calorimetric sensors is based on TG and TB modes, where the influence of the CP and CTD modes is discussed within it.

2.2.2.1. Temperature gradient (TG) modes

Temperature gradient modes rely on measuring the changes in the heat distribution due to fluid flow around the centre of heat (Fig. 2-3). To achieve this, the sensor body must first be heated above the ambient temperature, resulting in an overheat, ΔT, by applying power, P. Similar to anemometric sensing modes, two modes are possible while operating the calorimetric sensor in TG mode. By applying a constant power, the sensor's overheat varies with the flow. By regulating the total power applied, the overheat of the sensor can be kept constant. The resulting two modes are the CP-TG and CTD-TG modes.

For the resistor-based calorimetric sensor shown in Fig. 2-3, a simple CP-TG interface can be envisioned by biasing the sensor with a constant voltage or current source. Fig. 2-7(a) shows a possible realization of this interface where a constant heating power, 2 * I^2R, is applied to create an overheat, which reduces as a result of flow. However, the parameter of interest in calorimetric sensors is the temperature difference, δT, created due to flow rather than overheat. The differential temperature can then be converted to flow using eq. (2-3) [10]

$$\frac{\delta T}{P} = \frac{U^n}{C + DU^n} \tag{2-3}$$

where C and D are sensor constants. Operating the sensor in a CP-TG mode results in an open loop architecture and suffers from all the drawbacks mentioned in section 2.2.1.1, namely slower response time and larger influence of all the elements in the signal chain. Moreover, the calorimetric sensor operated in CP-TG mode has a non-monotonic transfer curve where the differential temperature saturates and then decreases with the flow as the overheat decreases [15] (Fig. 2-7 (b)).

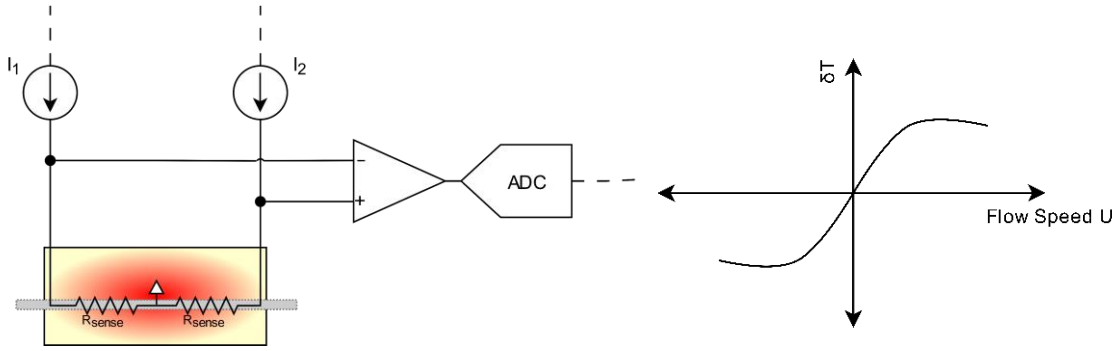

(a) Schematic Representation *(b) Flow speed vs differential temperature*

Fig. 2-7: CP-TG mode of operation of the Calorimetric sensor

The overheat can be regulated by putting the sensor in a closed loop and operating the sensor in a CTD-TG mode. This, however, requires an external temperature sensor to measure the ambient temperature. To operate the sensor shown in Fig. 2-3 in a CTD-TG mode, we also need to sense the common-mode temperature of the sensor, which is possible by using common-mode sense circuits, a simple implementation of which is two large resistors as shown in Fig. 2-8(a). In CTD-TG mode, the differential temperature can be related to flow speed by eq. (2-4) [10]

$$\frac{\delta T}{\Delta T} = SU^n \tag{2-4}$$

where S is again a constant depending upon the sensor's geometry and fluid properties. The CTD-TG mode regulates the overheat and, thus, has a monotonic response to flow, though very high flows still saturate the output (Fig. 2-8(b)). Moreover, operating the sensor in a CTD-TG mode will result in a faster transient response [28]. From eq. (2-3) and eq. (2-4), we can see that CP-TG mode needs calibration of 2 sensor constants to measure flow, whereas CTD-TG modes need calibration of one sensor constant proportional to flow. Hence, the additional calibration and the relation of eq. (2-3) can introduce extra sensing inaccuracy. However, from Fig. 2-7 and Fig. 2-8, we can see that the CTD-TG mode of operation comes at the cost of extra circuitry and complexity.

Due to the operation in TG mode, the part of the interface that contains the flow information still operates in an open loop manner. In both the CTD-TG and CP-TG modes, $I_1 = I_2$ or $\delta P = 0$ and δT varies with the flow. As a result, the system is still influenced by the non-idealities of all the blocks in the signal chain.

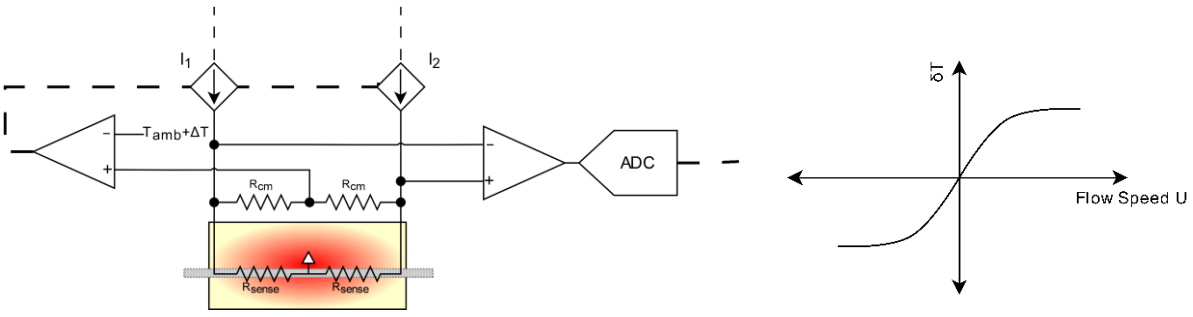

(a) Schematic Representation *(b)Flow speed vs differential temperature*

Fig. 2-8: CTD-TG mode of operation of the Calorimetric sensor

2.2.2.2. Temperature Balance (TB) modes

Temperature balance mode operates by putting the sensor in a closed loop to cancel out the flow-induced changes in the heat distribution, i.e., δT = 0. To achieve this for the sensor shown in Fig. 2-3, the power dissipated in each resistor must be modulated to maintain the centre of heat at the equilibrium point, independent of the fluid flow. Similar to TG mode, the total power dissipated in the sensor can be kept constant, leading to CP-TB mode, or the ΔT can be kept constant, resulting in a CTD-TB mode.

The CP-TB mode can be realized as shown in Fig. 2-9(a), where the differential power is modulated by varying I_1 and I_2 to cancel out the temperature difference created due to fluid flow. The flow information is now present in the differential heating power applied, which can be read out using two ADCs, one to read out the information regarding the differential current and one to read out the differential voltage (Fig. 2-9(a)). In this case, I_1+I_2 will be constant, and the current will be adjusted between them to cancel out δT. The δP will be proportional to δT, resulting in the flow vs δP curve being the same as the flow vs δT curve, which is shown in Fig. 2-9 (b) and will be given by eq. (2-5) [10]

$$\frac{\delta P}{P} = \frac{U^n}{E + FU^n} \tag{2-5}$$

where E and F are again constants. Operating the sensor in the CP mode results in a slower response time due to changing overheat. However, operating the sensor in TB mode puts the sensor in a closed loop, suppressing non-idealities associated with the read-out chain.

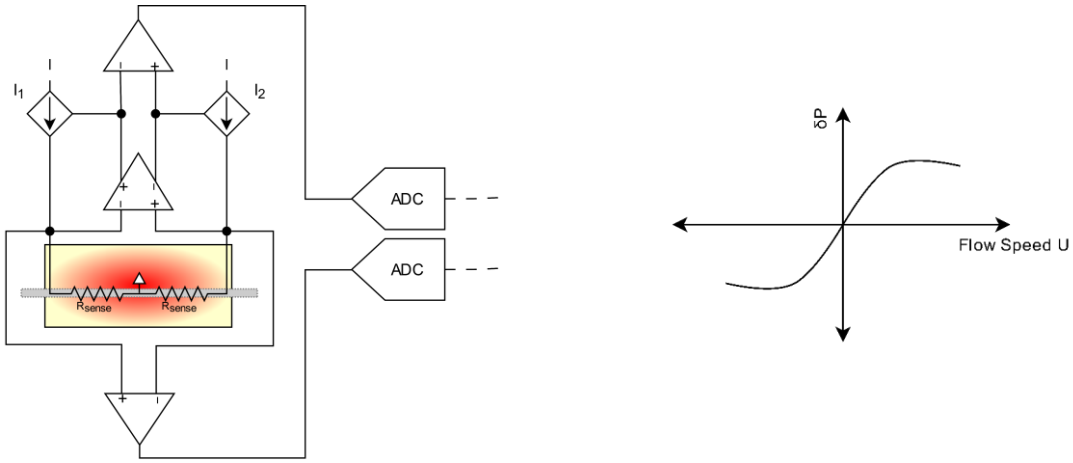

(a) Schematic Representation *(b)Flow speed vs differential power*

Fig. 2-9: CP-TB mode of operation of the Calorimetric sensor

The CTD-TB mode can be finally implemented by regulating the differential temperature and the overheat, resulting in the sensor being operated as a null detector. Thus, the read-out becomes independent of all the sensor-introduced limitations, such as slow response time and temperature-dependent non-linearities. A CTD-TB readout can be envisioned using a pseudo-differential architecture shown in Fig. 2-10 (a). The currents I_1 and I_2 will be regulated to ensure that the temperature of the sense resistors becomes equal to the desired overheat, ΔT. The flow vs δP curve is given in Fig. 2-10 (b). The δP is related to flow using eq. (2-6)

$$\frac{\delta P}{\Delta T} = SU^n \tag{2-6}$$

where S is a constant. The CTD-TB mode allows for fast and accurate flow response, however, at the expense of additional circuitry and an increase in design complexity.

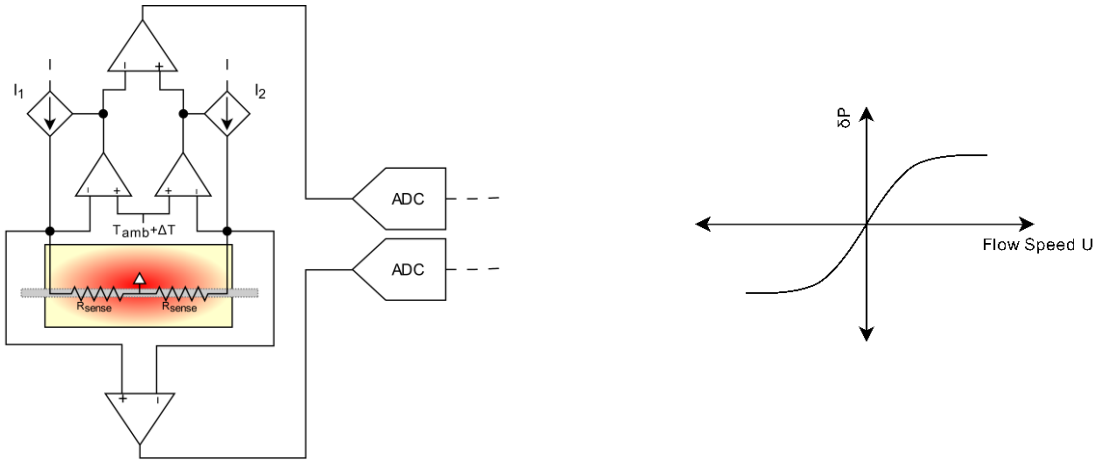

(a) Schematic Representation *(b)Flow speed vs differential power*

Fig. 2-10: CTD-TB mode of operation of the Calorimetric sensor

A summary of different operating modes for anemometric and calorimetric sensors is given in Table 2-1. Though the anemometric sensor interfaces described in section 2.2.1. are more straightforward than the calorimetric sensor interfaces described in section 2.2.2., they can only measure flow speed and not direction. Moreover, the bypass principle-based calorimetric flow sensor shown in Fig. 2-4 has a faster response time and higher sensitivity to low flows than the direct through-flow measurement-based anemometric sensor shown in Fig. 2-2. As a result, the calorimetric sensor is more widely used in low-flow applications requiring faster response times and was the chosen sensor for this project.

Table 2-1: Summary of different operating modes

Sensor Type	Sensing Mode	Measured	Constant	Equation
Anemometric Sensor	CP	ΔT	P	$\frac{P}{\Delta T} = A + BU^n$
	CTD	P	ΔT	$\frac{P}{\Delta T} = A + BU^n$
Calori metric Sensor	CP-TG	δT	P & δP	$\frac{\delta T}{P} = \frac{U^n}{C + DU^n}$
	CTD-TG	δT	ΔT & δP	$\frac{\delta T}{\Delta T} = SU^n$
	CP-TB	δP	P & δT	$\frac{\delta P}{P} = \frac{U^n}{E + FU^n}$
	CTD-TB	δP	ΔT & δT	$\frac{\delta P}{\Delta T} = SU^n$

Chapter 3. Thermal Sigma Delta Modulator

This chapter discusses the design of a TΣΔ based interface used to read out the calorimetric flow sensor shown in Fig. 2-4. The primary objective is to cancel the flow-induced temperature gradient (δT) by applying varying heating power to the two temperature-dependent resistors. The differential heating power (δP) can then be converted to flow speed using eq. (2-5) or (2-6) for CP-TB and CTD-TB modes, respectively. The read-out should be simple and cost-efficient. Thus, minimal circuitry is desirable.

The chosen topology to realize the flow-to-digital converter is a TΣΔM, which uses the sensor's thermal mass as the first integrator in the loop filter with the feedback DAC being formed by a power DAC. The bit-stream average will then be a digital representation of $\delta P/P_{DAC,}$ where P_{DAC} is the reference DAC power. However, the thermal mass is a passive-lossy integrator and provides no in-band gain, limiting the attainable resolution [10][38]. An electrical filter with high in-band gain can be added after the thermal filter to improve the performance of a TΣΔM [10]. The resulting second-order TΣΔM can attain higher resolution at the cost of an extra integrator in the loop.

This chapter starts with a brief overview of ΣΔ ADCs followed by an overview of TΣΔ ADCs. The key differences between the two types of ADCs are highlighted. The properties of a thermal mass, when being used as a filter, are explored. Then, the flow sensor's thermal mass modelling using circuit elements is discussed. A linearized mathematical model of the TΣΔM is developed for analysis, and then a more sophisticated circuit simulation model is created. The performance of the TΣΔM and its limitations are discussed, finally leading to the analysis and design of a second-order TΣΔM. This chapter discusses a simpler implementation of TΣΔM to interface the sensor in a CP-TB mode, and the CTD-TB interface is described in the following chapter.

3.1. Architecture Overview

This section will introduce the basic concepts of a ΣΔ ADC. The properties of a TΣΔ ADC will then be presented. The primary differences between a TΣΔ ADC and its electrical counterpart will be discussed in this section.

3.1.1. Sigma Delta ADC

An ADC consists of two primary operations – sampling, which is a discretization of time, and quantization, which is a discretization of amplitude. According to the Nyquist theorem, in a sampled system, the sampling frequency should be greater than or equal to twice the input signal bandwidth (f_{bw}) to uniquely recreate the original signal from the sampled signal [67]. ADCs operating at twice the signal bandwidth (2 f_{bw}) are called Nyquist ADCs, whereas ADCs operating at higher frequencies are called oversampling ADCs. While sampling is a lossless operation, quantization is a lossy operation and introduces a quantization error. Even though this quantization error is a deterministic signal, for high resolutions (> 7 bits [67]), this error can be approximated to be a statistical signal with "noise-like" characteristics. This quantization noise has a total power of $V_{LSB}^2/12$, uniformly distributed in bandwidth from -fs/2 to fs/2, where V_{LSB} is the ADC step size and is equal to full-scale input/2^N, where N is the ADC resolution. As shown in the single-sided spectrum of Fig. 3-1(a), for a Nyquist ADC, the entire signal band (f_{bw}) extends till fs/2; thus, all the quantization noise power is in-band. Oversampling reduces the total in-band quantization noise power by spreading it over a larger frequency range, as shown in Fig. 3-1(b). The effective ADC resolution can then be improved by using a decimation filter that filters the out-of-band quantization noise and down-samples the data back to Nyquist frequency. An oversampled ADC can thus achieve higher resolution than the quantizer used, allowing for ½ bit or

3dB improvement per doubling of sampling frequency. The ratio of sampling frequency (fs) to Nyquist frequency (2 f_{bw}) is called the Over-Sampling Ratio (OSR).

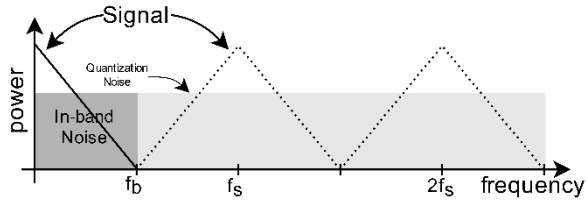

(a) Nyquist ADC

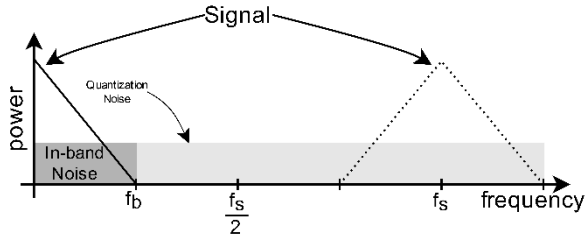

(b) Oversampled ADC

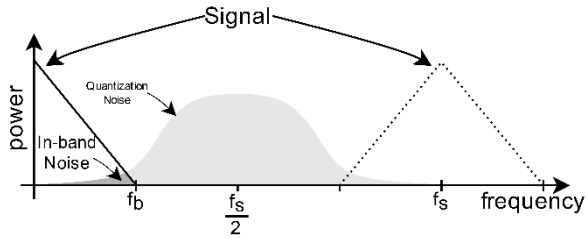

(c) Sigma-Delta ADC

Fig. 3-1: Single-ended signal and quantization noise spectrum of different ADCs

A ΣΔ ADC is a class of oversampled ADCs that consists of a ΣΔM followed by a decimation filter (Fig. 3-2). A ΣΔM is a closed-loop system where the low-frequency analog input signal, $V_{in}(t)$, is continuously balanced by a high-frequency digital bit-stream, bs(n). The digital bit-stream is converted to its equivalent analog value by a DAC and represents the instantaneous quantized value of the sampled loop filter output, which, in turn, represents the input signal. This value is subtracted (Δ) from the input to obtain the instantaneous quantization error, e(t), which is then integrated (Σ) by the loop filter. The feedback loop drives the average value of the quantization error to zero; thus, the average of the output bit-stream is representative of the input signal. The decimation filter is used to filter and down-sample the data.

A ΣΔM is highlighted in Fig. 3-2. A feature of a ΣΔM is that the loop filter (H(s)) has high gain at low frequencies. The loop gain reduces as the frequency increases. As a result, the loop filter shapes the quantization noise away from low frequencies and pushes it to higher frequencies, as shown in Fig. 3-1(c). This high-frequency noise can then be filtered and data down-sampled, allowing for more than a 3dB increase in resolution per doubling of OSR. The quantization noise shaping can be improved by increasing the order of the loop filter, H(s). As a rule of thumb, the in-band quantization noise power in a ΣΔM can be given by eq. (3-1) [34]

$$q_{rms}^2 = \frac{\pi^{2L} e_{rms}^2}{(2L+1)OSR^{2L+1}} \tag{3-1}$$

where L is the loop filer order, e is the quantization noise from the quantizer, and OSR is equal to $f_s/2f_{bw}$. ΣΔ ADCs allow for an improvement of L+0.5 bits per doubling of OSR and can thus achieve a resolution much higher than the resolution of the quantizer used. Note that this improvement of L+0.5 bits is only seen for a quantization noise-dominated ΣΔ ADC.

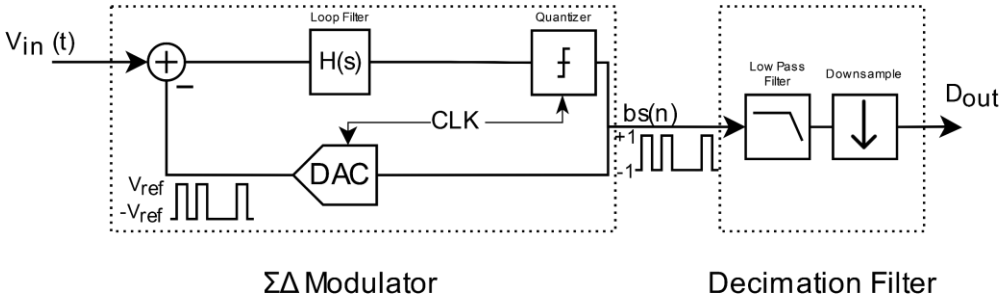

Fig. 3-2: Sigma Delta ADC

3.1.2. Thermal Sigma Delta ADC

A primary difference between a TΣΔ ADC and an electrical ΣΔ ADC is that the loop filter consists of a thermal mass, which acts like a low-pass filter [27] in the thermal domain, whose input is heating power, and whose output is a change in temperature. A temperature sensor converts the temperature to voltage for subsequent processing. A power DAC completes the feedback loop. In the case of thermal flow sensors, the TΣΔ ADC can be realized by integrating the sensor itself inside the sigma-delta loop. The TΣΔ loop cancels out the flow-induced temperature gradient (δT) using the feedback power DAC, which heats up or cools down the sensor depending upon the bit-stream output.

In the resistor-based thermal flow sensor used in this project, Joule heating can be used to realize the feedback power DAC, and the high TC of the resistors means that they can be used as temperature sensors. The resistors are, thus, used in a time-multiplexed manner as heating and sensing elements. The entire TΣΔ ADC can be built using a clocked comparator and power source in addition to the sense resistors. A microcontroller or an FPGA can directly read the output bit-stream for further processing with its average (μ_{avg}) representing $\delta P/P_{DAC}$.

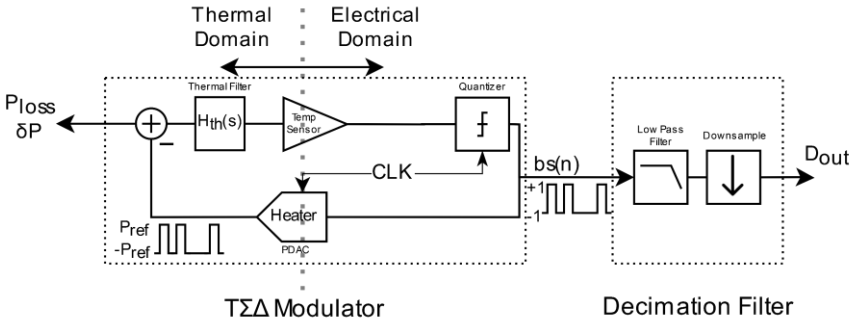

Fig. 3-3: Thermal Sigma Delta ADC

A TΣΔM uses a thermal mass as a passive low-pass filter to form the loop filter, as shown in Fig. 3-3. Thermal filters are half-order filters with a gentle roll-off of ~10 dB/decade [27] instead of the 20 dB/decade of electrical filters. As a result, the noise-shaping of the TΣΔM is limited, which limits its quantization noise suppression. Additionally, the thermal mass always leaks heat to its surroundings.

This limits the filter's DC gain, further limiting the modulator's performance. Moreover, the signal swings at the input of the quantizer depend on the sensitivity of the temperature sensor. As a result, the design of a TΣΔ needs careful analysis and characterisation of the thermal flow sensor. An electrical integrator can be added to improve the performance of a TΣΔ ADC by increasing the in-band gain and making the system less susceptible to thermal mass properties [29]. The resulting second-order TΣΔ ADC, shown in Fig. 3-4, has improved noise shaping and DC characteristics.

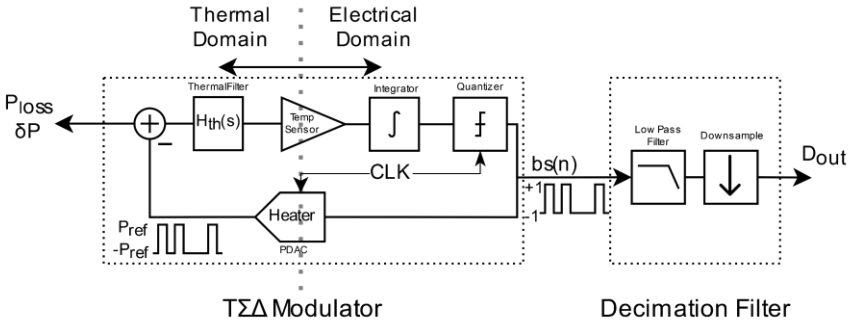

Fig. 3-4: Second-order Thermal Sigma Delta ADC

3.2. Thermal Low Pass Filter

In this section, a model of the flow sensor's thermal mass is developed. To allow for the simulation of the TΣΔM using circuit simulators like LTSpice and Cadence, we aim to find a network of simple electrical components that shows the same response for a given excitation as shown by the actual sensor. To that end, we seek to develop an RC ladder network [68] with finite segments that emulate the behaviour of thermal mass.

3.2.1. Thermal Filter Model

We start by looking at the well-known thermal parameters and their analogous electrical counterparts in Table 3-1. The behaviour of any thermal mass can be modelled by subdividing it into a number of finite elements and considering each element as a thermal low-pass filter with thermal resistance and thermal capacitance [69]. In the resistor-based flow sensor used, the node of excitation is the same as the node of observation, i.e., the point where the heating power is applied is the same as the point where the temperature change is measured, the system behaves like an RC driving-point impedance [10]. Some properties of this thermal impedance ($Z_{th}(s)$) can thus be derived from network theory [70], which tells us that RC driving point impedance is a positive real function ($s=j\omega$) with the following properties:

A. The poles and zeros are simple and lie on the negative real axis.
B. The partial fraction expansion of $Z_{th}(s)$ gives real and positive residues.
C. The poles and zeros interlace (alternate) on the negative real axis.
D. The critical frequency nearest to the origin is always a pole and might be located at the origin, whereas the critical frequency furthest from the origin is always a zero and can be at infinity.

Table 3-1: Thermal Properties and their analogous electrical counterpart

Thermal Parameter	Units	Electrical Parameter	Units
Temperature	K	Voltage	V
Heat Flow	W	Current	A
Heat	J = Ws	Charge	Q = As
Resistance	K/W	Resistance	Ω = V/A
Capacitance	J/K	Capacitance	F = Q/V

Some qualitative assessments of the thermal filter can be made based on these properties. A and B mentioned above mean that $Z_{th}(s)$ can be expressed by a general eq. (3-2)

$$Z_{TH}(s) = \frac{K_1}{s+\sigma_1} + \frac{K_2}{s+\sigma_2} + \cdots \tag{3-2}$$

where K_i and σ_i are both real and positive. Eq. (3-2) can be graphically represented by a series of RC segments shown in Fig. 3-5(a). This is called a Foster network [70] and is a commonly known form used to represent a thermal impedance. The Foster network, however, does not correspond to a physical representation of a thermal mass. This is because the Foster network comprises of floating capacitances, which is impossible in the thermal domain that only has capacitances to the ground [71] (ground refers to ambient temperature). A Foster network can be transformed into its Cauer equivalent by using standard procedures from linear circuit theory [70]. The Cauer network (Fig. 3-5(b)) has only node-to-ground capacitances and is thus a plausible physical representation of a thermal mass. Note that these networks are a discretized representation of the continuous heat-flow structure of a thermal mass [72]. An actual representation of thermal impedance consists of an infinite distributed RC network with a continuous spectrum of time constants [27]. However, since our goal is to create a model of the thermal mass that can be used for the simulation environment, a simple Foster network was preferred.

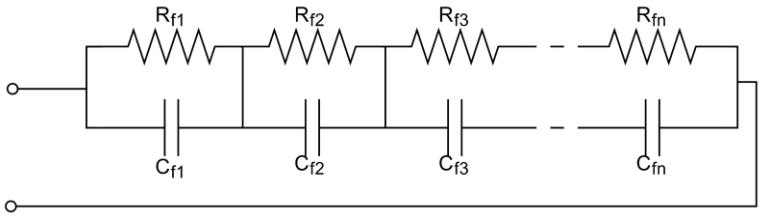

(a) Foster Network

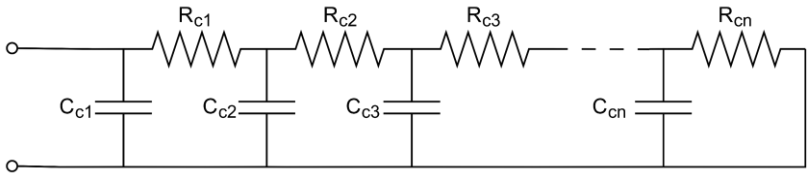

(b) Cauer Network

Fig. 3-5: Electrical Realization of Thermal Filters (Zth(s))

Properties C and D are graphically visualised in Fig. 3-6, showing that $Z_{th}(s=j\omega)$ must have low pass characteristics. The interlaced poles and zeros with the critical frequency near the origin as the pole and farthest from the origin as zero indicates that the slope of this low pass filter, when approximated by a straight line, can assume any arbitrary value between 0 and 20 dB/decade, depending upon the relative position of the poles and the zeros. As a result, the thermal mass can have a phase shift of 90˚ at most at high frequencies, which results in the TΣΔM being unconditionally stable. The second-order TΣΔM, as a consequence, can be designed to be stable without the need for any compensation path [10][31]. This is because, theoretically, the combined phase shift of the second-order TΣΔM tends to 180˚ only at very high frequencies.

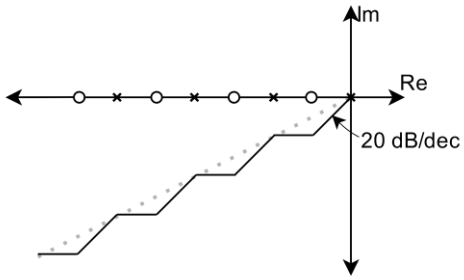

Fig. 3-6: Pole-Zero representation of an RC Driving point impedance

3.2.2. Experimental Characterization of Thermal Mass

With a theoretical understanding of the expected thermal model, we can now create a model for our resistor-based calorimetric flow sensor, which can be used for simulations. A highly accurate sensor model can be obtained using 3-D Finite Element Analysis. Such an approach, however, requires prerequisite knowledge of the material type, the glue and the foam and is computationally intensive. Another approach is to model the thermal mass experimentally from the measured step response [10][73]. This approach allows for an accurate modelling of the sensor's thermal mass without any prerequisite knowledge about the sensor construction.

The experimental setup is shown in Fig. 3-7. The sensor is initially biased with 100µA current for a long time to allow it to reach a steady state. Then, an input step of 35mA (equivalent power step of 110 mW) is applied using YOKOGAWA GS200. An external function generator, 33220A Agilent, triggers the current step and marks the start of conversion. The same clock is used to trigger the start of data logging on the NI PCI-6363 DAQ board - the DAQ board features a 16-bit SAR ADC capable of operating at 2MSamples/s. The sensor is buffered using high-precision, low-noise amplifiers (MAX44246) to prevent loading the sensor output by the ADC. An anti-aliasing filter (AAF) is also added after the buffer to remove the high-frequency content. Since the bandwidth of interest for the sensor is relatively low (<10kHz), the corner frequency for the AAF is chosen to be 100kHz.

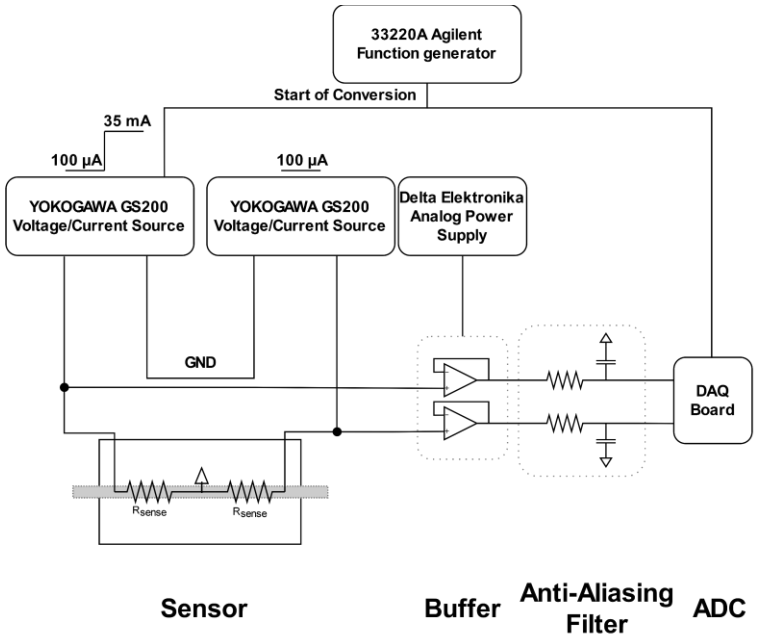

Fig. 3-7: Measurement Setup for Modelling of Thermal Mass

The output voltage (V) read via the DAQ board can then be converted to temperature using eq. (3-3)

$$\Delta T = \frac{\left(\frac{V}{IR_0} - 1\right)}{\alpha} \tag{3-3}$$

where I is the current applied to the sensor and is equal to 35mA, R_0 is the nominal resistance at 20˚C and is equal to 90 Ohm, and α is the temperature coefficient of the resistor and is equal to 3200 ppm/Ƙ. The dynamic response of the measured curve will be governed by the general RC charging eq. (3-4) [27] where τ denotes the time constant and equals $R_{th} * C_{th}$. The values of R_{th} and C_{th} from eq. (3-4) can be directly mapped to the components of the Foster network of Fig. 3-5 (a).

$$Z_{th}(t) = R_{th1}\left(1 - e^{-\frac{t}{\tau_1}}\right) + R_{th2}\left(1 - e^{-\frac{t}{\tau_2}}\right) + R_{th3}\left(1 - e^{-\frac{t}{\tau_3}}\right) + \cdots R_{thn}\left(1 - e^{-\frac{t}{\tau_n}}\right) \tag{3-4}$$

An algorithm was developed to model the thermal filter, which fitted the measured response, ΔT, to $P * Z_{th}$, where P is the known power input and the parameters of Z_{th}, given in eq. (3-4), were the results of the fitting algorithm. Experimentally, 38 RC segments were found, which resulted in the relative error being less than ± 2.5% of the measured value. A smaller number of segments results in worse accuracy, whereas a larger number of segments did not improve the same. A more sophisticated algorithm can be explored to improve the modelling accuracy; however, 38 RC segments with a ± 2.5% modelling accuracy were the best we achieved within the given time constraint. The fitting results, along with measurement results, are shown in Fig. 3-8. The details of the fitting algorithm are given in Appendix A.

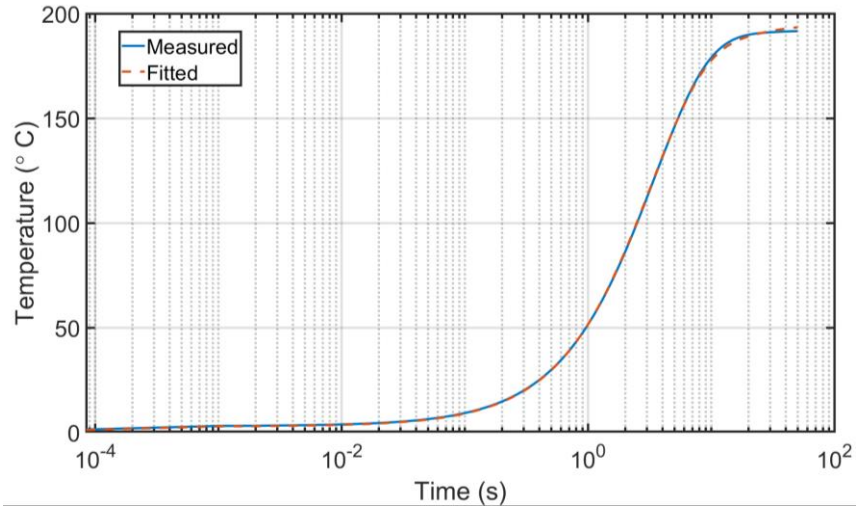

Fig. 3-8: Measured and Fitted step response of the Thermal Flow Sensor

The frequency response of the modelled system is shown in Fig. 3-9. Note that discretizing the continuous spectrum of time constants results in the system having a non-uniform slope across the frequency range. When approximated by a straight line (dashed line in Fig. 3-9), the thermal mass has a 10dB/decade slope, indicating that the poles and zeros are nearly equally spaced [27]. However, as will be shown in the measurement results of Chapter 4, the model developed predicts only the low-frequency behaviour correctly, and the high-frequency behaviour is not modelled very well. This limitation in modelling is primarily due to the finite accuracy of MATLAB convergence algorithms used and time constraints. Nominally, the bode plot of Fig. 3-9 tells us that a stable second-order TΣΔM can be built without any feedforward or feedback compensation (as also shown in [10][31]). However, a provision to add a feedforward zero in the design was kept, which will be elaborated on in Chapter 4. In practice, it was found that the modulator can be made stable for the target application without any compensation and achieved the desired resolution, which the model predicted well.

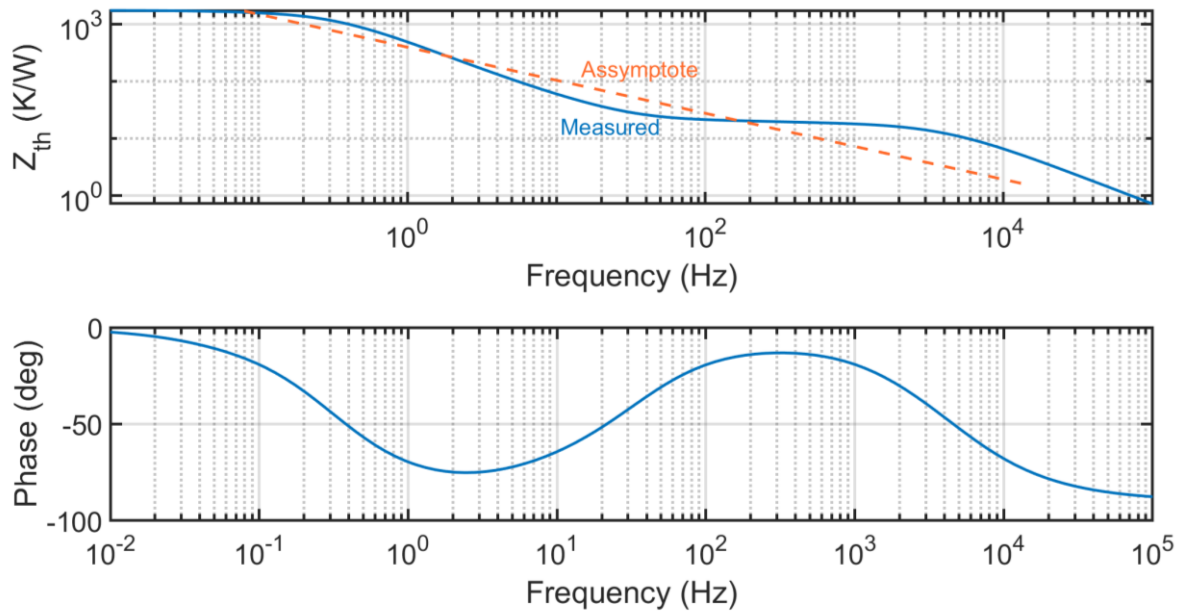

Fig. 3-9: Bode Plot of the modelled foster network representing Thermal Flow Sensor

3.3. Modelling of TΣΔM

This section describes the system-level modelling of the TΣΔM. The Foster network of the thermal mass, developed in section 3.2.2., serves as the model of the first "passive" integrator in the ΣΔ loop. In this section, a TΣΔM will first be analyzed using a linearized mathematical model, followed by numerical simulations on a non-linear model built in a circuit simulator. This section also explores a similar analysis of the second-order TΣΔM.

3.3.1. TΣΔM

3.3.1.1. Linearized Analysis

A ΣΔM consists of a loop filter, a quantizer and a feedback DAC. A quantizer is a low-resolution ADC and highly non-linear block, making the linear analysis of a ΣΔM difficult. A popular approach is to replace the non-linear quantizer with a linear gain block and additive noise to model the quantization noise. However, defining the gain of a binary quantizer is challenging as the input-output curve can be approximated by a line of any slope [34].

The gain of a quantizer is given by eq. (3-5):

$$\kappa = \frac{D_{OUT,rms}}{V_{IN,rms}} \tag{3-5}$$

where $D_{OUT,rms}$ is the rms value of the digital output code and $V_{IN,rms}$ is the rms value of the quantizer input voltage. For a binary quantizer, the digital output is always +1 or -1. Thus, $D_{OUT,rms}$ of a 2-level quantizer is always 1, and the gain is inversely proportional to the input voltage swing. From [34], the gain of a binary quantizer can be determined by a statistical approximation given in eq. (3-6)

$$\kappa = \frac{E[\overline{V_{IN}}]}{E[V_{IN}^2]} \tag{3-6}$$

which results in an average value of the quantizer gain. Thus, a linear model of the TΣΔM (Fig. 3-10) can be realized by using the thermal mass transfer function ($H_{th}(s)$) as the loop filter, the PTC resistor forming the temperature sensor, the transfer function ($H_e(s)$) of which is its sensitivity, the linearized

approximation of the binary quantizer, and the feedback power-DAC being formed by the resistors used as heaters. The input to the TΣΔM will be differential heat-loss (δP) needed to compensate for the differential temperature (δT) created due to fluid flow. Although the linear model only approximates the actual behaviour of the TΣΔM, it allows us to analyze it and build an intuition about the system behaviour. It also provides valuable insights into the modulator's stability and noise performance.

In Fig. 3-10, W_n is the wind noise – the noise generated due to the random motion of particles in the flow tube [74]. The V_{en} is the thermal noise of the temperature sensor and interface electronics. The quantizer is modelled as a variable gain block with a gain, κ, and quantization noise, V_{qn}. Since this work is focused on developing the read-out for an existing flow sensor, the effect of W_n, which is strongly influenced by the sensor's properties, is considered beyond the scope of this thesis and will be neglected in the subsequent discussion.

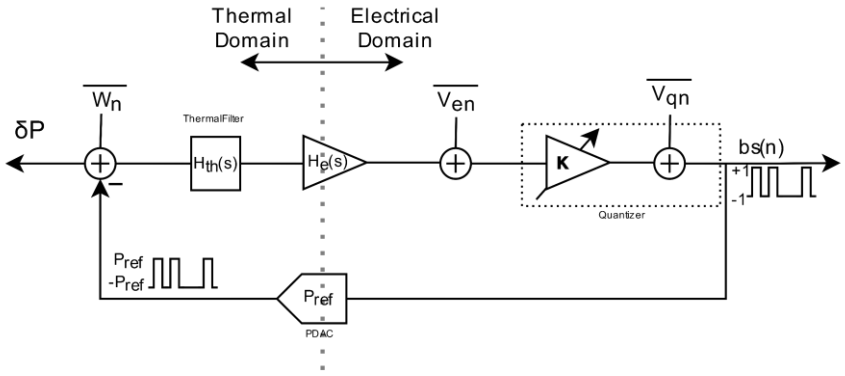

Fig. 3-10: Linear Model of a TΣΔM

From Fig. 3-10, the output (V_0) of the modulator can be written by multiplying the various signal and noise sources with their respective transfer functions as given in eq. (3-7)

$$V_0 = STF\ \delta P + NTF_{en}V_{en} + NTF_{qn}V_{qn} \tag{3-7}$$

where δP is the differential heat loss to flow, and the STF denotes the Signal Transfer Function from input to output. V_{en} is the thermal noise from the interface electronics, and NTF_{en} is the Noise Transfer Function (NTF) from the output of the sense resistors to the modulator output. V_{qn} is the quantization noise, and NTF_{qn} is the Noise Transfer Function (NTF) of the quantization noise to the output. The STF is given in eq. (3-8).

$$STF = \frac{H_{th}(s)H_e(s)\kappa}{1 + P_{ref}H_{th}(s)H_e(s)\kappa} \approx \frac{1}{P_{ref}} \tag{3-8}$$

If the term $P_{ref}H_{th}(s)H_e(s) \gg 1$, the STF can be approximated to be inversely proportional to the power of the feedback DAC. Since a ΣΔM has a large low-frequency gain, this approximation becomes more accurate for higher OSR, and the average value of the output is normalized to feedback DAC power. This result is not surprising as the bit-stream average of a ΣΔM represents input normalised to the DAC reference. The input of the TΣΔ being δP, the average output will thus be $\delta P/P_{ref}$. The NTF_{en} is given by eq. (3-9).

$$NTF_{en} = \frac{\kappa}{1 + P_{ref}H_{th}(s)H_e(s)\kappa} \approx \frac{1}{H_{th}(s)H_e(s)P_{ref}} \tag{3-9}$$

The noise at the output of the electrical interface is thus shaped by the inverse of the product of the thermal filter's transfer function, the temperature sensor's sensitivity, and the feedback DAC's power.

The thermal mass has low pass filtering characteristics. Thus, the thermal noise is high pass filtered at the output. Since we have no control over the thermal mass's filtering properties or the temperature sensor's sensitivity, increasing the DAC reference power is the only way to reduce the in-band thermal noise. Ultimately, this is limited by the maximum instantaneous power allowed in the sense resistors. As will be shown in the next chapter, the choice of the DAC power was then dictated by the required overheat temperature while operating in the safe region of the sensor. The NTF_{qn} is given by eq. (3-10).

$$NTF_{qn} = \frac{1}{1 + P_{ref} H_{th}(s) H_e(s) \kappa} \approx \frac{1}{H_{th}(s) H_e(s) P_{ref} \kappa} \tag{3-10}$$

Thus, the quantization noise is shaped by a product of the inverse of the thermal filter transfer function, the temperature sensor's sensitivity, the DAC reference power, and the quantizer gain. From eq. (3-9) and (3-10), we see that the quantizer gain (κ) should be sufficiently high to ensure that the quantization noise is suppressed below the thermal noise. However, the binary quantizer gain, κ, given in eq. (3-6), depends on the quantizer input signal. Thus, we cannot control or optimize the quantizer gain. We can improve the quantization noise suppression by adding an electrical filter after the thermal filter, resulting in a second-order TΣΔM. For a given OSR, we can also reduce the quantization noise by increasing the quantization steps. However, this multi-bit TΣΔM is challenging as the swings at the sensor's output strongly depend on the thermal filter properties and the temperature sensor's sensitivity. For the sensor used in this project, swings are expected to be in the order of a few hundred µVs, which would need the quantizer threshold levels down to a few uVs, making the multi-bit quantizer design challenging.

From equations (3-7), (3-8), (3-9), and (3-10), we can now write the output of the linearized modulator as given in eq. (3-11)

$$V_o = \frac{\delta P}{Pref} + \frac{V_{en}}{H_{th}(s) H_e(s) P_{ref}} + \frac{V_{qn}}{H_{th}(s) H_e(s) P_{ref} \kappa} \tag{3-11}$$

The linearized model, though instructive, is only an approximation of the real non-linear system. Moreover, quantizer gain, κ, given by eq. (3-6), is a statistical approximation and requires extensive time-domain simulations. As a result, we now move on to the non-linear simulation model for the TΣΔM and revisit the equations developed in this section later.

3.3.1.2. Simulation Model

This section will describe a model of the TΣΔM created in a circuit simulator. First, the model of the flow sensor developed is explained. To use the same PTC resistor for heating and sensing, the TΣΔM reads out the sensor in a time-multiplexed manner, which will be described in this section.

The electro-thermal model of the flow sensor is shown in Fig. 3-11. A single-ended model is shown for simplicity; however, the real implementation uses a fully differential model. The current input, I_{in}, develops a voltage across the resistor R_{sense}, V_{in}. The resistor also heats up due to I^2R losses, which increases the sensor's temperature. The power input into the thermal mass, $I_{in}^2 R_{sense}$, is modelled in the following manner: First, a voltage-controlled voltage source (vcvs) with a gain of $1/R_{sense}$ is used, which converts the voltage input, V_{in}, to its equivalent current value resulting in output voltage $V_1 = V_{in}/R_{Sense}$. V_1 is multiplied by V_{in} using the voltage multiplier block to get an output voltage, V_2, which is the power input to the thermal mass. We proceed now into the thermal domain, keeping in mind the electro-thermal equivalence from Table 3-1. The power input, V_2, is first passed through a voltage-controlled current source (vccs) with a gain of 1 to generate a current, W. This power (current) input results in a change in the temperature (voltage), T, the dynamic response of which is governed by the thermal mass transfer function, H_{th}. This temperature is then converted back into a voltage by the PTC

resistor. This is achieved again via a vcvs with an offset of 1 and gain of α (=3200ppm/K), which results in an output voltage, V_4, equal to 1+αΔT. Finally, a voltage multiplier block multiples V_4 with V_{in} to generate $V_{out} = I_{In}*R_{sense}(1+\alpha\Delta T)$.

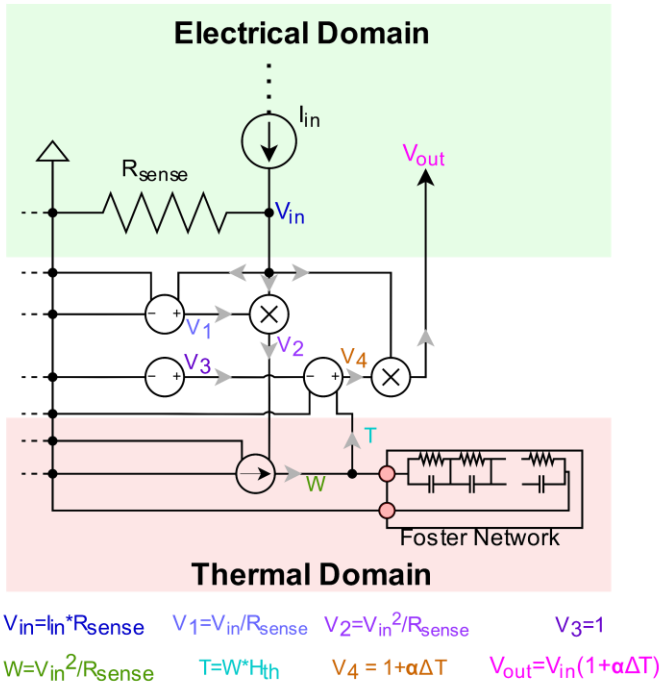

Fig. 3-11: The electro-thermal model of the Flow Sensor

The thermal flow sensor is then integrated into a TΣΔ loop with the feedback power-DAC being formed by a current source and the sense resistors (Fig. 3-12). The system is read out in a time-multiplexed manner. The need for this can be realized by seeing the two effects that happen simultaneously when the DAC is connected: there is a large voltage change due to IR drop (in order of a few Volts) and a small voltage change due to heating of the resistors (in order of a few hundred µVs). Since the relevant information is present only in the latter voltage change, which contains the information about the temperature changes, we need to eliminate the influence of the large IR drop. This is possible by disconnecting the DAC current source for a part of the total clock period. The temperature change, governed by $H_{th}(s)$, will slowly decay, whereas the IR drop will be removed nearly instantaneously. Thus, the feedback DAC will be disconnected during a part of the clock period called the "sensing" phase (Fig. 3-13), during which the modulator decision would be taken. Based on this decision, the feedback current source DAC will be connected to the relevant resistor when the modulator enters the "heating" phase (Fig. 3-13). The resulting time-multiplexed system is equivalent to a Return-to-Zero (RZ) feedback DAC in a ΣΔM. Fig. 3-13 shows the timing diagram of the proposed TΣΔM, where US represents the feedback to the top sense resistor and DS represents the feedback to the bottom sense resistor. Note that the feedback DAC must be disconnected during the sensing phase when the quantizer takes the decision; otherwise, the proposed TΣΔ will always toggle at fs/2, and we will lose all flow information.

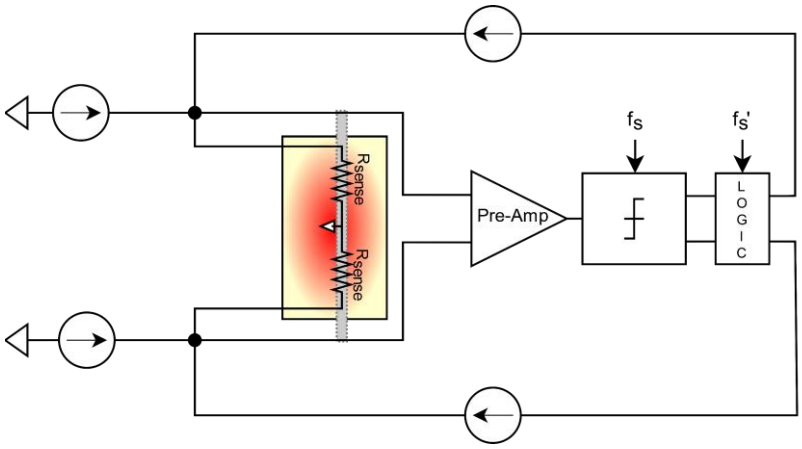

Fig. 3-12: Simulation Model of TΣΔM

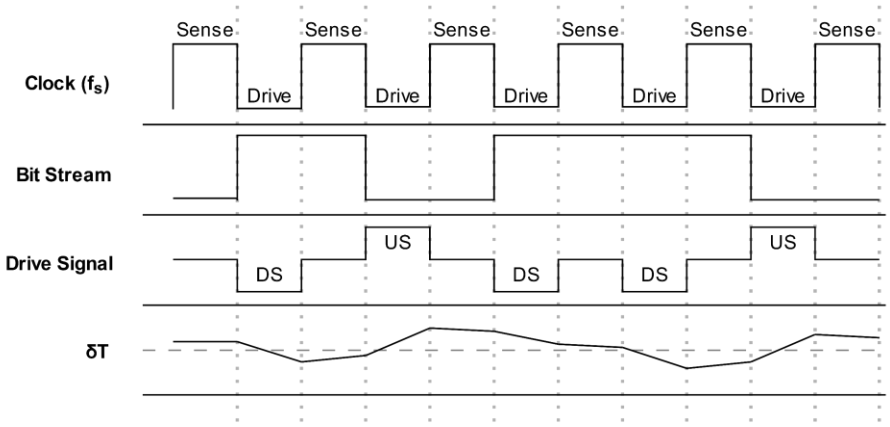

Fig. 3-13: Clock Diagram of TΣΔM

A pre-amp with a 40 dB gain is used before the comparator to amplify the signal swing at the output of the thermal mass. For the TΣΔM with the flow sensor used in this work, a total noise density of 10 nV/√Hz, referred to the output of the sense resistors, ensures that the target resolution (~13 bits) in the desired BW (~1.5 Hz) is met with a sufficient margin. With the aim of having a thermal noise-dominated system, the input-referred noise density of the Pre-Amp, $V_{en,}$ was chosen to be a conservative 10 nV/√Hz for this simulation (the differential noise of the sense resistors of 90Ω is 1.73 nV/√Hz and hence will cause the thermal noise to increase to 10.15 nV/√Hz). The total quantization noise power density will be given by eq. (3-12)

$$\overline{V_{qn}^2} = \frac{\Delta^2}{12}\frac{1}{f_s} \tag{3-12}$$

where Δ is the step size of the quantizer (=2 for a binary quantizer). The sampling frequency, f_s, was chosen to be 5kHz to ensure a sufficiently high OSR for these simulations. The feedback DAC power was chosen to be ~20mW (current of 21mA with 50% Duty Cycle (DC) of RZ DAC) to ensure sufficiently high feedback DAC power while staying in the safe operating region of the sensor. Multiple simulations were performed with the given parameters, and then eq. (3-6) was used to find the quantizer gain.

With all the required parameters now known, we can use eq. (3-11) to find the output referred noise spectral density of the TΣΔM, as shown in Fig. 3-14. It also shows the contribution of the quantization noise and thermal noise to the total output noise. Fig. 3-14 also shows the results of the non-linear model from the circuit simulator. The two systems show similar noise-shaping performance, especially in the low-frequency domain; thus, the linear model can be used to make quick, first-order

approximations. However, the simulation results show a peak in the spectrum. This is primarily due to the limit cycles commonly seen in a first-order modulator due to finite loop gain [34]. Note that these limit cycles do not indicate modulator instability, as the amplitude of these peaks does not change with time and is a function of the input signal. As will be shown later, the linearized analysis becomes more and more valid as the order of the modulator increases and the assumptions made about the quantizer and the quantization error become more valid.

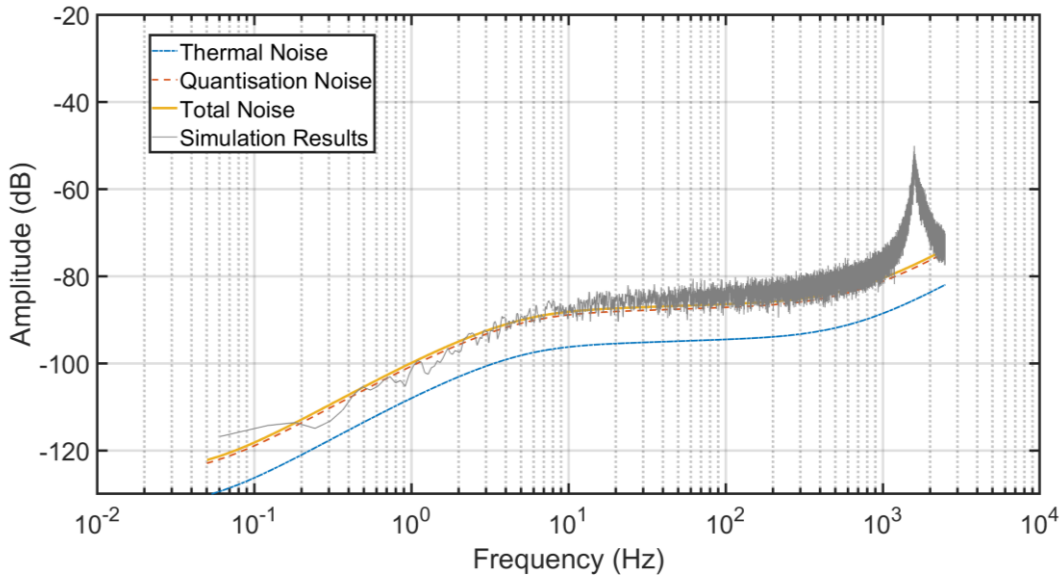

Fig. 3-14: Noise Spectral Density of TΣΔM

From Fig. 3-14, we can see that the proposed system with the proposed sampling frequency will be dominated by quantization noise. As a result, the system will not meet the resolution requirements in the target bandwidth. A potential solution could be to increase the sampling frequency, fs, which suppresses the quantization noise further in a ΣΔM, partly due to the noise spreading effect and partly due to the increased quantizer gain [31]. However, this effect is less dominant in a TΣΔM because the slow thermal mass cannot respond to high-frequency DAC pulses and, thus, behaves asynchronously if fs is too high. An accurate model of the thermal filter's high-frequency behaviour can predict the same from simulations, as shown in [31]. However, the limited modelling accuracy of the thermal mass in this work did not show this behaviour in simulations, but it was observed in measurements as will be shown in Chapter 4.

3.3.2. Second-Order TΣΔM

3.3.2.1. Linearized Analysis

To improve the resolution of the TΣΔM, an electrical filter can be added after the thermal filter to increase in-band gain, further suppressing the in-band quantization noise. The block diagram of the second-order TΣΔM is shown in Fig. 3-4. This model can then be used to create a simplified-linearized model by following the same approach as section 3.3.1.1. The linearized model with the various noise sources is shown in Fig. 3-15.

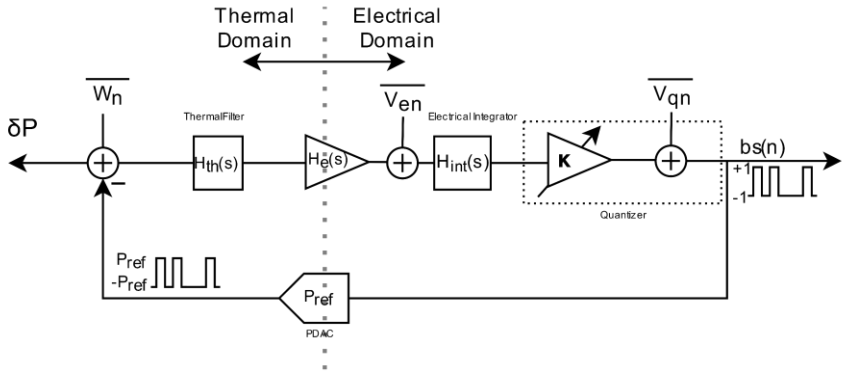

Fig. 3-15: Linear Model of a second-order TΣΔM

The noise, V_{en}, now depicts the total noise of the read-out chain, referred to the output of the sense resistors, including the noise of the sense resistors. Representing total electronic noise by V_{en} means that the modulator transfer function remains the same as eq. (3-7), and STF and NTF_{en} can be approximated by the equations (3-8) and (3-9), respectively. However, the quantization noise transfer function, NTF_{qn}, changes significantly due to the electrical integrator in the loop. NTF_{qn} will now be given by eq. (3-13)

$$NTF_{qn} = \frac{1}{1 + P_{ref}H_{th}(s)H_e(s)H_{int}(s)\kappa} \approx \frac{1}{H_{th}(s)H_e(s)P_{ref}H_{int}(s)\kappa} \tag{3-13}$$

where $H_{int}(s)$ represents the transfer function of the electrical integrator. The output of the second-order TΣΔM can thus be given by eq. (3-14)

$$V_o = \frac{\delta P}{Pref} + \frac{V_{en}}{H_{th}(s)H_e(s)P_{ref}} + \frac{V_{qn}}{H_{th}(s)H_e(s)P_{ref}H_{int}(s)\kappa} \tag{3-14}$$

Now, we build the non-linear simulation model of the proposed second-order TΣΔM to find the quantizer gain, κ. Note that the presence of an integrator in the loop means that the swings at the input of the quantizer will change, and hence, using the same gain as the first-order TΣΔM can give misleading results.

3.3.2.2. Simulation Model

The non-linear simulation model of the second-order TΣΔM is shown in Fig. 3-16. The model is based on the TΣΔ model of Fig. 3-12, where an electrical integrator was added in the loop. For simulations, the electrical integrator was implemented as an OTA-RC integrator with a unity gain frequency of 17.5kHz. The total input referred noise of the read-out was maintained at 10 nV/√Hz (i.e., the noise was dominated by the pre-amp, which suppresses the noise of the further stages sufficiently).

The proposed second-order TΣΔM differs from the first-order TΣΔM in one other crucial way: the integrator (and thus the following interface) needs to be disconnected during the drive phase (Fig. 3-13) of the modulator. As discussed in section 3.3.1.2., when the feedback DAC is connected, there is a large IR drop in the order of a few Volts, whereas the change in voltage due to temperature rise is in the order of a few hundred µVs. Since the relevant information is only present in the latter voltage change, if the interface is not disconnected, the Continuous-Time (CT) OTA RC integrator output will be dominated by the IR drop instead of voltage change due to temperature variation; thus, it would no longer operate as a TΣΔM, and we would lose all flow information.

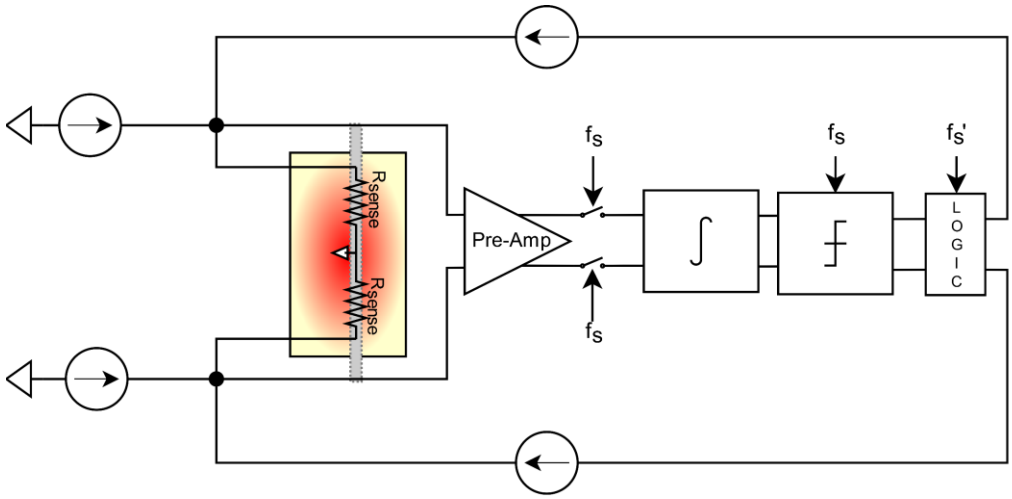

Fig. 3-16: Simulation Model of second-order TΣΔM

The quantizer gain was found from the simulations and eq. (3-14) was used to estimate the output noise spectrum. The results are shown in Fig. 3-17. We can see that adding the second integrator helps suppress the quantization noise below the thermal noise floor in the BW of interest. The resulting second-order TΣΔM can thus achieve a thermal noise-limited output spectrum in the BW of interest. The ADC resolution will now depend on the design of the interface electronics and their respective input referred thermal noise floor. The simulation results are also shown in Fig. 3-17, which shows a similar shaping as the linearized model.

From Fig. 3-17, an interesting observation is that the second-order TΣΔM output spectrum is shaped in the BW of interest even though it is dominated by thermal noise. A thermal-noise dominated ΣΔM [34] and TΣΔM [10][31] show a flat noise power spectrum in the BW of interest. This is because in a conventional ΣΔM, the noise of the stages after the first integrator is usually suppressed sufficiently by the first integrator. However, in the case of TΣΔM, the dominant noise source is the Pre-Amp, the noise of which, when referred to the output, is shaped by the thermal filter transfer function. As a result, the second-order TΣΔM has an interesting output spectrum with two slopes, the shaped thermal noise-dominated slope of ~10dB/decade and the quantization noise-dominated slope of ~30 dB/decade.

3.4. Conclusion

This chapter discussed the design of a cost-efficient read-out to interface a flow sensor in TB mode by putting the sensor in first-order and second-order TΣΔ loops. The modelling of the thermal mass, which is used as the first filter in the ΣΔ loop and is thus crucial to ensure the modulators' stability as well as shaping performance, is discussed in detail. Linear models of first and second-order TΣΔMs are developed to obtain an intuitive understanding of the modulators' behaviour. This was then followed by numerical simulations of the actual non-linear system.

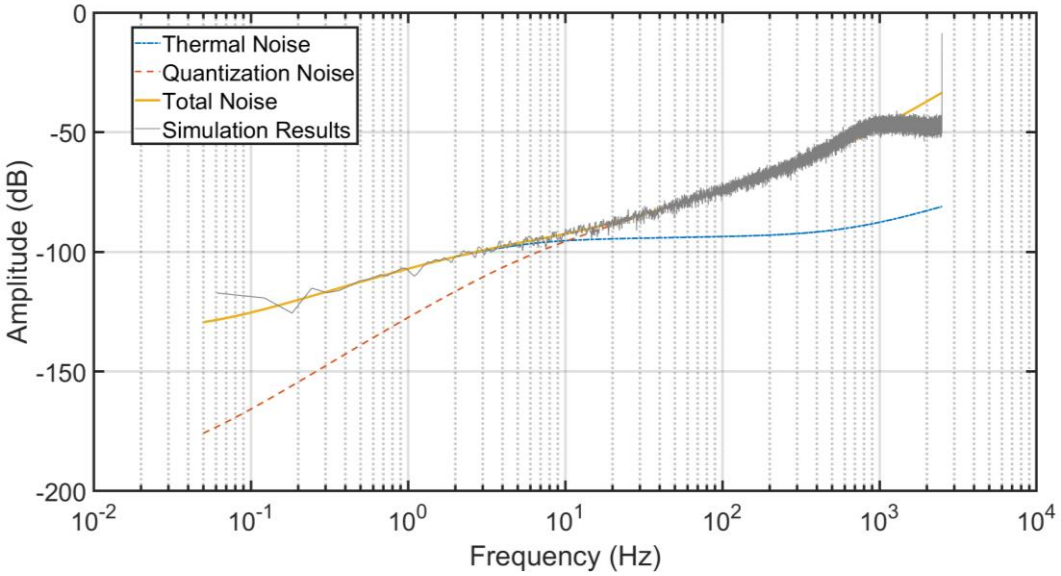

Fig. 3-17: Noise Spectral Density of second-order TΣΔM

Chapter 4. Flow Sensing using TΣΔM

This chapter discusses the implementation of a second-order TΣΔ interface to read out the calorimetric flow sensor. The second-order TΣΔM can be implemented with an amplifier, an integrator, a comparator, and a feedback current DAC in addition to the flow sensor. It is a simple- and cost-effective way to implement a flow-to-digital converter with high resolution and fast dynamic response.

This chapter starts by highlighting the target specifications for the desired flow-to-digital converter and the corresponding requirements from the second-order TΣΔM. Afterwards, the final architecture and the prototype design of the second-order TΣΔM are presented, in which the sensor operates in a CTD-TB mode while meeting the target specifications. Then, the results of the top-level simulations of this architecture are presented. This chapter concludes with the measurement results of the prototype modulator built using discrete components.

4.1. Requirements

The proposed flow-to-digital converter will be used as a commercial product (flow meters and controllers) with a targeted accuracy of ~10 bits. Then, to have a safe margin for quantization errors, the read-out should target a 13-bit resolution.

To understand what this means for the modulator design, we must first establish how much differential power (δP) must be compensated by the loop for a full-scale flow input of 7mL/min (set by sensor construction). We begin with the flow-to-temperature transfer curve of the calorimetric flow sensor when operated in an open-loop (CP-TG). This test was carried out by biasing the sensor with a constant current source of 15.3 mA. This results in an overheat of approximately 35˚C, which offers a good compromise between high sensitivity and long-term stability (information provided by Bronkhorst). Due to fluid flow, the sensor will cool asymmetrically, generating a differential temperature, δT, which can then be converted to a differential voltage due to the PTC of the resistors. This voltage can be read out via a difference amplifier and will be a function of the differential temperature as given by eq. (4-1)

$$\Delta V = IR_0\alpha(\Delta T_1 - \Delta T_2) \tag{4-1}$$

where I is the current input and equal to 15.3 mA, R_0 is the nominal resistance value of the sense resistors and equal to 90 Ω, α is the temperature coefficient and is equal to 3200 ppm/K, and ΔT_1 and ΔT_2 are the resistors' overheat temperatures above the nominal temperature at which the value R_0 is defined (= 20˚C). Fig. 4-1(a) depicts the δT created as a function of fluid flow. Using the electro-thermal equivalence of Table 3-1, we can convert this δT to δP by dividing it by the total thermal resistance, R_{th}, found in section 3.2.2. The transfer curve of δP to flow is shown in Fig. 4-1(b).

From Fig. 4-1(b), we can see that a full-scale flow rate of 7mL/min needs a differential heating power of about 3.75 mW. For 13-bit resolution (or 80 dB SNR), this means that the total input referred integrated noise in the BW of interest should be 0.375µW_{rms}.

The BW of the read-out needs to be large enough to ensure that the transient response is dominated by the sensor and not by the read-out electronics. Since the thermal sensor has a dominant time constant of ~1s, the bandwidth of interest was conservatively chosen to be 1.5Hz.

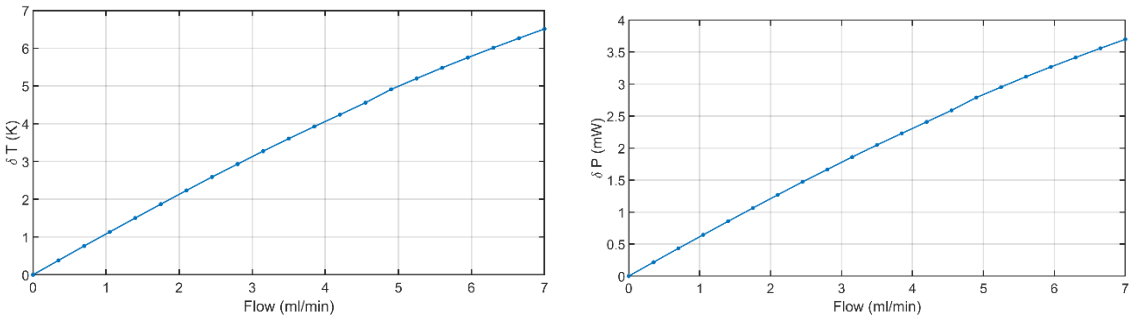

(a) Flow vs δT *(b) Flow vs δP*

Fig. 4-1: Flow vs differential temperature (a) and power (b) transfer curves

With the BW and total input referred integrated noise known, we can now calculate the maximum allowed thermal noise density of the interface electronics, referred to the output of the sense resistors. Dividing NTF_{en} (eq. (3-9)), which gives the output referred thermal noise, by the STF (eq. (3-8)), we can get the transfer function of the thermal noise referred to the input of the modulator and is given in eq. (4-2).

$$NTF_{en,in} = \frac{1}{H_{th}(s)H_e(s)} \tag{4-2}$$

where $H_{th}(s)$ is the transfer function of the thermal filter developed in section 3.2.2., and $H_e(s)$ is the temperature sensor's sensitivity (=3200 ppm/K). Eq. (4-2) is plotted in Fig. 4-2, where the dashed line highlights the upper limit of the BW of interest. Integrating the noise in the BW of interest, we find that a thermal noise of ~19 nV/√Hz results in a resolution of 13 bits.

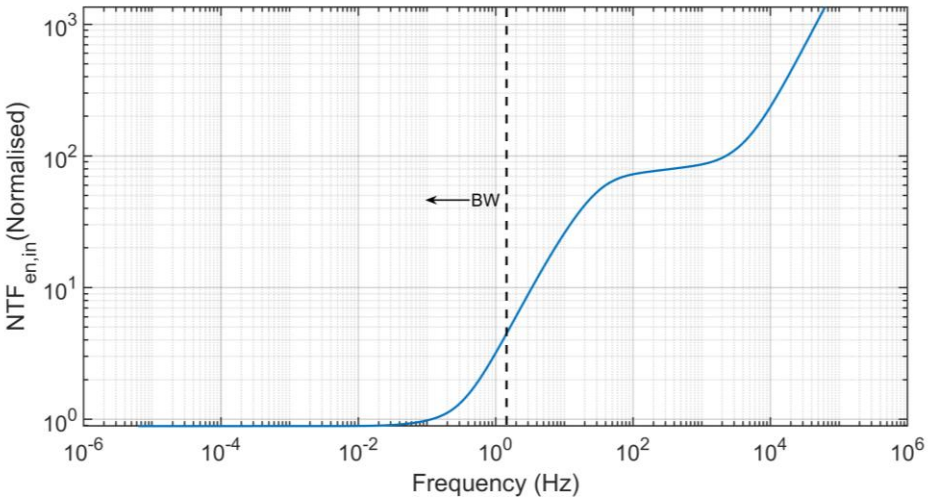

Fig. 4-2: Normalised transfer function of thermal noise referred to the input of TΣΔM

Finally, as discussed above, the sensor must maintain a constant overheat of 35˚C above ambient temperature irrespective of flow, thereby needing to be operated in CTD-TB mode. The requirements for the read-out and the TΣΔM are listed in Table 4-1. It is not an exhaustive list of requirements needed to build a commercial product, but it only highlights the ones that were main focus areas for this thesis.

Table 4-1: Read-Out Specifications

Specification	Value
Resolution	>13 bits
Bandwidth	>1.5Hz
Input referred thermal noise density	<19 nV/√Hz
Overheat	35˚C
Full-Scale Flow	7mL/min (by senor design)

4.2. Realization of TΣΔM for CTD-TB flow sensing

This section explores the final architectural realization of the modulator built around the calorimetric flow sensor. The initial starting point is shown in Fig. 3-16, in which the sensor is biased by current sources and is operated in the CP-TB mode. However, designing low-noise BJT/MOS-based current sources for the target application is challenging. This is because the BW of interest is ~1.5Hz, and such current sources typically have significant 1/*f* noise. Thus, they would require chopping or other circuit techniques to bring their 1/*f* noise below the thermal noise floor with a corner frequency substantially lower than 1.5Hz. These drawbacks were encountered during the design of a proof-of-concept prototype built based on such current sources. However, the prototype successfully confirmed the second-order modulator's stability.

A more efficient way to bias the sensor is to put it in a Wheatstone Bridge (WhB), as shown in Fig. 4-3. In addition, a method of regulating the sensor's common-mode temperature is required to operate it in the CTD-TB mode. This is done by implementing a pseudo-differential architecture in which two independent loops are used to regulate the absolute temperature of the two resistors to 35˚C above the ambient temperature. Flow information will then be encoded in the difference in bit-streams of the two single-ended modulators.

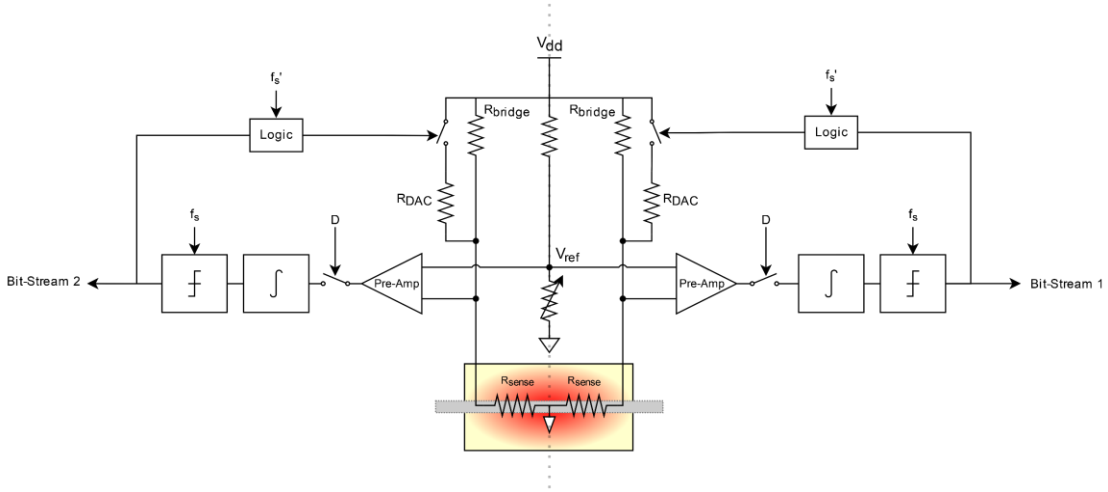

Fig. 4-3: Pseudo-differential architecture of TΣΔM for CTD-TB flow sensing

The bridge resistors (R_{bridge}) set the biasing current, while the DAC resistors (R_{DAC}) set the feedback current (note that $R_{DAC} < R_{bridge}$). The common-mode level is currently set by a resistive divider with a tuneable resistor to adjust the reference voltage, V_{ref}. Note that the architecture in Fig. 4-3 is pseudo-differential about the dashed line, which means that errors common to both modulators, such as supply noise, will be cancelled out in the final differential output (Bit-Stream 1 - Bit-Stream 2). However, the inevitable mismatch between the two paths will limit this cancellation, resulting in some noise leakage to the output. As a result, a low-noise voltage reference is needed to bias the WhB. This

architecture is also subject to tolerances in sensor manufacturing as the bias current and the DAC current are now governed by the impedance of the sense resistors summed with R_{bias} and R_{DAC} (the impedance seen from VDD to GND), respectively. Any mismatch in the sense resistors will result in an offset at the output, which, however, can be easily removed by calibration.

The average power in each sense resistor, per cycle of TΣΔM, will be given by eq. (4-3)

$$P_{avg} = \left(\left(\frac{VDD}{R_{sense} + R_{bridge}} \right)^2 \frac{T - T_{on}}{T} + \left(\frac{VDD}{R_{sense} + R_{bridge} || R_{DAC}} \right)^2 \frac{T_{on}}{T} \, \mu_{avg,cm} \right) R_{Sense} \quad (4\text{-}3)$$

where T_{on} is the on-period of the RZ feedback DAC and $\mu_{avg,cm}$ is the Bit-Stream average of the common-mode modulator. To utilise the full-scale range of the common-mode modulator, we would like to have the $\mu_{avg,cm}$ as 0.5 under no-flow conditions. Furthermore, taking an RZ DAC with a 50% duty cycle, we can use eq. (4-3) to find the average temperature of each sense resistor by multiplying the average power with the thermal resistance, R_{th}, found in section 3.2.2. To ensure a temperature of 35˚C above ambient, we need a power of ~20mW. On this basis, the bias current ($V_{DD} / (R_{sense} + R_{Bridge})$) was chosen to be 8mA to ensure a sufficient signal content during the sense phase (Fig. 3-13), and the corresponding DAC current ($V_{DD} / (R_{sense} + R_{Bridge} || R_{DAC})$) is then 26mA to ensure an average power input of 20mW.

Now, we look into the implementation of the different blocks shown in Fig. 4-3.

Wheatstone Bridge: The values of the resistors shown in the WhB in Fig. 4-3 can be determined from the chosen current values of 8mA and 26mA for the bias current and the DAC current, respectively. For a VDD of 5V, the corresponding values of R_{bridge} and R_{DAC} will be 525Ω and 112Ω, respectively. Note that, for this calculation, the value of the sense resistor was taken to be 100Ω, which is the expected value for an overheat of 35˚C at room temperature. The WhB resistors should have a low-temperature coefficient to ensure minimal variation across temperature and were chosen accordingly. The switches were chosen to be low leakage, low on-resistance precision switches from the TMUX112x [75] family.

The noise of the WhB can be calculated by realizing that, when seen from the input of the amplifier, the sense resistors and the bridge resistors will be in parallel. Since the DAC resistors will be disconnected during the sense phase when the rest of the interface circuit is connected, they will not add to the total noise. The noise of the WhB will thus be given by eq. (4-4)

$$V_{N,WhB} = \sqrt{2} \sqrt{4kT(R_{bridge} || R_{Sense})} \quad (4\text{-}4)$$

where k is the Boltzmann constant, and T is the temperature. Note that the noise in the two arms of the WhB will be uncorrelated and have been accommodated in eq. (4-4) by multiplying it with the factor of √2. The total noise density of the WhB will thus be 1.76 nV/√Hz. Note that the noise of the reference branch will be common-mode and, hence, will be rejected by the differential modulator.

Amplifier: The amplifier topology used is the inverting amplifier shown in Fig. 4-4(a), which was chosen for its simplicity. The output of the amplifier will be given by eq. (4-5)

$$V_{out} = (V_{ref} - V_{in}) \frac{R_{fb}}{R_{in}} + V_{ref} \quad (4\text{-}5)$$

where V_{in} will be from the output node of the sensor, and V_{ref} is the voltage from the reference branch.

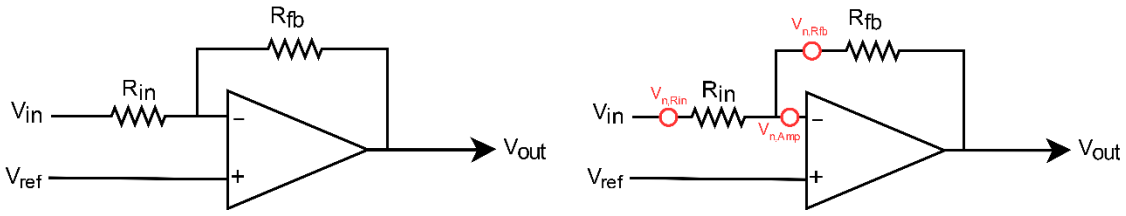

(a) Inverting Amplifier

(b) Inverting Amplifier with different noise sources highlighted

Fig. 4-4: Inverting Amplifier

The noise analysis of the inverting amplifier can be carried out by using Fig. 4-4(b), which highlights the different noise sources in the topology. The transfer function of various noise sources to the output of the amplifier is given in eq. (4-6).

$$\begin{aligned} V_{n,Rin,Out} &= \sqrt{4kTR_{in}}\frac{R_{fb}}{R_{in}} \\ V_{n,Rfb,Out} &= \sqrt{4kTR_{fb}} \\ V_{n,Amp,Out} &= \sqrt{\left(V_{n,Amp}\left(1+\frac{R_{fb}}{R_{in}}\right)\right)^2} \end{aligned} \tag{4-6}$$

where $V_{n,Rin,Out}$ is the noise from the input resistor, $V_{n,Rfb,Out}$ is the noise from the feedback resistors, and $V_{n,Amp,Out}$ is voltage noise from the OPAMP. The gain of the amplifier (A_{inv}) being R_{fb}/R_{in}, we can find the total input referred noise of the inverting amplifier by dividing the square of eq. (4-6) by a square of the amplifier gain as given in eq. (4-7).

$$V_{n,in} = \sqrt{4kTR_{in} + 4kTR_{fb}\left(\frac{R_{in}}{R_{fb}}\right)^2 + \left(V_{n,Amp}\left(1+\frac{R_{in}}{R_{fb}}\right)\right)^2} \tag{4-7}$$

Thus, the noise from the input resistors will be directly seen at the input without any attenuation, whereas the amplifier gain will attenuate the noise of the feedback resistor. The OPAMP noise will be amplified by $(1 + 1/A_{Inv})$. Eq. (4-7) tells us that the input-referred noise of the inverting amplifier can be reduced by increasing the closed loop gain, with the lower limit being formed by the noise of the OPAMP and the input resistors. A higher amplifier gain can also suppress the noise of the subsequent stages more efficiently. However, a very high gain can cause linearity issues due to headroom limitations.

The OPAMP chosen was from the MAX442x [76] series, which is a chopped and auto-zeroed OPAMP and thus has low 1/f noise. It has a high DC gain with a GBW of ~5MHz. The input resistors were chosen as 1kΩ and feedback resistors as 100kΩ to have a closed loop gain of 40dB, which ensures that we are primarily limited by the noise of the OPAMP. With the expected signal swings of 400 µV at the sensor's output, a gain of 40dB translates to an output swing of 40 mV. With a supply headroom of 5V, a swing of 40 mV will result in no issues in the amplifier's linearity. The total input referred noise of the inverting amplifier will thus be 10.8 nV/√Hz. Since two amplifiers are used, the total noise at the output of the sense resistors will be √2 times higher and equal to 15.41 nV/√Hz.

Integrator: The integrator used is an OTA RC integrator, as shown in Fig. 4-5(a), again for its simplicity. The integrator unity gain frequency will be governed by the values of the integrating resistor (R_{in}) and the feedback capacitor (C_{fb}) as given in eq. (4-8).

$$f_u = \frac{1}{2\pi R_{in} C_{fb}} \tag{4-8}$$

Though the simulations assure modulator stability, the limitations in modelling the thermal mass raise some concerns, and thus, a provision to add a feedforward capacitor (C_{ff}) to the integrator was kept. The feedforward zero will be at the frequency given by eq. (4-9). Since the design was made using discrete components, the pole/zero locations of the integrator could be changed easily on the printed circuit board (PCB).

$$f_{ff} = \frac{1}{2\pi R_{in} C_{ff}} \tag{4-9}$$

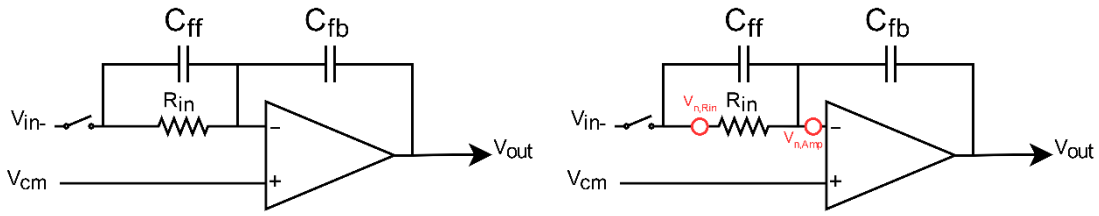

(a) OTA-RC Integrator

(b) Integrator with different noise sources highlighted

Fig. 4-5: OTA RC- Integrator

Noise analysis of the integrator is straightforward in this case, where the noise of the OPAMP and the integrating resistor is seen directly at the input, as shown in Fig. 4-5(b). To refer these noise sources to the output of the sense resistors, we need to divide by the gain of the inverting amplifier (A_{inv}), resulting in the total input referred noise of the integrator to be given by eq. (4-10).

$$V_{n,INT} = \sqrt{\frac{4kTR_{in}}{A_{inv}^2} + \frac{V_{n,AMP}^2}{A_{inv}^2}} \tag{4-10}$$

The OPAMP chosen was the same as the one used for the inverting amplifier. From simulations, the unity gain frequency was chosen to be 17.5 kHz to allow for large signal swings at the input of the quantizer. The integrating resistor was 1kΩ, and the integrating capacitor was then 9nF. The resulting noise density of the integrator, referred to the output of the sense resistors, is 0.1nV/√Hz.

The total input referred noise spectral density of the modulator is thus 15.51 nV/√Hz, thus allowing a safe margin to ensure a resolution of >13 bits in a BW of 1.5 Hz.

Integrator Gating: The integrator must be disconnected from the WhB during the drive phase (Fig. 4-6) to ensure no integration occurs when the DAC is connected. A high-impedance node is created by opening the switch shown in Fig. 4-5, and the integration is stopped, resulting in the integrator output (and the OPAMP virtual ground) to hold its previous state. A dead band is implemented (Fig. 4-6) between the time the feedback DAC is disconnected, and the integrator is connected to prevent integration errors due to switching transients.

This dead band was implemented by combining an RC-delay line with an AND gate, which delays only the rising edge of the clock, as shown in Fig. 4-7. The switch used to connect/disconnect the integrator

was again chosen from the TMUX112x family. The AND gate chosen was the SN74HC7001 [77], and the main clock is to be taken via an external function generator.

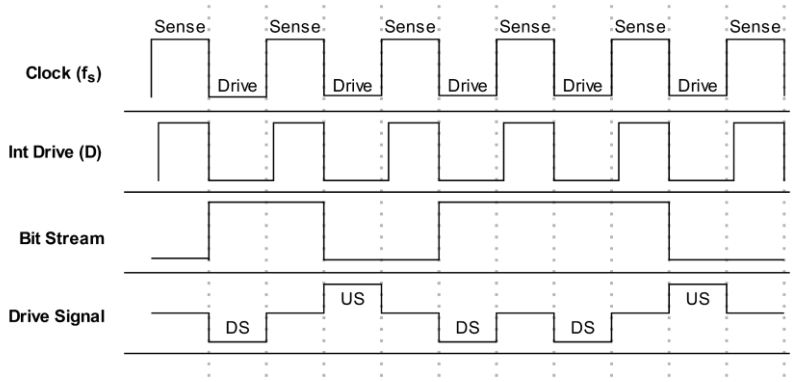

Fig. 4-6: Clock scheme for the second-order TΣΔM

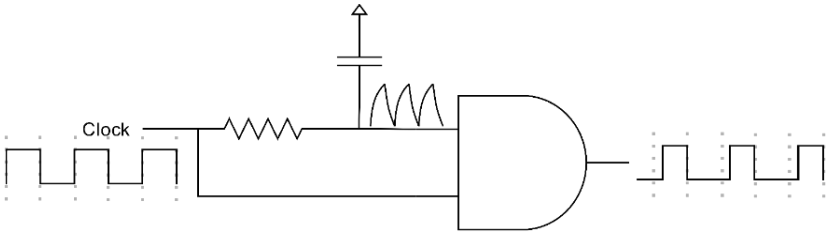

Fig. 4-7: Integrator Clock Generator

Quantizer and digital logic: The quantizer has been implemented using a continuous time comparator with a D-FF, as shown in Fig. 4-8. The requirements on the quantizer are not stringent as it needs just to be fast enough to take the decision, which is not a challenging task with a clock frequency of 5kHz.

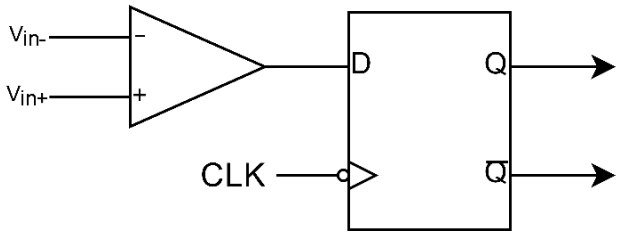

Fig. 4-8: Quantizer implementation using a Continuous-Time comparator and D-Flip Flop

The digital logic shown in the block diagram of Fig. 4-3 is primarily needed to implement an RZ feedback system as per the clock diagram of Fig. 4-6. This is easily achievable by using a two 2-input AND gate with 1 input as the inverse of the clock and 1 input from the D-Flip Flop shown in Fig. 4-9. The comparator chosen was from the TLV902x [78] family, the D-FF was chosen as SN74HCS72 [79], and the AND gate was chosen again as SN74HC7001.

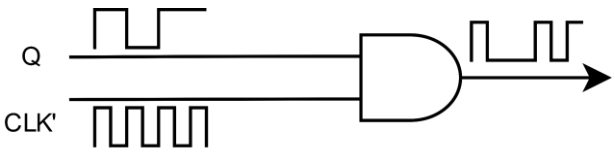

Fig. 4-9: Digital Logic to create RZ feedback DAC

4.3. Top Level Simulations

The performance of the modulator shown in Fig. 4-3 was then tested using circuit simulations. The thermal filter was modelled as explained in section 3.3.1.1. The blocks in Fig. 4-3 were replaced by their relevant circuit-level counterparts, as explained in section 4.2. The non-idealities of various elements such as OPAMP, Comparator, D-FF, and digital blocks were found using the respective datasheets and modelled using VerilogA. The simulation was performed for an f_s of 5kHz with 40dB amplifier gain and an integrator with a 17.5 kHz unity-gain frequency and no feedforward capacitor.

With no input, the simulated spectrum of the differential modulator (Bit-Stream 1 – Bit-Stream 2) is shown in Fig. 4-10. The 10dB/decade slope seen up to ~30Hz is due to the thermal noise of the interface electronics shaped by the thermal filter. The higher frequency shows a 30dB/decade slope due to the quantization noise shaped by both the thermal and electrical integrator. Shown in Fig. 4-11 is the output spectrum of the two single-ended modulators. As expected, the noise shaping properties are the same as in Fig. 4-9. However, we see high-frequency tones in the single-ended modulators, which are cancelled out in the differential modulators and were found to be a function of the CM level and the flow input.

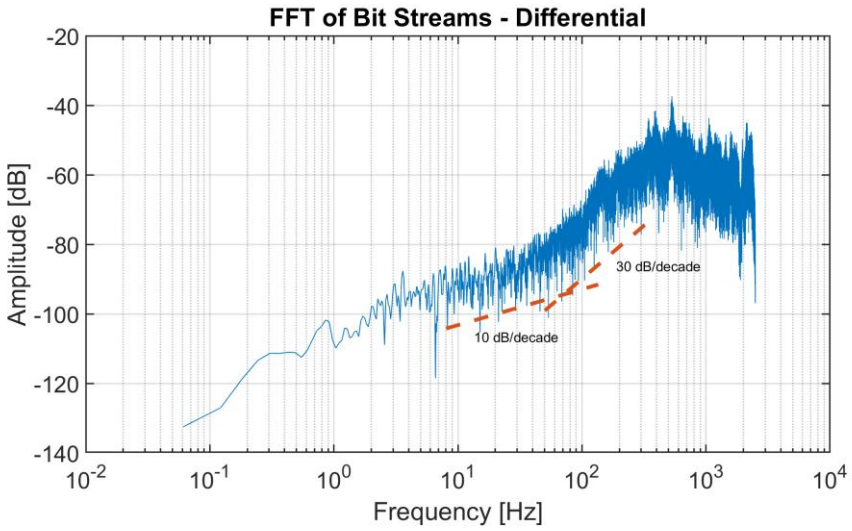

Fig. 4-10: Simulated output spectrum of the differential TΣΔM

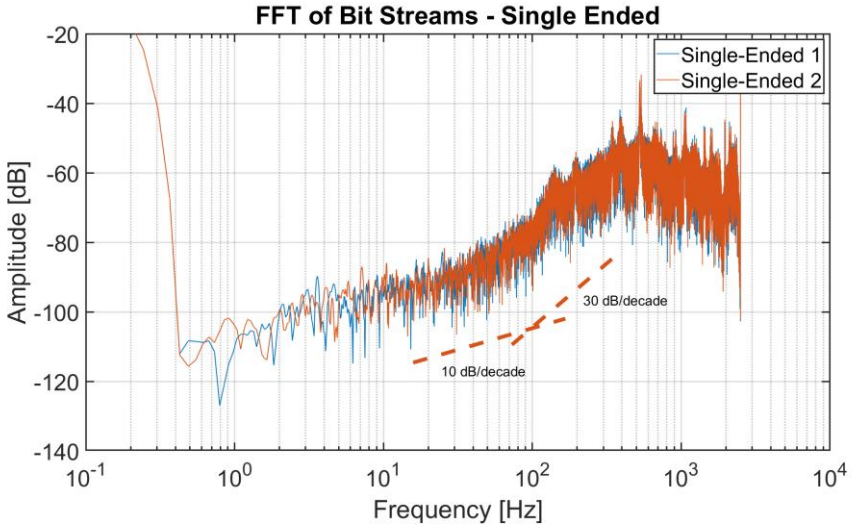

Fig. 4-11: Simulated output spectrum of the Single-Ended TΣΔMs

To validate the modulator's stability over the target input range (-3.75mW to 3.75mW), we need to check if the swing of the two integrators in the modulator, thermal and electrical, are bounded across the entire input range. Fig. 4-12(a) and Fig. 4-12(b) show the swing at the output of the thermal integrator and electrical integrator, respectively, for inputs ranging from -4mW to 4mW. We can see that the signal swings remain bounded across the entire range, showing that the modulator is stable. Moreover, from Fig. 4-12(a), we see that the temperature swing of the sensor is <170mK, thereby showing that the TΣΔM operates the sensor in a TB mode.

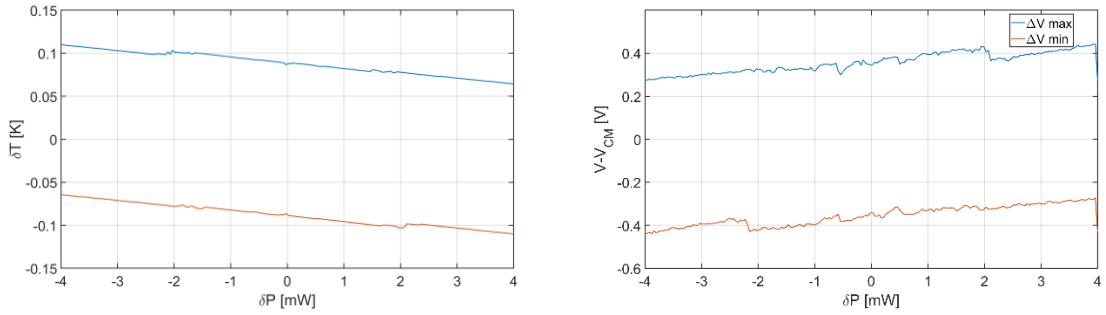

(a) Thermal Integrator Swings *(a) Electrical Integrator Swings*

Fig. 4-12: Signal Swings at the output of thermal and electrical integrator

To confirm that the designed modulator achieves the target resolution in the given BW, a 300-second long simulation was performed with an input of 3.75 mW and 0 mW. To decimate the data, simple sinc filters were used. A $sinc^1$ filter, which is usually sufficient to suppress the out-of-band (OOB) quantization noise of first-order ΣΔM, does not work well with the designed TΣΔM because the OOB slope is greater than 20dB/decade. A $sinc^2$ filter works well with the designed modulator, as it sufficiently suppresses the OOB quantization noise. A slightly improved resolution was obtained with a $sinc^3$ filter at the cost of increased filter complexity. This is primarily due to the slight peaking of the NTF at frequencies close to 300Hz. However, the $sinc^2$ filter was used for ease of implementation. The modulator's input-referred noise was found by calculating the standard deviation of the Bit-Stream average with zero input. Its dynamic range can be found by subtracting the modulator's output for a full-scale input from no input. A plot of BW vs resolution can then be created, as shown in Fig. 4-13. Also shown in Fig. 4-13 is our design target. A resolution of ~13.8 bits can be achieved in a BW of 1.5 Hz, meeting our specs with a sufficient margin.

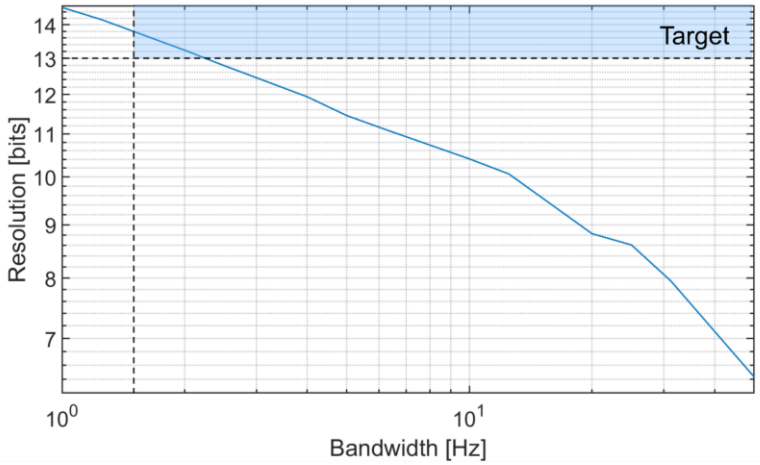

Fig. 4-13: Simulated plot of BW vs resolution for the TΣΔM

4.4. Measurement Results

The prototype PCB is shown in Fig. 4-14. It was designed conservatively, with many test points and trimming options, and is 130cm^2 in size. The area marked "Analog" includes the amplifier and the integrator. The “Digital” part comprises the comparator, the D-Flip Flop, and the AND gate. The “Clock” consists of an SMA connector for the input master clock taken from an external function generator and the circuit needed to generate the gating pulse for the integrator. The data is read out via the NI-PCI 6363 DAQ board. The connection to the DAQ board is galvanically isolated with digital isolator ICs. The bit-streams of the two single-ended modulators are read by the DAQ board, and data is post-processed in LabVIEW to get the differential bit-stream. The sensor is connected to the PCB via a three-pin connector housing shown in Fig. 4-14. The reference branch was implemented using potentiometers to tune the reference voltage, which changes the common-mode temperature. The other potentiometers were used for tuning the RC delay line. The board is powered using a 5V supply from low-noise LDOs.

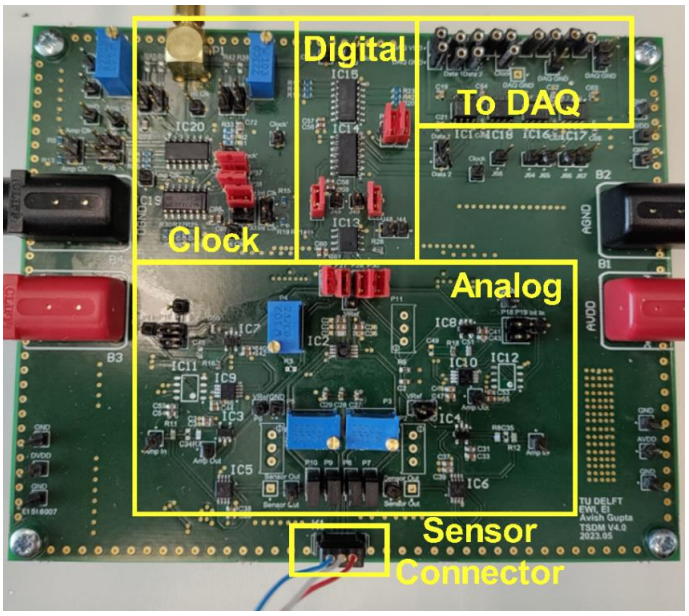

Fig. 4-14: The prototype PCB for the TΣΔM

The test setup for flow measurements is depicted in the block diagram of Fig. 4-15. Pressurized air is used as the fluid to test the modulator. An analog valve is used to set the air pressure to 2 bar, followed by EL Flow Prestige® [57] to control the fluid flow through the sensor.

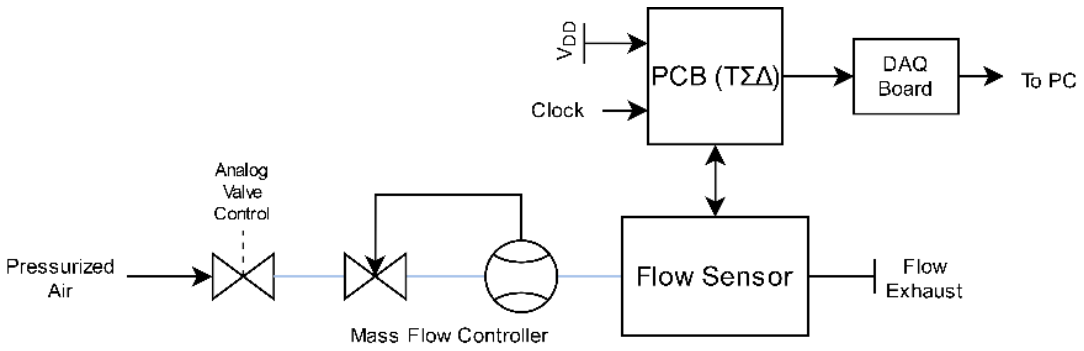

Fig. 4-15: Test Setup for Flow Measurements

The differential output spectrum of the second-order TΣΔM under no flow conditions is shown in Fig. 4-16. The gentle 10dB/decade slope observed up to ~50Hz is due to the thermal noise of the interface

electronics, followed by the 30 dB/decade slope, which is the quantization noise-dominated region. Fig. 4-16 also shows the output spectrum when the integrator is bypassed, resulting in a first-order TΣΔM. The first-order modulator has a noise floor much higher than the thermal noise floor of the second-order TΣΔM as it is quantization noise-dominated. Adding a second integrator, thus, helps reduce the quantization noise below the thermal noise floor and gains more than 10dB in resolution.

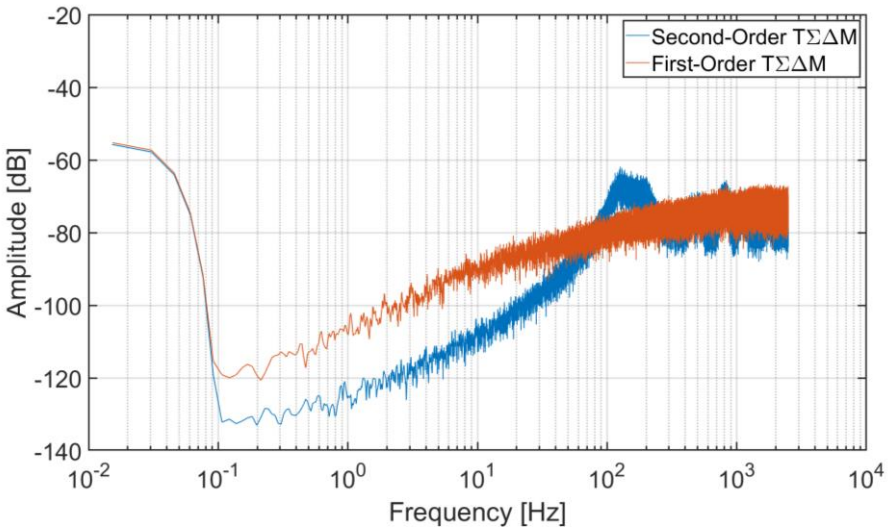

Fig. 4-16: Output Spectrum of the differential First-Order and Second-Order TΣΔM at 0 flow

Fig. 4-17 shows the output spectrum of the bit-streams of the two single-ended second-order TΣΔMs. The two spectrums show nearly identical performance and have noise-shaping characteristics similar to the differential bit-stream of the second-order modulator shown in Fig. 4-16. However, the single-ended modulators show tones at frequencies above 300Hz, which are nearly cancelled out when the difference is taken. The frequencies and amplitudes of these tones are a function of the sensor's CM level and the input flow rate.

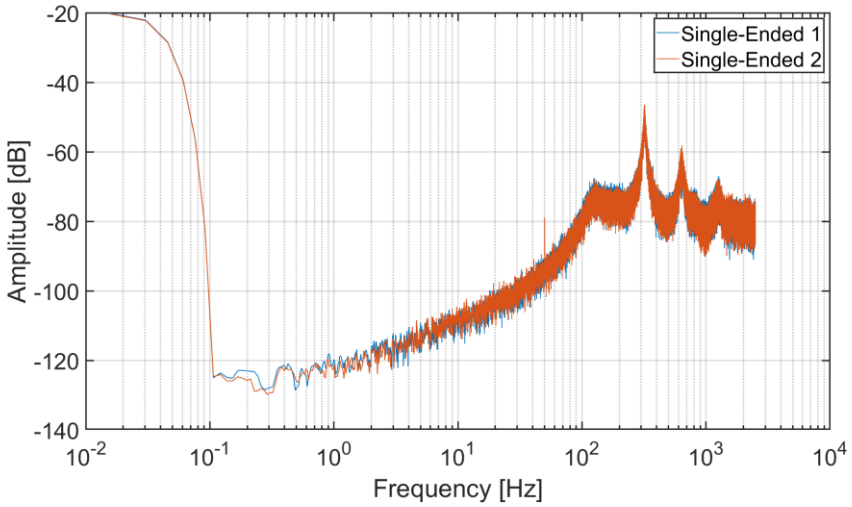

Fig. 4-17: Output spectrum of single-ended Second-Order TΣΔM

Fig. 4-18 shows the output spectrum of the bit-streams of the single-ended first-order TΣΔM. We also see tones in the output spectrum of the first-order modulator, which are a function of the sensor's CM temperature and flow input.

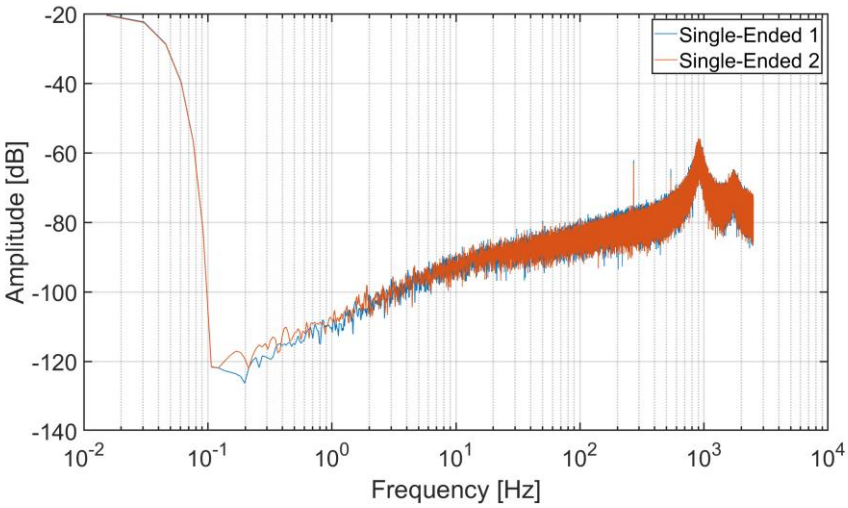

Fig. 4-18: Output spectrum of single-ended First-Order TΣΔM

The modulator's DC transfer function was tested by sweeping the input flow range. Fig. 4-19 shows the input-output transfer curve for the TΣΔM. From section 2.2.1.2., for a sensor operated in CTD-TB mode, the output is given by eq. (4-11).

$$\mu_{AVG} = \frac{\delta P}{P_{Ref}} = \frac{SU^n \Delta T}{P_{Ref}} \tag{4-11}$$

where S and n are sensor constants. Fig. 4-19 shows the curve obtained by fitting eq. (4-11) to measurement results. The highly linear behaviour of the modulator is due to the fact that we are using only a fraction of the full-scale range of the sensor, where the response is more linear (Fig. 2-10(b)), or in other words, the sensor is operated in the low flow linear region of operation.

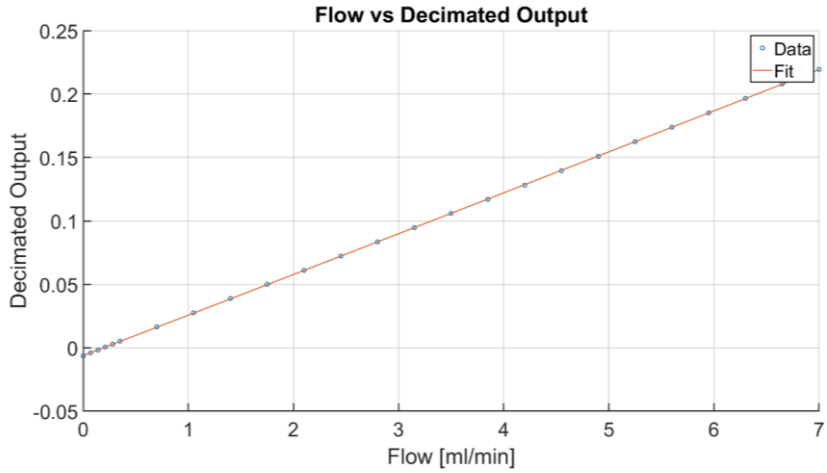

Fig. 4-19: Flow vs decimated output for the TΣΔM

To check the resolution of the designed TΣΔM, an 840-second long dataset is collected at 0 flow and decimated with a sinc^2 filter to find the noise. The dynamic range is found by subtracting the bit-stream average at 0 flow from the bit-stream average at a full-scale flow of 7mL/min. The resulting plot of BW vs resolution (in bits) is shown in Fig. 4-20, where the resolution at the target BW of 1.5Hz is 13.7 bits, thereby meeting our target resolution. The resolution is the same as predicted by the simulation results shown in Fig. 4-13, thereby validating the design procedure.

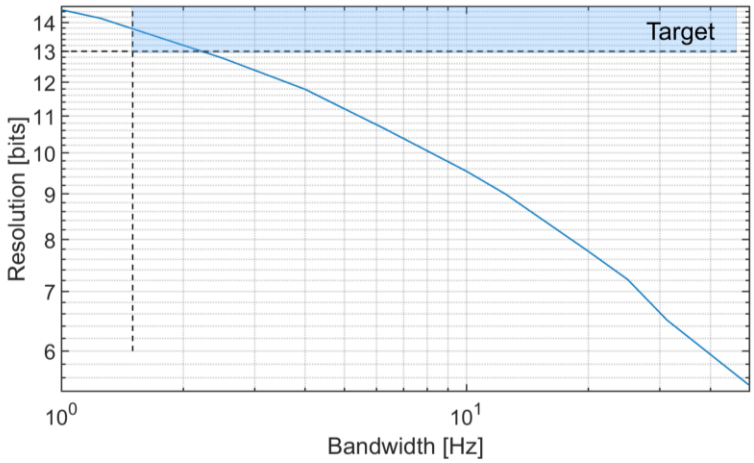

Fig. 4-20: Plot of BW vs Resolution for the TΣΔM

The sampling frequency of the second-order TΣΔM was increased to observe the modulator's stability. The test was carried out without any feed-forward capacitor. With no flow, the output spectrum of the second-order TΣΔM with different sampling frequencies is shown in Fig. 4-21. It can be seen that the modulator is stable for sampling frequencies up to nearly 20 kHz, beyond which the modulator starts showing signs of instability. The second-order modulator was also stable with a full-scale flow input for sampling frequencies up to 20 kHz.

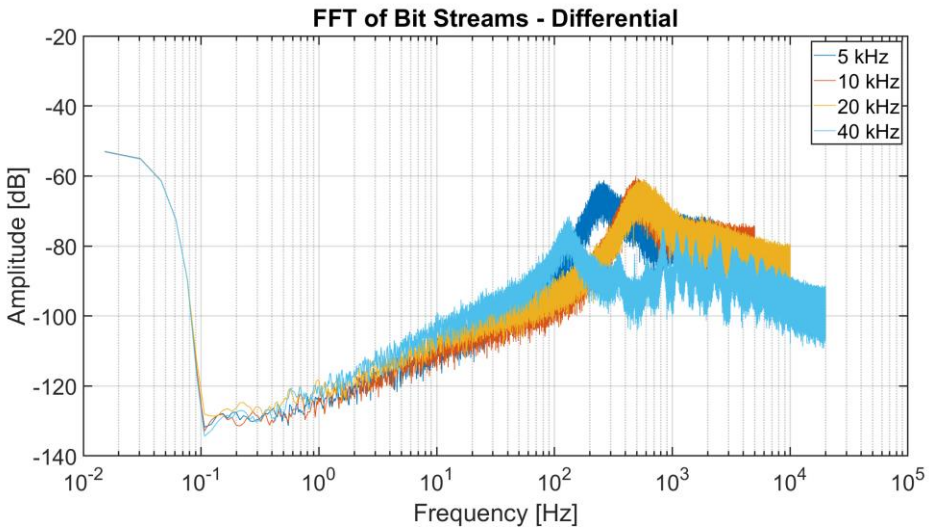

Fig. 4-21: Output Spetrums of Second-Order TΣΔM for different f_s

As shown in Fig. 4-16, the first-order modulator is quantization noise-dominated in the BW of interest and, thus, has a noise floor much higher than the second-order modulator's thermal noise-dominated noise floor. The resulting system had a modest resolution of only 11 bits. Shown in Fig. 4-22 is the effect of doubling sampling frequency on the resolution of the first-order TΣΔM. As expected of a quantization noise-dominated ADC, the resolution increases with f_s. However, the resolution only increases by ~0.6 bits per doubling of the sampling frequency instead of by 1.5 bits as in a general first-order ΣΔM. This is primarily attributed to the poor noise-shaping characteristics of the thermal filter, which gives a slope of less than 20 dB/decade and an unexpected phase shift in the modulator's transfer function [31], which is not captured in the thermal filter model developed in section 3.2.2. Moreover, this trend does not continue for frequencies above 20kHz, where the resolution starts saturating, and the modulator loses the noise shaping at frequencies above 40kHz when the thermal mass becomes too slow to

respond to the heat pulses of the feedback DAC and the system no longer behaves like a TΣΔM. The same can be observed from the output spectra of the first-order modulator for different sampling frequencies shown in Fig. 4-13, where the noise suppression starts saturating at frequencies above 20kHz. However, we can see that the modulator is still stable for sampling frequencies up to 40kHz because the phase shift of a first-order TΔΣM only tends to 90˚even at high sampling frequencies.

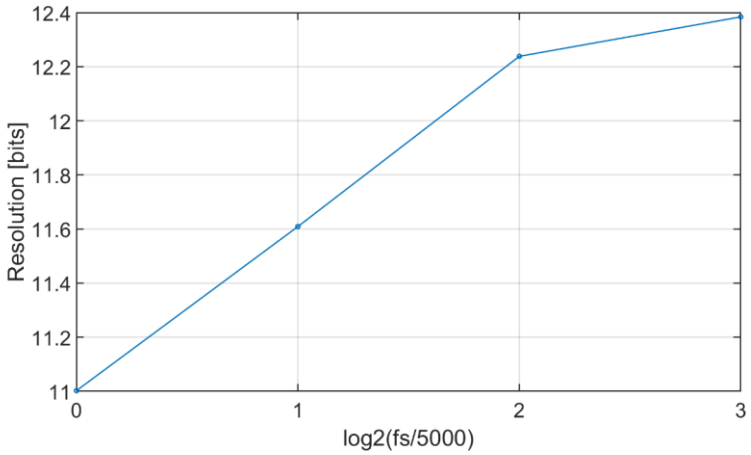

Fig. 4-22: Plot of sampling frequency ($log_2(fs/5000)$) vs resolution (bits) for the First-Order TΣΔM

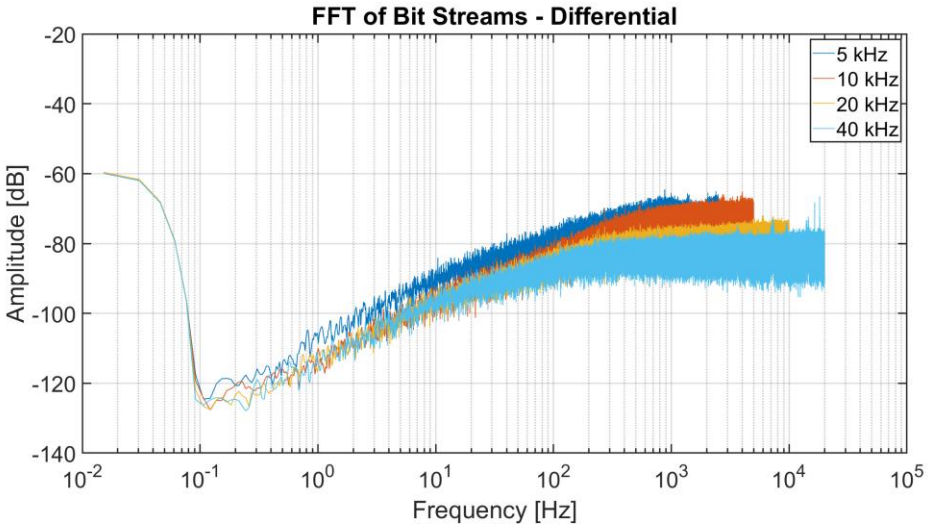

Fig. 4-23: Output Spectrums of First-Order TΣΔM for different f_s

The results indicate that the thermal filter model developed in section 3.2.2. captures the low-frequency behaviour well, thereby allowing a reasonable estimate of the modulator's resolution, but the high-frequency behaviour is not modelled well enough and merits further research.

A simple interface to read out the calorimetric flow sensor can thus be realized with a pseudo-differential TΣΔM architecture, as is shown in Fig. 4-3. The discrete-component implementation provided the freedom to rapidly explore further design optimizations. For example, since the amplifier only boosts the voltage applied to the integrator, it can be removed to simplify the design. To restore the signal swing at the input of the quantizer, the integrating capacitor size was reduced by a factor of 100 (the amplifier had a gain of 100V/V). Moreover, the continuous-time (CT) comparator in the quantizer (Fig. 4-8) can be removed if the swing at the quantizer input is sufficient. However, tests showed that the hysteresis of the D-FF results in a slight loss of resolution. The output spectrum in this case is shown in Fig. 4-24, where we can see that the modulator's OOB performance degrades, resulting

in a ~1dB loss of resolution when the data is decimated using a sinc^2 filter. A chain of inverters can be potentially used in place of the comparator to restore the quantizer gain (and overcome the D-FF hysteresis) in a more cost-efficient manner.

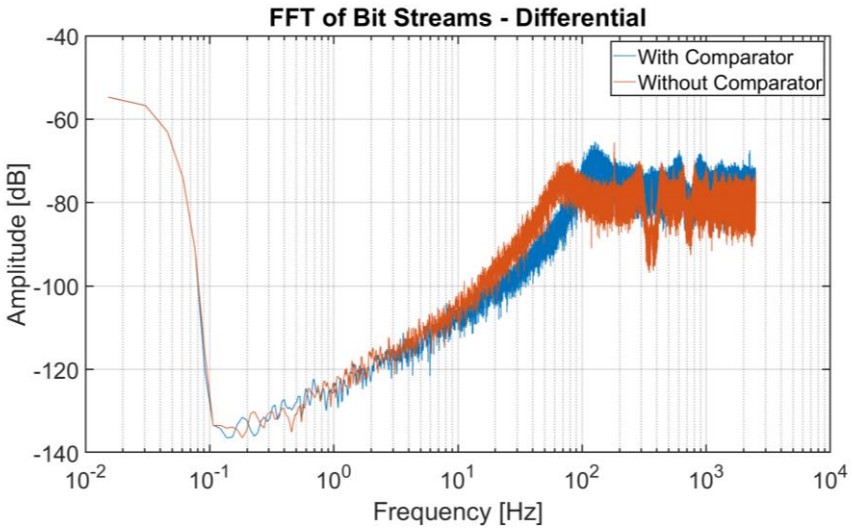

Fig. 4-24: Output spectrum of second-order TΣΔM with and without the CT comparator

The final simplified architecture shown in Fig. 4-25 was then achieved in which the amplifier was removed, but the quantizer topology was kept the same. An OPAMP still dominates the total input referred noise, and thus, a resolution of ~13.7 bits in a BW of 1.5Hz was maintained while reducing the number of components significantly.

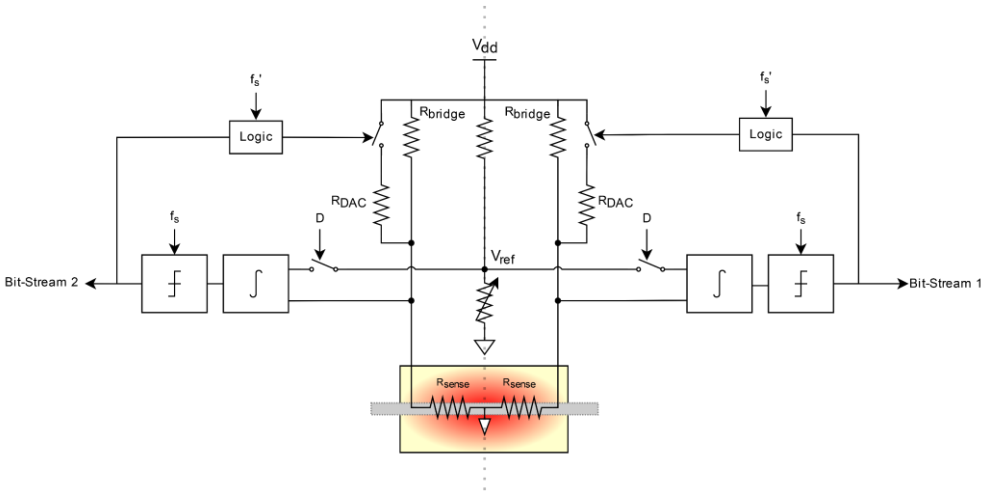

Fig. 4-25: Final optimized architecture of TΣΔM for CTD-TB flow sensing

4.5. Conclusion

This chapter demonstrated the design of a simple and cost-efficient read-out to interface a flow sensor in a CTD-TB mode. This is achieved by using a pseudo-differential architecture, where two independent TΣΔMs control the common-mode temperature of the sensor while also cancelling out the flow-induced temperature gradients. A prototype design using discrete components was presented to validate the design approach. With a clock frequency of 5kHz, the prototype design achieves a resolution of 13.7 bits in a BW of 1.5Hz when decimated using a sinc^2 filter. The design was optimized to reduce the number of components, resulting in the entire readout needing just two integrators, two clocked comparators, and a few switches in addition to the flow sensor.

Chapter 5. Conclusion and Future Work

5.1. Conclusion

This thesis explored the design of an interface to digitize the output of a calorimetric sensor that uses PTC resistors as heating and sensing elements. One of the primary design goals was to achieve a low-cost interface that uses minimal components while maximizing performance. This goal was achieved by using a TΣΔM-based architecture, which uses the PTC resistors in a time-multiplexed manner as heating and sensing elements. A pseudo-differential architecture was used, which controlled the common-mode as well as the differential temperature of the sensor, thereby operating it in the constant temperature difference-temperature balance mode.

The prototype pseudo-differential TΣΔM was built using discrete components on a PCB. An electrical filter was added after the thermal filter to realize a second-order modulator with improved resolution. The final architecture provides a microprocessor-compatible output while using only two integrators, two comparators, and a few switches in addition to the flow sensor. With a sampling frequency of 5kHz, the modulator achieved a resolution of ~13.7 bits in a BW of 1.5Hz when the output was decimated by a $sinc^2$ filter. The resolution was predicted well by simulations in which the thermal mass was modelled using resistors and capacitors, thereby validating the design procedure.

Measurements were also performed on a pseudo-differential first-order TΣΔM, which only uses the sensor's thermal mass as its loop filter. This achieved a modest resolution of ~11 bits at a sampling frequency of 5kHz. However, its resolution only increased at a rate of ~0.6 bits per doubling of OSR for sampling frequencies up to about 40kHz. Simulations did not predict this trend, primarily due to limitations in the modelling of the sensor's thermal mass.

5.2. Future Work

In this thesis, a TΣΔM was used to read out a calorimetric flow sensor in a CTD-TB mode. However, it can also be used to interface an anemometric sensor with minimal changes. The pseudo-differential architecture allows for ease of implementation when using discrete components but is less robust to common-mode and power supply variations. Flow sensors are also susceptible to ambient temperature changes, as their heat transfer rate depends on the temperature difference between the sensor's body and ambient temperature [28]. Moreover, dynamic element matching could be used to reduce the offset caused by the component mismatch. Finally, limitations in the modelling of the sensor's thermal mass, especially at high frequencies, raise some concerns about the modulator's stability. This section will address all these issues and describe some topics for future research.

5.2.1. Interfacing Other Thermal Flow Sensors

The pseudo-differential architecture is quite suitable for interfacing the anemometric sensor shown in Fig. 2-1. This is possible by using one of the TΣΔM shown in Fig. 4-25. The reference branch output will now be from the ambient temperature sense resistor, and the feedback will be applied to the heated resistor in a time-multiplexed manner (Fig. 5-1). The thermal noise referred to the output of the sense resistors for the anemometric sensor will be smaller due to the presence of a single integrator in the read-out chain. However, the final resolution for the same will be governed by the gain of the thermal mass and, thus, the sensor's construction. Also, the sensor will be slower due to the much larger fluid volume that needs to be heated.

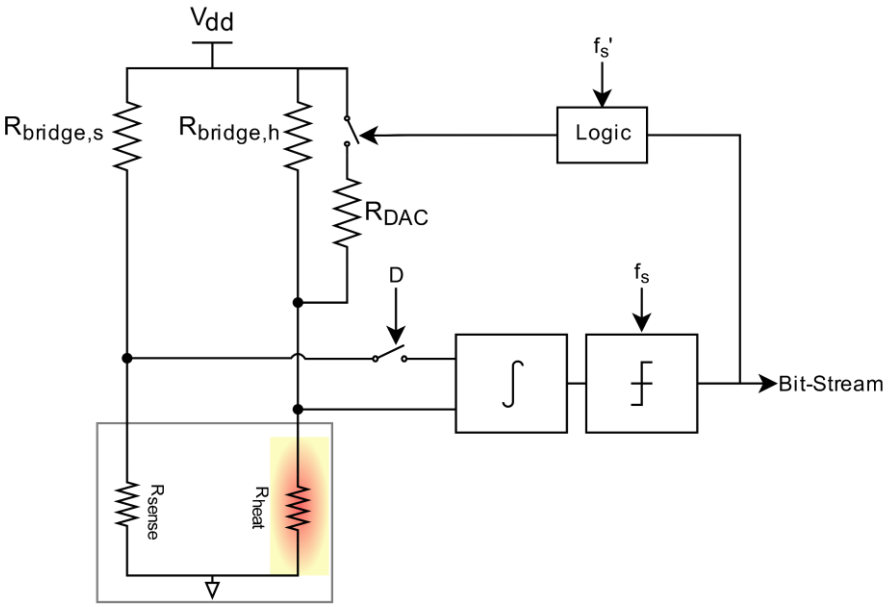

Fig. 5-1: TΣΔ based interface for the anemometric flow sensor

The pseudo-differential architecture can also be used to interface resistor-based MEMS calorimetric flow sensors. Its resolution and dynamic response are expected to improve as MEMS sensors can be micromachined to remove most of the thermal mass surrounding the resistors and the microfluidic channel. This smaller thermal mass results in an improved bandwidth of the thermal filter and, in turn, improved resolution. The dynamic response is expected to be better due to the very small amount of fluid that needs to be heated; moreover, most of the heat will be transferred into the fluid through the flow channel due to the improved isolation from the surroundings. A CMOS-MEMS implementation can be envisioned, leading to a compact, power- and cost-efficient flow sensor architecture with high resolution and dynamic response and a direct digital output.

5.2.2. Fully Differential Interface with Ambient Temperature Compensation

The use of pseudo-differential architecture allows for ease of implementation when using discrete components at the cost of reduced robustness to common-mode and power supply variations. This is primarily due to the paucity of fully differential OPAMPs with the desired specifications. However, an on-chip implementation allows us to design a fully differential OPAMP with the desired characteristics, enabling us to use a fully differential TΣΔM, which will be more robust to common-mode and power supply variations.

The differential TΣΔM is shown in Fig. 5-2. However, this architecture will operate the sensor in a CP-TB mode, driving only δT to 0. For common mode regulation, two large resistors at the output of the sense resistors can be used to sense the common-mode and build an overheat regulation loop. However, by biasing the Wheatstone bridge with a resistor, R_{VDD}, as shown in Fig. 5-2, the two bridge resistors (R_{bridge}) can now be used as common-mode sense resistors. An ambient temperature sensor can be used as the reference input of the common-mode modulator to compensate for ambient temperature variations instead of a constant reference voltage. An offset can be introduced to the ambient temperature sensor's output to maintain the temperature of the sensor body to a well-known value above ambient temperature ($T_{AMB}+\Delta T$). The output from the top of the bridge and an ambient temperature sensor's output can now be used as input to the common-mode modulator.

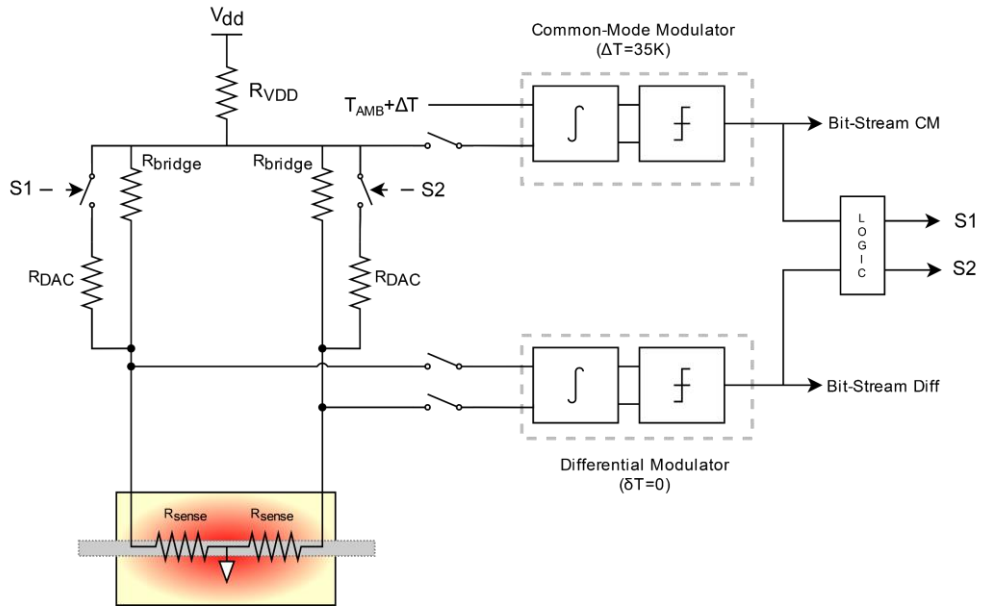

Fig. 5-2: A fully differential architecture for CTD-TB mode of operation

However, now the question arises of how to combine the outputs of the common-mode and the differential modulator to operate the sensor in CTD-TB mode. This can be achieved by dividing the drive phase into a common-mode drive and a differential drive phase. The timing diagram is shown in Fig. 5-3, where one DAC resistor is connected during the differential drive phase depending on the differential modulator output. During the common-mode drive phase, both the DAC resistors are connected or disconnected depending upon the common-mode modulator output, thereby controlling the absolute temperature of the sensor. However, this improved robustness to common-mode and supply variations comes at the cost of increased design complexity and additional digital circuitry.

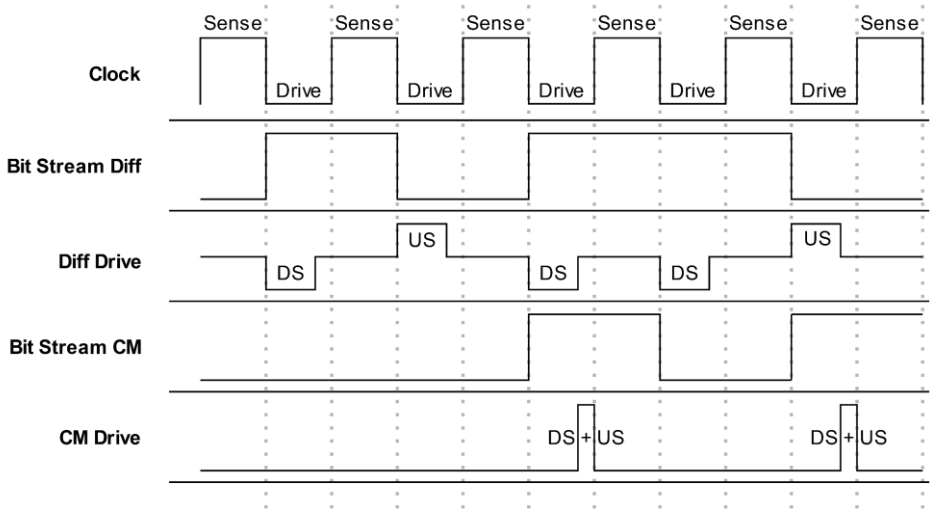

Fig. 5-3: Timing diagram for CM and Differential modulator

5.2.3. Methods to reduce the effect of mismatch

A mismatch between the resistors will lead to an offset at the output. In this work, expensive high-precision resistors with 0.01% matching were used for R_{DAC} and R_{bridge}. Dynamic Element Matching (DEM) [80] can be used to suppress the effect of mismatch of the bridge resistors, allowing us to use low-cost, low-precision resistors(Fig. 5-4). Note that R_{DAC} and R_{bridge} have different values; hence, a single-unit resistor value will need to be chosen, using which R_{DAC} and the R_{bridge} can be realized so that

a DEM scheme can be applied. Moreover, a system-level chopping can be further incorporated to reduce the effect of mismatch of the sense resistors. To achieve the system level chopping, shown in Fig. 5-4, the TΣΔM can be operated in an incremental mode where the integrators are reset after every conversion cycle of the modulator. By averaging two conversions with inverted polarity in the digital domain, the accuracy of the readout can be improved significantly. However, as can be seen in Fig. 5-4, this comes at the cost of increased circuit complexity.

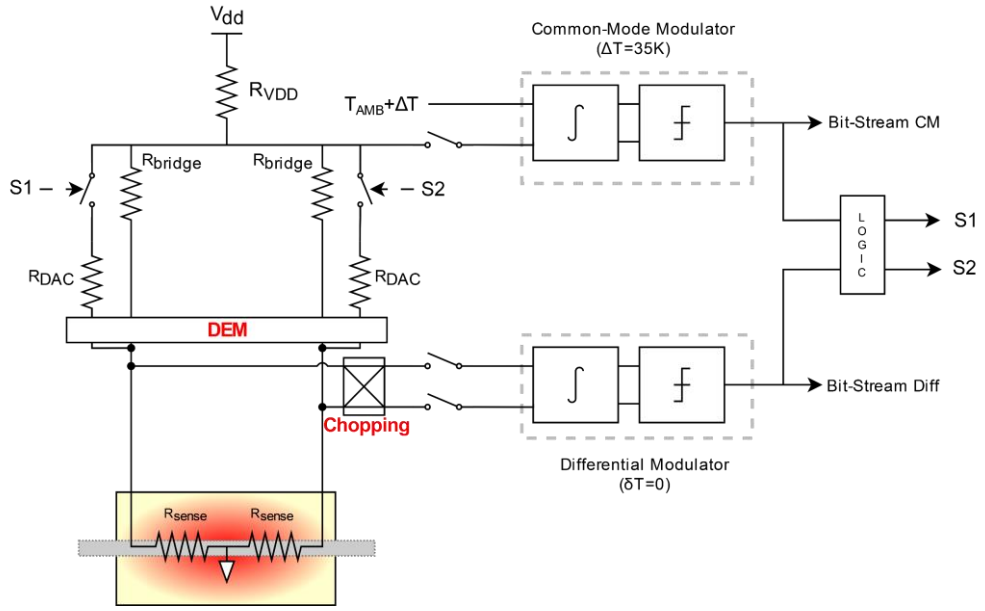

Fig. 5-4: Chopping and DEM to improve accuracy

5.2.4. Improved thermal mass modelling

The accurate modelling of thermal mass has been a challenging task. Though the predicted low-frequency behaviour matches the measurement results well, allowing for a reasonable estimate of the resolution, the limitation in high-frequency modelling limits the modulator operation to frequencies below 20kHz. Several approaches to modelling the thermal mass exist, a review of which is given in [81] and [82]. Previously, the deconvolution-based approach [68] to model the thermal mass from transient measurements was adopted in [10] and [31] and proved to be very successful in accurately predicting the performance of the TΣΔM. This approach, however, significantly adds to the modelling complexity and is highly susceptible to noise in the step measurement. A review of these methodologies, leading to a more accurate thermal mass model, could be helpful in further optimizing the design and achieving higher resolutions.

Bibliography

[1] Bolin Yu, Zhiyin Gan, Shu Cao, Jingping Xu, and Sheng Liu, "A micro channel integrated gas flow sensor for high sensitivity," *2008 11th Intersociety Conference on Thermal and Thermomechanical Phenomena in Electronic Systems*, 2008. doi:10.1109/itherm.2008.4544273

[2] P. Murali, A. M. Niknejad, and B. E. Boser, "CMOS microflow cytometer for magnetic label detection and classification," *IEEE Journal of Solid-State Circuits*, vol. 52, no. 2, pp. 543–555, 2017. doi:10.1109/jssc.2016.2621036

[3] K. A. A. Makinwa and J. H. Huijsing, "A wind sensor with an integrated low-offset instrumentation amplifier," *ICECS 2001. 8th IEEE International Conference on Electronics, Circuits and Systems (Cat. No.01EX483)*. doi:10.1109/icecs.2001.957500

[4] A. Mangell, "Flow measurement techniques," *World Pumps*, vol. 2008, no. 507, pp. 32–34, 2008. doi:10.1016/s0262-1762(08)70379-1

[5] J. E. Hardy, J. O. Hylton, T. E. McKnight, C. J. Remenyik, and F. R. Ruppel, *Flow Measurement Methods and Applications*. John Wiley & Sons, 1999.

[6] A. C. de Oliveira, S. Pan, R. J. Wiegerink, and K. A. Makinwa, "A MEMS coriolis-based mass-flow-to-digital converter for low flow rate sensing," *IEEE Journal of Solid-State Circuits*, vol. 57, no. 12, pp. 3681–3692, 2022. doi:10.1109/jssc.2022.3210003

[7] E. Aydin and K. A. A. Makinwa, "A low-field portable nuclear magnetic resonance (NMR) microfluidic flowmeter," *2021 21st International Conference on Solid-State Sensors, Actuators and Microsystems (Transducers)*, 2021. doi:10.1109/transducers50396.2021.9495479

[8] W. Xu *et al.*, "CMOS MEMS thermal flow sensor with enhanced sensitivity for heating, ventilation, and air conditioning application," *IEEE Transactions on Industrial Electronics*, vol. 68, no. 5, pp. 4468–4476, 2021. doi:10.1109/tie.2020.2984446

[9] J. T. Kuo, L. Yu, and E. Meng, "Micromachined Thermal Flow Sensors—a review," *Micromachines*, vol. 3, no. 3, pp. 550–573, 2012. doi:10.3390/mi3030550

[10] K. A. A. Makinwa, "Flow sensing with thermal sigma-delta modulators," Ph.D. dissertation, Delft Univ., 2004.

[11] Y.-H. Wang *et al.*, "MEMS-based gas flow sensors," *Microfluidics and Nanofluidics*, vol. 6, no. 3, pp. 333–346, 2009. doi:10.1007/s10404-008-0383-4

[12] P. Salomon, *Micro sensors–World wide markets and economic impact*, Jan. 2006.

[13] L. V. King, "On the convection of heat from small cylinders in a stream of fluid: Determination of the convection constants of small platinum wires, with applications to hot-wire anemometry," *Proceedings of the Royal Society of London. Series A, Containing Papers of a Mathematical and Physical Character*, vol. 90, no. 622, pp. 563–570, 1914. doi:10.1098/rspa.1914.0089

[14] J. Lötters, "ECONOMICAL THERMAL MASS FLOW SENSOR BASED ON CONSTANT TEMPERATURE ANEMOMETRY," presented at Sensor 99, Nürnberg, Germany, May 18-20, 1999

[15] T. S. J. Lammerink, N. R. Tas, M. Elwenspoek, and J. H. J. Fluitman, "Micro-liquid Flow Sensor," *Sensors and Actuators A: Physical*, vol. 37–38, pp. 45–50, 1993. doi:10.1016/0924-4247(93)80010-e

[16] L. J. Bradbury and I. P. Castro, "A pulsed-wire technique for velocity measurements in highly turbulent flows," *Journal of Fluid Mechanics*, vol. 49, no. 4, pp. 657–691, 1971. doi:10.1017/s0022112071002313

[17] A. Al-Salaymeh, J. Jovanović, and F. Durst, "Bi-directional flow sensor with a wide dynamic range for medical applications," *Medical Engineering & Physics*, vol. 26, no. 8, pp. 623–637, 2004. doi:10.1016/j.medengphy.2004.06.002

[18] J. Sobczyk, “Semi-empirical approach to gas flow velocity measurement by means of the thermal time-of-flight method—further investigation,” *Energies*, vol. 15, no. 6, p. 2166, 2022. doi:10.3390/en15062166
[19] L. Huang, “Micromachined Thermal Time-of-flight flow sensors and their applications,” *Micromachines*, vol. 13, no. 10, p. 1729, 2022. doi:10.3390/mi13101729
[20] T. S. J. Lammerink, F. Dijkstra, Z. Houkes, and J. van Kuijk, “Intelligent gas-mixture flow sensor,” *Sensors and Actuators A: Physical*, vol. 47, no. 1–3, pp. 380–384, 1995. doi:10.1016/0924-4247(94)00925-8
[21] H.-E. de Bree, H. V. Jansen, T. S. Lammerink, G. J. Krijnen, and M. Elwenspoek, “Bi-directional fast flow sensor with a large dynamic range,” *Journal of Micromechanics and Microengineering*, vol. 9, no. 2, pp. 186–189, 1999. doi:10.1088/0960-1317/9/2/320
[22] M. Ashauer *et al.*, “Thermal flow sensor for liquids and gases based on combinations of two principles,” *Sensors and Actuators A: Physical*, vol. 73, no. 1–2, pp. 7–13, 1999. doi:10.1016/s0924-4247(98)00248-9
[23] G. Bedö, H. Fannasch, and R. Müller, “A silicon flow sensor for gases and liquids using AC measurements,” *Sensors and Actuators A: Physical*, vol. 85, no. 1–3, pp. 124–132, 2000. doi:10.1016/s0924-4247(00)00380-0
[24] S. Dalola *et al.*, “MEMS thermal flow sensor with Smart Electronic Interface Circuit,” *IEEE Sensors Journal*, vol. 12, no. 12, pp. 3318–3328, 2012. doi:10.1109/jsen.2012.2219619
[25] N. A. Djuzhev, D. V. Novikov, G. D. Demin, A. I. Ovodov, and V. T. Ryabov, “An experimental study on MEMS-based gas flow sensor for wide range flow measurements,” *2018 IEEE Sensors Applications Symposium (SAS)*, 2018. doi:10.1109/sas.2018.8336727
[26] W. Xu *et al.*, “A wireless dual-mode micro thermal flow sensor system with extended flow range by using CMOS-MEMS process,” *2018 IEEE Micro Electro Mechanical Systems (MEMS)*, 2018. doi:10.1109/memsys.2018.8346682
[27] V. Szekely, “On the representation of infinite-length distributed RC One-Ports,” *IEEE Transactions on Circuits and Systems*, vol. 38, no. 7, pp. 711–719, 1991. doi:10.1109/31.135743
[28] B. W. van Oudheusden, “Effect of operating conditions on the dynamic response of thermal sensors with and without analog feedback,” *Sensors and Actuators A: Physical*, vol. 58, no. 2, pp. 129–135, 1997. doi:10.1016/s0924-4247(96)01404-5
[29] K. A. A. Makinwa and J. H. Huijsing, “A 2nd order thermal sigma-delta modulator for flow sensing,” *IEEE Sensors*, 2005. doi:10.1109/icsens.2005.1597757
[30] K. A. A. Makinwa and J. H. Huijsing, “A smart wind sensor using thermal sigma-delta modulation techniques,” *Sensors and Actuators A: Physical*, vol. 97–98, pp. 15–20, 2002. doi:10.1016/s0924-4247(02)00034-1
[31] J. Wu, “A Low-Power Thermal Wind Sensor in CMOS Technology,” M.Sc. thesis, Delft Univ., 2013.
[32] X. Wang, Y.-K. Lee, and W. Xu, “A fast response and CMOS compatible micro gas flow sensor with thermal feedback,” *IEEE Sensors Letters*, vol. 4, no. 10, pp. 1–4, 2020. doi:10.1109/lsens.2020.3026974
[33] Y. Pan, F. R. Riedijk, and J. H. Huijsing, “A new class of integrated thermal oscillators with duty-cycle output for application in thermal sensors,” *Sensors and Actuators A: Physical*, vol. 22, no. 1–3, pp. 655–659, 1990. doi:10.1016/0924-4247(89)80052-4
[34] S. Pavan, R. Schreier, and G. C. Temes, *Understanding Delta-Sigma Data Converters*. Piscataway: IEEE Press, 2017.
[35] J. H. Huijsing and F. R. Riedijk, “Integrated semiconductor circuit for thermal measurements,” U.S. Patent No. 5064296, Nov. 12, 1991.
[36] H. J. Verhoeven and J. H. Huijsing, “An integrated gas flow sensor with high sensitivity, low response time and a pulse-rate output,” *Sensors and Actuators A: Physical*, vol. 41, no. 1–3, pp. 217–220, 1994. doi:10.1016/0924-4247(94)80114-2
[37] H.J. Verhoeven, “Smart thermal flow sensors,” Ph.D. dissertation, Delft Univ., 1996.

[38] L. Castaner, V. Jimenez, M. Dominguez, F. Masana, and A. Rodriguez, “Design end fabrication of a low cost water flow meter,” *Proceedings of International Solid State Sensors and Actuators Conference (Transducers ’97)*, 1997. doi:10.1109/sensor.1997.613607

[39] M. Dominguez and L. Castaner, “Bounding of thermal Σ-Δ modulators output for sensors,” *ISCAS’99. Proceedings of the 1999 IEEE International Symposium on Circuits and Systems VLSI (Cat. No.99CH36349)*. doi:10.1109/iscas.1999.780683

[40] M. Dominguez *et al.*, “Low-cost thermal Σ-Δ air flow sensor,” *IEEE Sensors Journal*, vol. 2, no. 5, pp. 453–462, 2002. doi:10.1109/jsen.2002.806308

[41] M. Domínguez *et al.*, “A hot film anemometer for the martian atmosphere,” *Planetary and Space Science*, vol. 56, no. 8, pp. 1169–1179, 2008. doi:10.1016/j.pss.2008.02.013

[42] J.K. Zelisse, F.R. Riedijk and J.H. Huijsing, "Thermal sigma-delta modulator for wind speed and direction measurement," Proc. of Eurosensors V, p. 303, Sept. 1991.

[43] K. A. A. Makinwa and J. H. Huijsing, “A wind-sensor interface using thermal Sigma Delta Modulation Techniques,” *Sensors and Actuators A: Physical*, vol. 92, no. 1–3, pp. 280–285, 2001. doi:10.1016/s0924-4247(01)00584-2

[44] K. A. A. Makinwa and J. H. Huijsing, “Constant power operation of a two-dimensional flow sensor,” *IEEE Transactions on Instrumentation and Measurement*, vol. 51, no. 4, pp. 840–844, 2002. doi:10.1109/tim.2002.803504

[45] J. Wu, Y. Chae, C. P. van Vroonhoven, and K. A. Makinwa, “A 50mW CMOS wind sensor with ±4% speed and ±2° direction error,” *2011 IEEE International Solid-State Circuits Conference*, 2011. doi:10.1109/isscc.2011.5746239

[46] J. Wu, C. van Vroonhoven, Y. Chae, and K. Makinwa, “A 25MW CMOS sensor for wind and temperature measurement,” *2011 IEEE SENSORS Proceedings*, 2011. doi:10.1109/icsens.2011.6127204

[47] C. A. Leme and H. Baltes, “Interfaces for microsensor systems,” *Analog Circuit Design*, pp. 163–181, 1994. doi:10.1007/978-1-4757-2310-6_10

[48] D. Jaeggi, C. Azeredo Leme, P. O'Leary and H. Baltes, "Improved CMOS power sensor," Proc. of Transducers '93, pp. 462-465, June 1993

[49] C. Condemine, M. Belleville, D. Barbier, G. Delhomme, and A. Dittmar, “A new sigma-delta thermal conductivity microsystem,” *1st Annual International IEEE-EMBS Special Topic Conference on Microtechnologies in Medicine and Biology. Proceedings (Cat. No.00EX451)*, 2000. doi:10.1109/mmb.2000.893768

[50] S. Perichon *et al.*, “Micro-blood flow measurement using thermal conductivity micro-needles: A new CMOS compatible manufacturing process onto porous silicon,” *1st Annual International IEEE-EMBS Special Topic Conference on Microtechnologies in Medicine and Biology. Proceedings (Cat. No.00EX451)*, 2000. doi:10.1109/mmb.2000.893767

[51] B. A. Vitorino, D. R. Belfort, S. Y. Catunda, M. Denoual, and R. C. Freire, “Second-order thermal sigma-delta applied to resistive bolometers on infrared detection,” *2016 1st International Symposium on Instrumentation Systems, Circuits and Transducers (INSCIT)*, Aug. 2016. doi:10.1109/inscit.2016.7598214

[52] B. A. Vitorino, S. Y. Catunda, D. R. Belfort, and R. C. Freire, “Autorange thermal sigma–delta converter for incident radiation measurement,” *IEEE Transactions on Instrumentation and Measurement*, vol. 68, no. 3, pp. 774–781, Mar. 2019. doi:10.1109/tim.2018.2857899

[53] G. K. Freitas, A. V. Sa, L. S. Palma, R. C. S. Freire, and A. Oliveira, “Thermal sigma-delta modulator: A temperature measurement application,” *2008 IEEE Instrumentation and Measurement Technology Conference*, 2008. doi:10.1109/imtc.2008.4547222

[54] O. Leman, F. Mailly, L. Latorre, and P. Nouet, “Noise analysis of a first-order thermal ΣΔ architecture for convective accelerometers,” *Analog Integrated Circuits and Signal Processing*, vol. 63, no. 3, pp. 415–423, 2009. doi:10.1007/s10470-009-9419-2

[55] T. S. J. Lammerink, N. R. Tas, G. J. M. Krijnen, and M. Elwenspoek, “A new class of thermal flow sensors using ΔT=0 as a control signal,” *Proceedings IEEE Thirteenth Annual*

International Conference on Micro Electro Mechanical Systems (Cat. No.00CH36308), 2000. doi:10.1109/memsys.2000.838572

[56] "SLG Liquid Flow Meter Series," SLG Liquid Flow Meter Series Ultra-High Pressure Flow Meter for LC Applications, https://sensirion.com/media/documents/69EBDF62/61658A36/Sensirion_Liquid_Flow_Meters_SLG_Datasheet_1.pdf.

[57] "EL-FLOW® Prestige," EL-FLOW® Prestige World's most versatile Mass Flow Meters / Controllers for Gases, https://www.bronkhorst.com/getmedia/630111fa-b6d9-4c40-83e5-8bd30286ba5f/EL-FLOW-Prestige-EN.pdf.

[58] "EL-FLOW ® Select," EL-FLOW ® Select Digital Thermal Mass Flow Meters and Controllers for Gases, https://www.bronkhorst.com/getmedia/98668a82-8d1c-4b7f-af8e-995be25641b3/EL-FLOW-Select_EN.pdf.

[59] "MASS-STREAM™," MASS-STREAM™ Digital Mass Flow Meters and Controllers for Gase, https://www.bronkhorst.com/getmedia/ea3f9d74-a738-49a2-8ad8-cfd07586398a/MASS-STREAM-D-6300-960067.pdf.

[60] M. Ahmed *et al.*, "Fully integrated bidirectional CMOS-MEMS flow sensor with low power pulse operation," *IEEE Sensors Journal*, vol. 19, no. 9, pp. 3415–3424, 2019. doi:10.1109/jsen.2019.2891784

[61] K. Clocker, S. Sengupta, M. Lindsay, and M. L. Johnston, "Single-element thermal flow sensor using dual-slope control scheme," *2017 IEEE SENSORS*, 2017. doi:10.1109/icsens.2017.8234069

[62] Thermal mass flow sensor for gases - inline/CTA principle, https://www.bronkhorst.com/int/service-support-1/technologies/thermal-mass-flow-sensor-for-gases-inline-cta-principle/.

[63] B. W. van Oudheusden, "Silicon Thermal Flow Sensors," *Sensors and Actuators A: Physical*, vol. 30, no. 1–2, pp. 5–26, Jan. 1992. doi:10.1016/0924-4247(92)80192-6

[64] Thermal mass flow sensor for gases - bypass principle, https://www.bronkhorst.com/int/service-support-1/technologies/thermal-mass-flow-sensor-for-gases-bypass-principle/.

[65] W. Jouwsma, "Laminar flow element," U.S. Patent No. 4427030A, Jan. 24, 1984.

[66] What is the difference between laminar flow and turbulent flow?, https://www.bronkhorst.com/int/blog-1/what-is-the-difference-between-laminar-flow-and-turbulent-flow/.

[67] P. M. J. M., *Analog-to-Digital Conversion*. Cham: Springer, 2023.

[68] V. Székely, "Thermodel: A tool for Compact Dynamic Thermal Model Generation," *Microelectronics Journal*, vol. 29, no. 4–5, pp. 257–267, 1998. doi:10.1016/s0026-2692(97)00065-7

[69] K.A.A. Makinwa and J.H. Huijsing, "A wind sensor interface using thermal sigma-delta modulation," Proc. of Eurosensors XIV, pp. 249 - 252, Sept. 2000.

[70] F. F. Kuo, *Network Analysis and Synthesis*. New York: Wiley, 1966.

[71] V. Székely and T. Van Bien, "Fine structure of heat flow path in semiconductor devices: A measurement and Identification Method," *Solid-State Electronics*, vol. 31, no. 9, pp. 1363–1368, 1988. doi:10.1016/0038-1101(88)90099-8

[72] V. Székely, "A new evaluation method of thermal transient measurement results," *Microelectronics Journal*, vol. 28, no. 3, pp. 277–292, 1997. doi:10.1016/s0026-2692(96)00031-6

[73] K. A. A. Makinwa, V. Szekely, and J. H. Huijsing, "Modeling and simulation of thermal sigma-delta modulators," *IMTC/2002. Proceedings of the 19th IEEE Instrumentation and Measurement Technology Conference (IEEE Cat. No.00CH37276)*. doi:10.1109/imtc.2002.1006850

[74] E. L. Gardner *et al.*, "MEMS thermal flow sensors— an accuracy investigation," *IEEE Sensors Journal*, vol. 19, no. 8, pp. 2991–2998, 2019. doi:10.1109/jsen.2019.2891596

[75] Texas Instruments, "5-V, Low-Leakage-Current, 1:1 (SPST), 2-Channel Precision Switches", TMUX1121 datasheet, Rev 1 - SEPTEMBER 2019
[76] Maxim Integrated , "36V, Low-Noise, Precision, Single/Quad/Dual Op Amps", MAX442x datasheet, Rev 7 - April, 2015
[77] Texas Instruments, "Quadruple 2-Input AND Gates with Schmitt-Trigger Inputs", SN74HC7001 Datasheet, Rev 6 - April, 2021
[78] Texas Instruments, "Precision Comparator Family", TLV9022 datasheet, Rev 6 - Mar, 2023
[79] Texas Instruments ,"Automotive Qualified Schmitt-Trigger Input Dual D-Type Negative-Edge-Triggered Flip-Flops With Clear and Preset", SN74HCS72-Q1 datasheet, Release - Oct, 2019
[80] I. Galton, “Why dynamic-element-matching DACS work,” *IEEE Transactions on Circuits and Systems II: Express Briefs*, vol. 57, no. 2, pp. 69–74, 2010. doi:10.1109/tcsii.2010.2042131
[81] A. Boodi, K. Beddiar, Y. Amirat, and M. Benbouzid, “Building thermal-network models: A Comparative Analysis, recommendations, and Perspectives,” *Energies*, vol. 15, no. 4, p. 1328, 2022. doi:10.3390/en15041328
[82] N. J. Ziegeler, P. W. Nolte, and S. Schweizer, “Quantitative performance comparison of thermal structure function computations,” *Energies*, vol. 14, no. 21, p. 7068, 2021. doi:10.3390/en14217068

Appendix A

MATLAB® Algorithm for thermal mass modelling.

To model the thermal mass, first, the transient response was measured using the setup shown in Fig. 3-7. A MATLAB algorithm then extracts the values of the thermal resistances (R_{th}) and capacitances (C_{th}). These values of R_{th} and C_{th} directly correspond to the elements of the foster network shown in Fig. 3-5 (a), allowing us to create a model of the thermal mass in circuit simulators such as Cadence or LTSpice (Fig. 3-11).

The primary goal of the algorithm is to find the foster network that shows the same response to a given excitation as the actual sensor. A flowchart of the algorithm is shown in Fig. A-1. From Fig. 3-7, the DAQ board output is a voltage. It is then converted into its equivalent temperature value by using eq. $(3\text{-}3)$. The resulting curve will be fitted to eq. $(A\text{-}1)$

$$\Delta T = P \sum_{i=1}^{n} R_{th,i} \left(1 - e^{-\frac{t}{\tau_i}}\right) \qquad (A\text{-}1)$$

where P is the power applied (~110mW), n is the number of segments used and $\tau = R_{th} * C_{th}$.

MATLAB's Curve Fitting Toolbox™ [1] is leveraged with a custom equation (eq. $(A\text{-}1)$), and the transient response is used as the primary input. The toolbox uses a Non-Linear Least Squares Fitting [2] method to find the values of the variables, which would minimize the error across the entire data range. The convergence of the algorithm is strongly dependent on the various additional parameters available, such as the starting points of each variable, the data set across which to minimize the error, and the number of iterations. An attempt made to fit eq. $(A\text{-}1)$ to the measured data using the toolbox, with R_{th} and τ both as unknowns, resulted in a maximum of 4 segments with an error of more than 20%. As a result, specific frequency points were chosen for the fitting algorithm. This results in a fixed value of τ, and the fitting algorithm has to fit only one unknown, R_{th}.

An initial fitting was first used to estimate the starting point of each of the variables for aiding the convergence algorithm. In this initial fitting stage, a first estimate of the unknown variables was made using a simple linear fitting. These were then used as inputs to the toolbox, which fits the measured data to eq. $(A\text{-}1)$ with R_{th} as the only unknown. This fitting is done iteratively, where the highest targeted frequency is fitted first, followed by iteratively adding the lower frequencies. For instance, while fitting frequencies 5kHz, 2.5kHz, and 1kHz, the algorithm would first only fit $R_{th,5kHz}(1\text{-}\exp(-t/\tau_{5kHz}))$ and try to minimize the error across the entire data set. In the next cycle, the algorithm will be updated to fit $R_{th,5kHz}(1\text{-}\exp(-t/\tau_{5kHz}))+ R_{th,2.5kHz}(1\text{-}\exp(-t/\tau_{2.5kHz}))$ with the value of $R_{th,5kHz}$ now known from the first run. The algorithm then continues to add the lower frequencies iteratively. This is done primarily to aid the convergence algorithm, which fits only a single unknown per cycle.

The final convergence algorithm is then run. It has an outer loop that checks and terminates the entire fitting algorithm if the maximum error is below ± 3%. An inner loop is used, which follows a similar approach of fitting the highest frequency first, followed by the lower frequencies. To improve the convergence, the data across which the error is minimized is clipped to smaller values as we move towards fitting lower frequencies. Taking the same example as above, when fitting frequencies 5kHz, 2.5kHz, and 1kHz, the algorithm would first only fit $R_{th,5kHz}(1\text{-}\exp(-t/\tau_{5kHz}))$ and try to minimize the error across the entire data set. In the next cycle, the algorithm will be updated to fit $R_{th,5kHz}(1\text{-}\exp(-t/\tau_{5kHz}))+ R_{th,2.5kHz}(1\text{-}\exp(-t/\tau_{2.5kHz}))$, with the value of $R_{th,5kHz}$ now known, to a data set after excluding first

fs/(2*pi*5000) points. This is done based on the assumption that the high-frequency time constants will dominate the initial data points. The initial values of R_{th} for each run are updated based on the previous run, allowing the algorithm to get a better initial estimate, resulting in a better final estimate. The loop slowly converges to the required value to minimize the error across the entire data range.

The fitting results vs measurement results, along with the error % across the entire data range, is shown in Fig. A-2. With the values of R_{th} and τ known, the values of C_{th} can be found easily and are given in Table A-1.

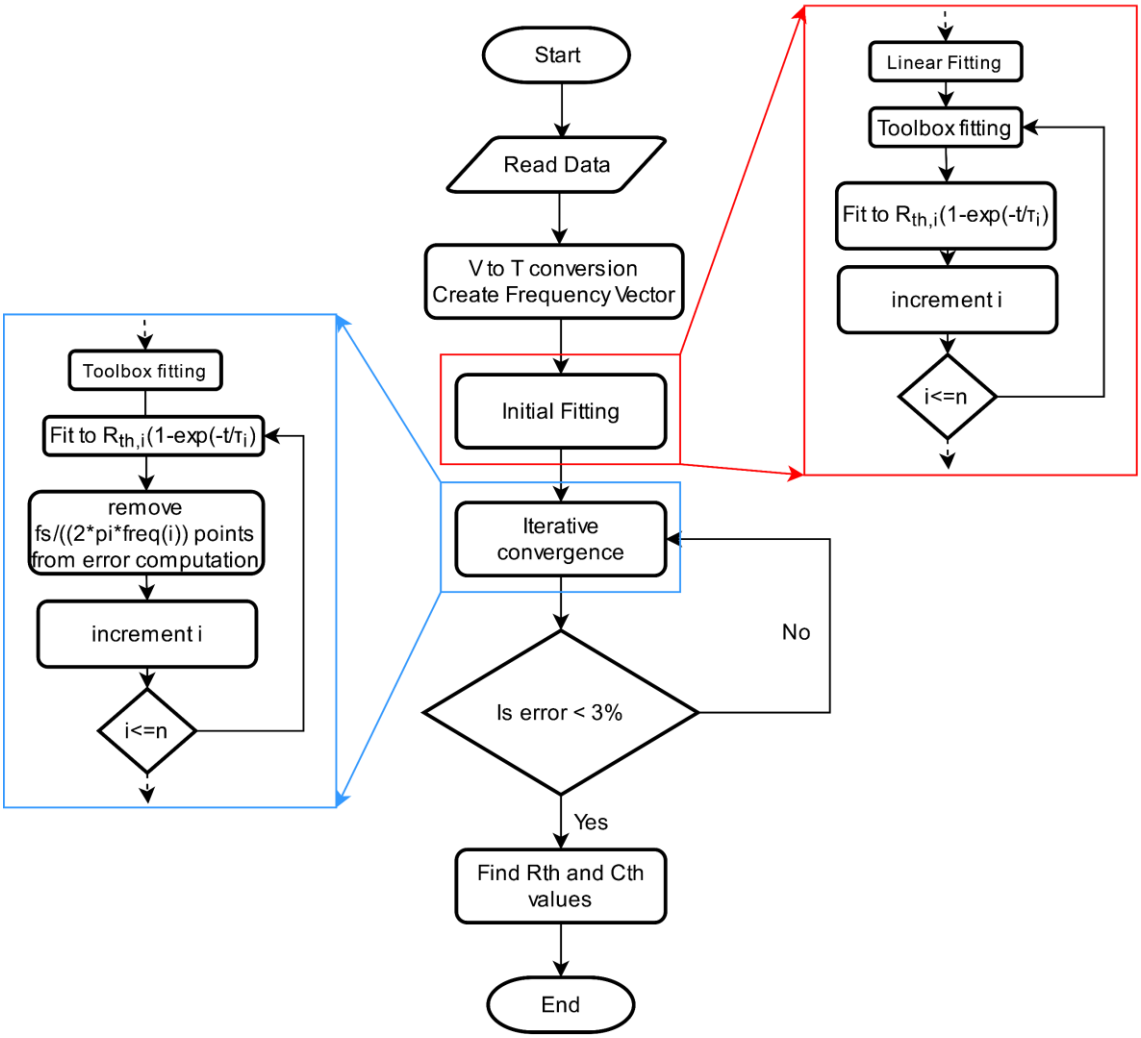

Fig. A-1: Flow-Chart for the Thermal Modelling Algorithm

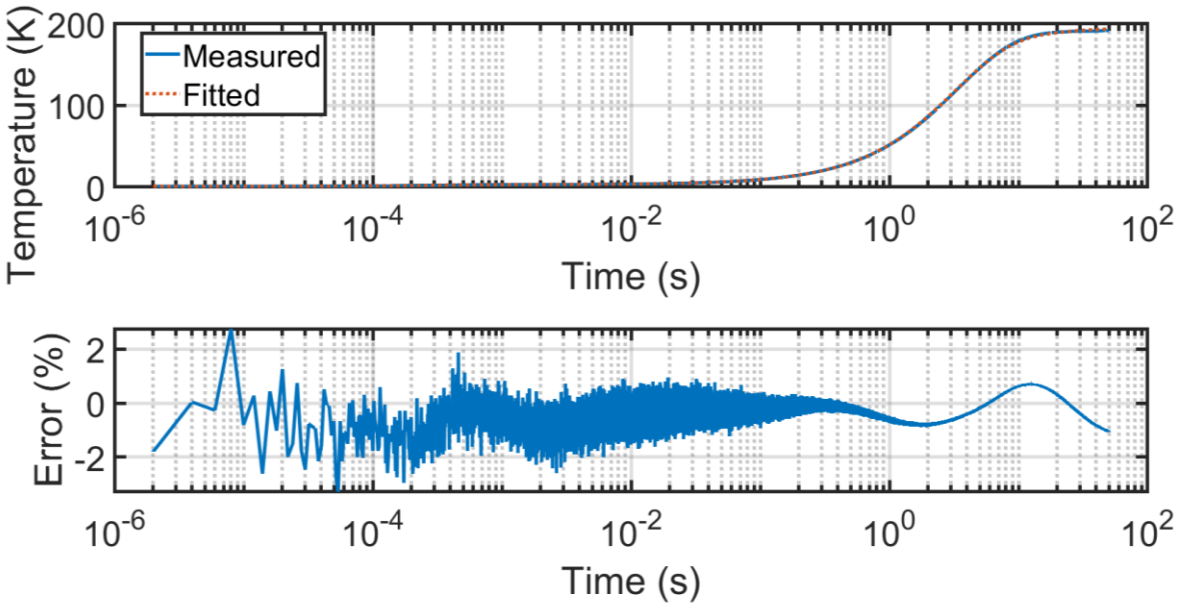

Fig. A-2: Fitted vs measured results with error %

Table A-1: Thermal resistance and capacitance values found from the algorithm

Resistance	R_{th1}	R_{th2}	R_{th3}	R_{th4}	R_{th5}	R_{th6}	R_{th7}	R_{th9}	R_{th9}	R_{th10}
Value	7.6E-01	9.2E-01	1.2E+00	1.3E+00	1.4E+00	6.9E-01	7.2E-01	7.5E-01	8.0E-01	8.1E-01
Capacitance	C_{th1}	C_{th2}	C_{th3}	C_{th4}	C_{th5}	C_{th6}	C_{th7}	C_{th8}	C_{th9}	C_{th10}
Value	2.2E-04	1.9E-04	1.6E-04	1.5E-04	1.5E-04	3.2E-04	3.2E-04	3.1E-04	3.1E-04	3.2E-04
Resistance	R_{th11}	R_{th12}	R_{th13}	R_{th14}	R_{th15}	R_{th16}	R_{th17}	R_{th18}	R_{th19}	R_{th20}
Value	8.6E-01	6.6E-01	8.6E-01	6.6E-01	9.4E-01	8.0E-01	7.0E-01	5.6E-01	5.1E-01	5.9E-01
Capacitance	C_{th11}	C_{th12}	C_{th13}	C_{th14}	C_{th15}	C_{th16}	C_{th17}	C_{th18}	C_{th19}	C_{th20}
Value	3.1E-04	4.2E-04	3.4E-04	4.6E-04	3.4E-04	4.2E-04	5.0E-04	6.7E-04	7.7E-04	7.2E-04
Resistance	R_{th21}	R_{th22}	R_{th23}	R_{th24}	R_{th25}	R_{th26}	R_{th27}	R_{th28}	R_{th29}	R_{th30}
Value	5.5E-01	3.5E-01	4.2E-01	4.3E-01	2.0E-01	9.3E-02	2.9E-01	4.2E-01	4.2E-01	3.3E-01
Capacitance	C_{th21}	C_{th22}	C_{th23}	C_{th24}	C_{th25}	C_{th26}	C_{th27}	C_{th28}	C_{th29}	C_{th30}
Value	8.3E-04	1.4E-03	1.3E-03	1.5E-03	4.0E-03	2.1E-02	7.8E-03	6.3E-03	7.6E-03	1.2E-02
Resistance	R_{th31}	R_{th32}	R_{th33}	R_{th34}	R_{th35}	R_{th36}	R_{th37}	R_{th38}		
Value	2.8E-01	1.0E-01	3.8E-01	1.4E+00	2.5E+00	4.8E+00	1.6E+03	1.5E+02		
Capacitance	C_{th31}	C_{th32}	C_{th33}	C_{th34}	C_{th35}	C_{th36}	C_{th37}	C_{th38}		
Value	1.9E-02	7.7E-02	1.1E-01	3.7E-02	3.2E-02	3.3E-02	2.0E-03	1.0E-01		

References

[1] "Curve fitting toolbox," Curve Fitting Toolbox Documentation - MathWorks India, https://in.mathworks.com/help/curvefit/.

[2] "Nonlinear least squares (curve fitting)," Nonlinear Least Squares (Curve Fitting) - MATLAB & Simulink - MathWorks India, https://in.mathworks.com/help/optim/nonlinear-least-squares-curve-fitting.html.